COUPLED THERMO-HYDRO-MECHANICAL MODELING OF CO2 INJECTION IN A WATER FORMATION

A Thesis

by

JIA FU

Submitted to the Office of Graduate and Professional Studies of
Texas A&M University
in partial fulfillment of the requirements for the degree of

MASTER OF SCIENCE

Chair of Committee,	Nobuo Morita
Committee Members,	Zenon Medina-Cetina
	Jihoon Kim
Head of Department,	Jeff Spath

August 2021

Major Subject: Petroleum Engineering

ABSTRACT

This thesis proposed a new coupling model for the thermo-hydro-mechanical process during CO2 injection in the water formation by coupling the geomechanical and fluid flow models. This thesis aims to couple fluid flow with geomechanical effects, predict the magnitude of formation strain and pore pressure change, and evaluate the over-burden and under-burden formation stabilities for carbon storage projects in the water formation.

The new proposed model uses a finite-difference simulator, ECLIPSE, and an in-house finite-element simulator, Geo3D. The mechanical model is featured by the non-linear stress-strain relations, so it is more accurate to handle geomechanical effects. The reservoir simulator, ECLIPSE, calculates the pressure and temperature distribution, and the pressure and temperature variations and the strain field changes are transferred between two models via an interface program.

In order to validate the coupling model, the study is divided into two parts. First, we compare analytical and numerical solutions of reservoir compaction and ground surface subsidence induced by pressure and temperature changes to validate the ability of Geo3D in handling geomechanical effects. The errors in ground surface subsidence and reservoir compactions are around 0.023% and 0.17%, respectively. Second, the coupling model is validated by the Terzaghi's 1D compaction problem using the fixed total stress method. The validation evaluates pressure distribution and formation compaction.

The application of the coupling model is conducted in a conceptual model with a radial grid system. Stress polygons are applied to analyze the under- and over-burden stability at different time steps. Pressure distribution and strain field are also compared between

coupled model and the ECLIPSE-only model. Overall, the coupling of the fluid flow model and geomechanical model has helped us obtain more accuracy in reservoir simulation and provided us with a tool to evaluate the formation stability.

DEDICATION

I dedicate this work to my dream.

I dedicate this work to my ex-girlfriend. We still love each other, but life must continue even without being together. We will achieve our dream life even though I am not by your side.

ACKNOWLEDGEMENTS

I would like to thank my committee chair, Dr. Morita, and my committee members, Dr. Kim and Dr. Median-Cetina, for their guidance and support throughout this research.

Thanks also go to Dr. Chao Fang and Dr. Minjie Lu from the Department of Physics and Astronomy for their advice about life and academics, helping me get used to my new life. I cannot make it through the COVID-19 pandemic without their help and company. Thanks to my friend Dr. Ruxin Zhang for his help making my life easier.

Finally, thanks to my mother and father for their trust, emotional and financial support, and my ex-girlfriend for her encouragement and love.

CONTRIBUTORS AND FUNDING SOURCES

Contributors

This work was supervised by a thesis committee consisting of Professor Nobuo Morita [advisor] and Professor Jihoon Kim of the Department of Petroleum Engineering, and Professor Zenon Medina-Cetina of the Department of Civil Engineering.

The geomechanical simulator GEO3D is the work of Dr. Morita. The *Porosity Change for Coupling* in Chapter 2 comes from Dr. Morita's course lecture, *Finite Element Method for Geomechanics Problems in Oil Industries.* Appendix A and B are from Dr. Morita's course lecture, *Linear and Non-Linear Rock Mechanics.*

All other work conducted for the thesis (or) dissertation was completed by the student independently.

Funding Sources

Graduate study was supported by an assistantship from Texas A&M University.

NOMENCLATURE

ε	Strain
u, v, w	Displacement in x, y, z direction
σ	Stress
F	Force
E	Young's modules
v	Poisson's ratio
E_m	Matrix Young's modules
v_m	Matrix Poisson's ratio
α	Biot's constant
γ	The coefficient of linear thermal expansion
p	Pressure
T	Temperature
N	Shape function
t	time
$\boldsymbol{T}$	External force
W	External work
U	Strain energy
h	Formation thickness
R	Reservoir radius
D	Reservoir depth

ΔH	Reservoir compaction
k	Permeability
ϕ	Porosity
ρ	Density
$s_i, i = g, w$	Saturation of gas or water
v	Velocity
q	Injection rate
g	Gravity
$\mu_i, i = g, w$	Viscosity of gas or water
$k_{ri}, i = g, w$	Relative permeability of gas or water
e	Specific energy
Ψ	The conservation quantity for energy balance
q^i	Heat source
$\mathbf{j}_{th}$	The diffusive heat flux
V_{pore}	Pore volume
$\delta\bar{\theta}$	Pore volume change
c_f	Fluid compressibility coefficient

TABLE OF CONTENTS

Page

LIST OF FIGURES

Page

LIST OF TABLES

Page

CHAPTER I

INTRODUCTION

Carbon dioxide (CO2) capture and storage (CCS) is a process including collecting CO2, transport to a storage site, and long-term storage underground. CCS can reduce overall greenhouse effect mitigation costs and increase the possibility of achieving greenhouse gas emission reductions. According to the Global Status of CCS 2020, there are 65 commercial CCS facilities, among which 26 facilities are under operation (Global CCS Institute, 2020). International Energy Agency (IEA) thinks that after 2020 the industry's scale needs to grow rapidly to capture at least 2000 million tons in 2023 (Fig. 1). In order to meet the potentially rapid growth in CCS, more storage sites need to be selected. Site characterization, selection, and performance prediction are important for successful geological storage projects. Before choosing a site, the geological setting must be characterized to determine if the overlying cap rock will seal the storage site, if there is a sufficiently voluminous and permeable storage formation and whether any abandoned or active wells will compromise the integrity of the seal. The site selection requires a holistic study of pore pressure, stress variation, and strain change, affecting formation stability. Thus, the coupling of reservoir fluid flow with geomechanics simulations can be utilized in site selection for CCS.

Since traditional reservoir simulation packages usually are not able to analyze geomechanics effects induced by pressure and temperature change, the finite difference fluid flow simulators which can handle multiphase flow need to be coupled with finite

element applications which simulate geomechanical process but could only handle single-phase fluid flow. The combination of reservoir simulator and geomechanics simulator can provide us a complete simulation, including fluid flow and rock deformation when conducting CO2 injection and a tool that could assist CCS site selection.

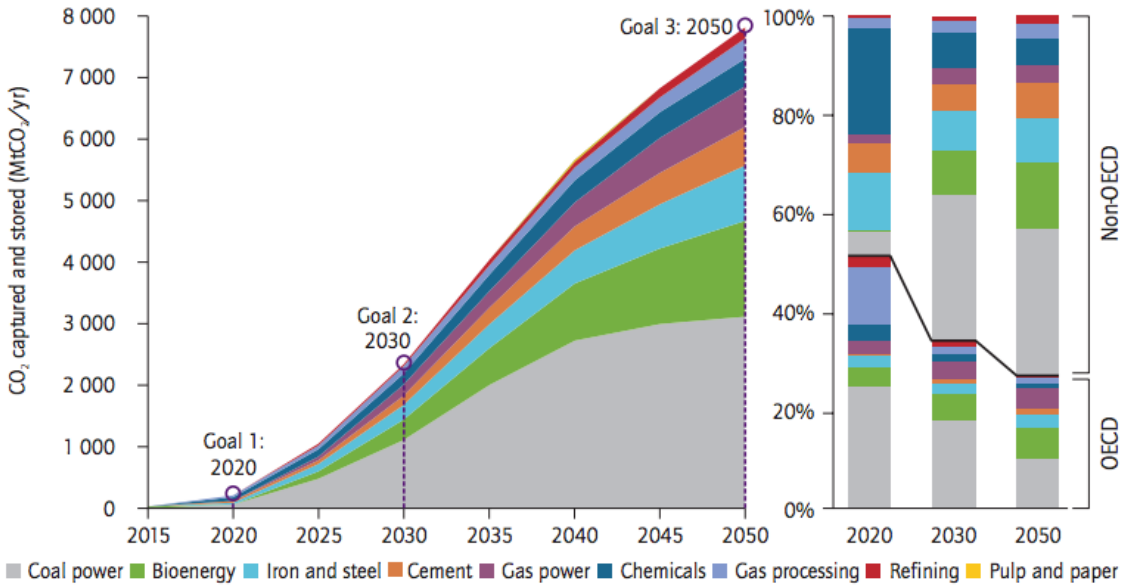

Figure 1-1 Global Carbon emission growth (IEA, 2013)

Background

The Sleipner storage project (Fig. 1-2), located in the mid-central North Sea, is operated by Statoil. This project is the first commercial-scale CO2 injection project in the world (Ghosh et al., 2015). Injection began in 1996 and at a North Sea Norwegian saline aquifer found between 800 and 1000 m below the seafloor. The storage formation is of the late Cenozoic age and is called the Utsira formation (Angeli et al., 2013). The Utsira formation

is a 200–250 m thick massive sandstone, with 15.5 Mt of injected CO2 since the project started until June 2015(MIT, 2015). The source of Sleipner's CO2 is the captured CO2 through collecting from the natural gas processing field located at Sleipner West (Gale et al., 2001). The stored CO2 is prevented from escaping to the surface by a 200–300 m thick layer of shale called the Nordland shales, which acts as caprock (Angeli et al., 2013). Although there is no evidence of leakage at the sea bottom, as 3D seismic monitoring has confirmed, the CO2 plume has risen through eight thin shale rock layers within the aquifer and reached the caprock in less than three years since the start of injection and storage. Nevertheless, while it is true that extensive experience on storage has been gained from CO2 storage projects like Sleipner, given the natural heterogeneity of geologic formations that vary from place to place, more far-reaching experience is needed to attain maturity in areas such as site selection, CO2 flood engineering, and reservoir management, workflow integration, monitoring and remediation, and regulatory development.

Carbon dioxide is a chemical compound of two elements, carbon and oxygen; its molecular formula is CO2. It exists in the atmosphere in small quantities (370 ppmv) and plays a crucial role in the Earth's environment as a necessary key in the life cycle of plants and animals. During photosynthesis, plants absorb CO2 and release oxygen. Anthropogenic activities which produce CO2 include the combustion of fossil fuels and other carbon-containing energy resources, the fermentation of organic compounds. Natural sources of CO2, including volcanic activity, also dominate the Earth's carbon cycle.

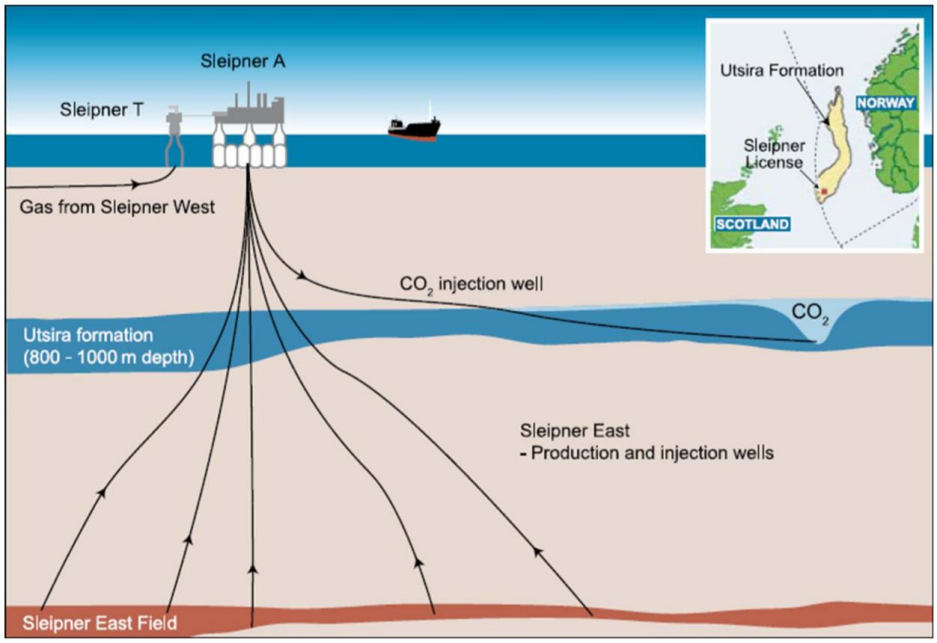

Figure 1-2 A simplified diagram of the Sleipner CO2 storage project, with an inset depicting the extent of the Utsira formation (IPCC, 2005)

Properties of Carbon Dioxide

At standard temperature and pressure, carbon dioxide is a gas. The physical state of CO2 varies with temperature and pressure, as shown in Fig. 1-3. At low temperatures, CO2 is solid; as temperature increases and when the pressure is less than 5.1 bar, the solid will sublime directly into the vapor state. At intermediate temperatures, between -56.5 ºC, the temperature of the triple point, and 31.1 ºC, the critical point, CO2 may be turned from a vapor into a liquid by compressing it to the corresponding liquefaction pressure. At a temperature higher than 31.1 ºC and a pressure larger than 73.9 bar, CO2 is in a supercritical state where it behaves like a gas. Under high pressure, the density of the gas can be very large, approximating or greater than the density of liquid water shown in Fig. 1-4. This is an essential feature of CO2, which is relevant to its storage. Heat is released

or absorbed in each phase changes across the solid-gas, solid-liquid, and liquid-gas boundaries (Fig. 1-3). However, the phase changes from the supercritical condition to liquid or the phase switches from supercritical to gas do not absorb or release heat. This property is important for designing CO2 compression facilities since it avoids handling the heat associated with the liquid-gas phase change.

Some physical properties of CO2 are given in Table 1-1. The phase diagram for CO2 is demonstrated in Fig. 1-3. The variation of the density of CO2 as a function of temperature and pressure is shown in Fig. 1-4, the variation of the vapor pressure of CO2 with temperature in Fig. 1-5, and the variation of viscosity with temperature and pressure in Fig. 1-6. The pressure-enthalpy chart for CO2 is shown in Fig. 1-7. The solubility of CO2 in water can be found in Fig.1-8.

Table 1-1 Physical Property of CO2 (NIST, 2003)

Property	**Value**
Molecular weight	44.01
Critical temperature	31.1 ℃
Critical pressure	73.9 bar
Critical density	467 kg/m^3
Triple point temperature	-56.5 ℃
Triple point pressure	5.18 bar
Boiling (sublimation) point (1.013 bar)	-78.5 ℃
Gas Phase	
Gas density (1.013 bar at boiling point)	2.814 kg/m^3
Gas density (@STP)	1.976 kg/m^3
Specific volume (@STP)	0.506 m^3/kg

Viscosity (@STP)	13.75 µPa·s
Thermal conductivity	14.65 mW·m/K
Solubility in water (@STP)	1.716 vol/vol
Enthalpy (@STP)	21.23 kJ/mol
Entropy (@STP)	117.2 J·mol/K
Entropy of formation	213.8 J·mol/K
Liquid Phase	
Vapor pressure (@ 20 °C)	58.5 bar
Liquid density (@ -20 °C and 19.7 bar)	1032 kg/m^3
Viscosity (@STP)	99 µPa·s

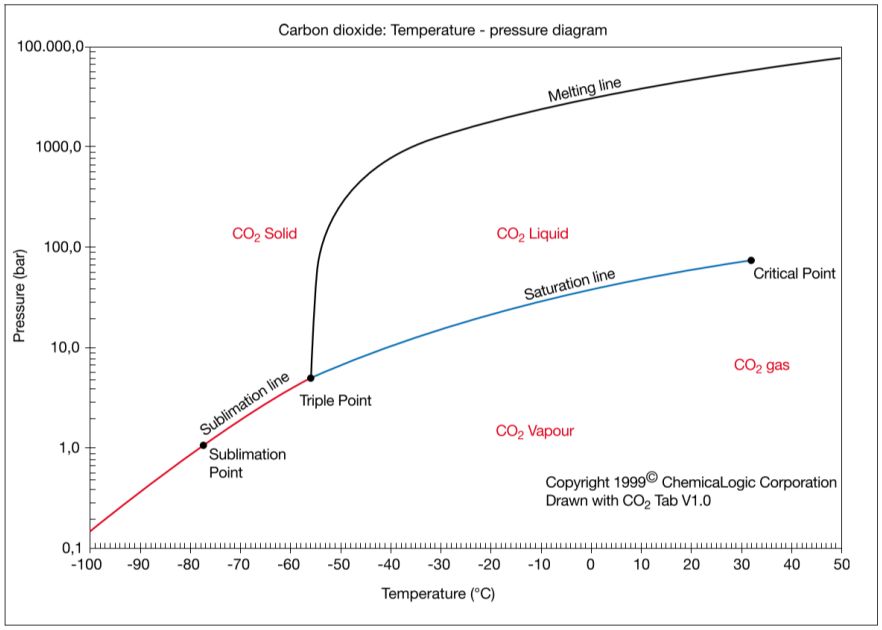

Figure 1-3 Phase diagram for CO2 (ChemicalLogic Corporation, 1999)

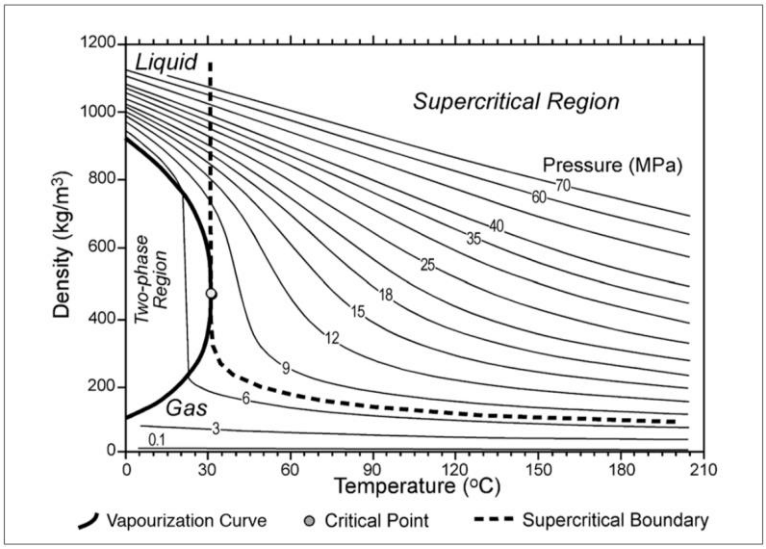

Figure 1-4 Variation of CO2 density as a function of temperature and pressure (Bachu, 2003)

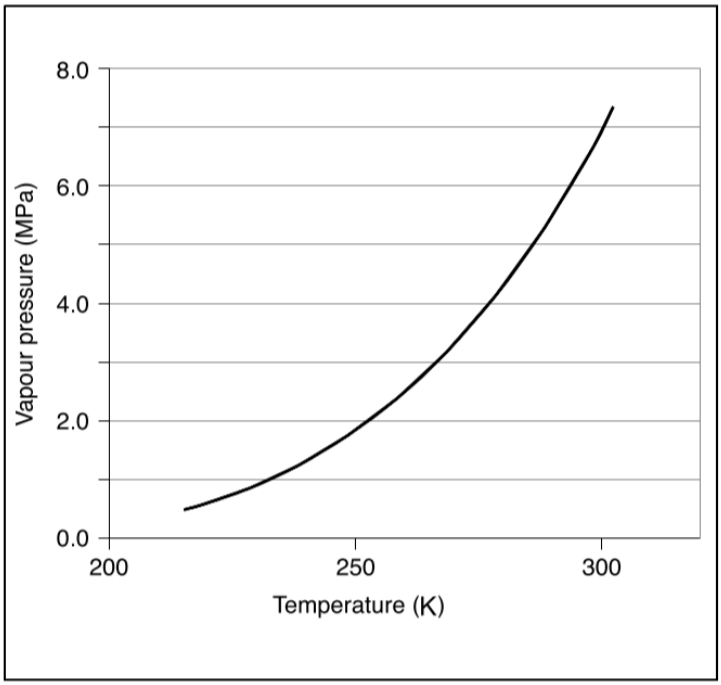

Figure 1-5 Vapor pressure of CO_2 as a function of temperature (Span and Wagner, 1996)

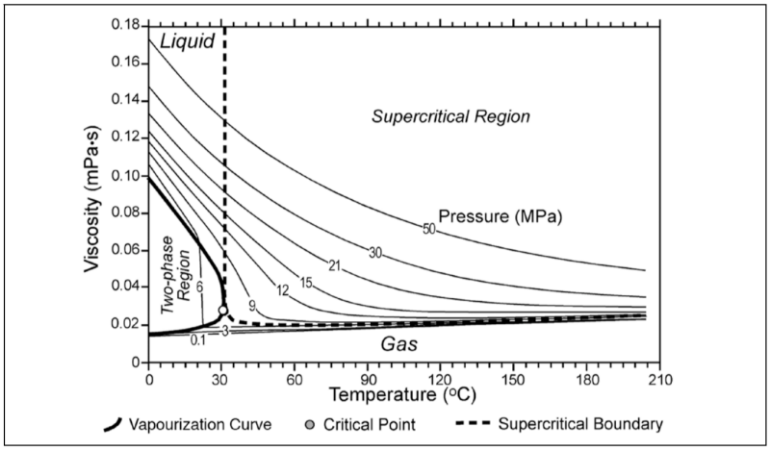

Figure 1-6 Variation of CO_2 viscosity as a function of temperature and pressure (Bachu, 2003)

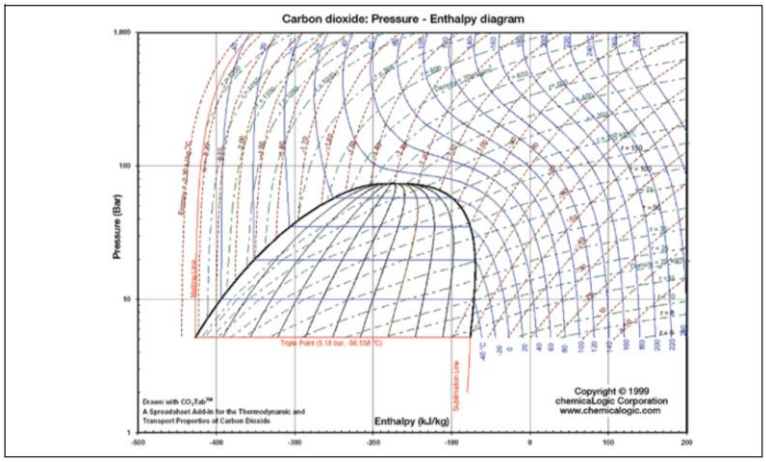

Figure 1-7 Pressure-Enthalpy chart for CO_2 (chemicaLogic Corporation, 2003)

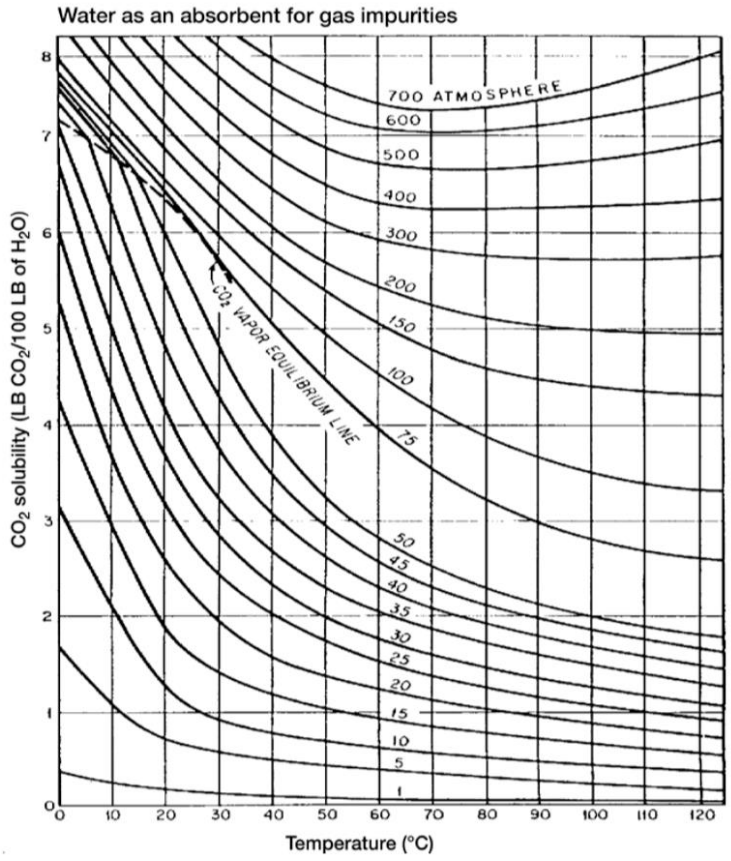

Figure 1-8 Solubility of CO_2 in water (Kohl and Nielsen, 1997)

Thermo-Hydro-Mechanical (THM) Coupled Physical Problem

THM coupled physical problems commonly exist in the engineering scenarios, such as carbon dioxide geological sequestration (CGS), oil and gas production, radioactive disposal, and enhanced geothermal systems. For CCS projects, supercritical CO2 is injected into depleted reservoirs or water formation, and injected fluid has a lower temperature than the formation. With the continuing injection, injected fluid reduces the formation temperature while pressure increases in the formation. Changes in temperature and pressure would lead to variations in stress and strain field and formation deformation

and further change permeability and porosity of the formation. Therefore, injection conditions could be affected, and fractures would be generated or reactivated. When failure occurs in caprock, CO2 leakage is likely to happen.

Research Objective

The objective of this research is to couple fluid flow with geomechanical effects and, therefore, to conduct a risk assessment of CO2 injection projects in water formation. In this research, we are going to calculate pressure, temperature, stress, and strain field change by applying a two-way coupling between a commercial finite-difference simulator, ECLIPSE, and an in-house finite-element simulator, GEO3D. Permeability and porosity would be updated each time step according to strain change calculated in the geomechanics simulator. And stress field change, induced by pressure change from Eclipse, would be loaded into GEO3D every time step. The coupling model investigates the aquifer as well as caprock and bedrock.

At last, we would obtain a time-dependent stress map and pressure change through the whole injection period and monitoring period. According to the stress map, we could evaluate the formation stability using the formation stability coefficient and stress polygon. Furthermore, we are going to do a parametric study to help site selection.

CHAPTER II

METHODOLOGY

In this chapter, we will develop the geomechanical model, the fluid model, and the coupling model, which will be applied in Chapter 3. The geomechanical model will be coded and validated in this chapter, while the fluid flow model will be solved by the commercial software ECLIPSE, which has been validated by the gas and oil industries. The geomechanical effect and fluid flow model will be coupled by the fixed total stress method. The porosity and permeability change represents the geomechanical effects in the fluid flow model. We will further discuss the expressions of pore volume change.

Geomechanical Model

A matrix expression is used for developing equations for the finite element method. The displacement strain relation is given by:

$$\boldsymbol{\varepsilon} = \begin{bmatrix} \frac{\partial}{\partial x} & 0 & 0 \\ 0 & \frac{\partial}{\partial y} & 0 \\ 0 & 0 & \frac{\partial}{\partial z} \\ \frac{\partial}{\partial y} & \frac{\partial}{\partial x} & 0 \\ 0 & \frac{\partial}{\partial z} & \frac{\partial}{\partial y} \\ \frac{\partial}{\partial z} & 0 & \frac{\partial}{\partial x} \end{bmatrix} \begin{bmatrix} u \\ v \\ w \end{bmatrix} \tag{2-1}$$

Equation of equilibrium is given by:

$$\nabla \boldsymbol{\sigma} + \boldsymbol{F} = 0 \tag{2-2}$$

Where $\nabla = \begin{bmatrix} \frac{\partial}{\partial x} & 0 & 0 & \frac{\partial}{\partial y} & 0 & \frac{\partial}{\partial z} \\ 0 & \frac{\partial}{\partial y} & 0 & \frac{\partial}{\partial x} & \frac{\partial}{\partial z} & 0 \\ 0 & 0 & \frac{\partial}{\partial z} & 0 & \frac{\partial}{\partial y} & \frac{\partial}{\partial x} \end{bmatrix}$

$$\sigma = [\sigma_x \quad \sigma_y \quad \sigma_z \quad \tau_{xy} \quad \tau_{yz} \quad \tau_{zx}]^T$$

$$F = [F_x \quad F_y \quad F_z]^T$$

The stress-strain relation is given by:

$$\sigma_{ij} = \frac{E}{1+v}\left(\varepsilon_{ij} + \frac{v}{1-2v}\varepsilon_{mm}\delta_{ij}\right) - \alpha p\delta_{ij} - \frac{E}{1-2v}\gamma\Delta T\delta_{ij} \tag{2-3}$$

where $\alpha = 1 - \frac{3(1-2v_m)}{E_m} \Big/ \frac{3(1-2v)}{E}, c_m = \frac{3(1-2v_m)}{E_m}, c_b = \frac{3(1-2v)}{E}$, α is the Biot's constant.

The matrix form of the above equation is given by:

$$\sigma = D\varepsilon - \alpha\bar{I}p - \gamma D\bar{I}\Delta T \tag{2-4}$$

where: γ is the coefficient of linear thermal expansion

$$\boldsymbol{\varepsilon} = \begin{bmatrix} \varepsilon_x & \varepsilon_y & \varepsilon_z & \gamma_{xy} & \gamma_{yz} & \gamma_{zx} \end{bmatrix}^T$$

$$\bar{I} = \begin{bmatrix} 1 & 1 & 1 & 0 & 0 & 0 \end{bmatrix}^T$$

$$D=\frac{E(1-\nu)}{(1+\nu)(1-2\nu)}\begin{bmatrix} 1 & \frac{\nu}{1-\nu} & \frac{\nu}{1-\nu} & & & \\ \frac{\nu}{1-\nu} & 1 & \frac{\nu}{1-\nu} & & & \\ \frac{\nu}{1-\nu} & \frac{\nu}{1-\nu} & 1 & & & \\ & & & \frac{1-2\nu}{2(1-\nu)} & & \\ & & & & \frac{1-2\nu}{2(1-\nu)} & \\ & & & & & \frac{1-2\nu}{2(1-\nu)} \end{bmatrix}$$

Using the virtual work principle, we discretize the system of elasticity equation. The virtual work principle states that for arbitrary virtual displacement if the internal and external work becomes stationary ($\delta U+\delta W=0$), the structure becomes in equilibrium condition. If the structure is in equilibrium, we have $\delta U+\delta W=0$.

The displacement with an element is interpolated with the nodal displacement with the following equation:

$$u=Nu^{e} \tag{2-5}$$

The displacement-strain relation is given by:

$$\varepsilon=Bu^{e} \tag{2-6}$$

where: N is the shape function, $N=\begin{bmatrix} N_1 & N_2 & ..... & N_{n-1} & N_n \end{bmatrix}$

$$B=\nabla^{T}N$$

$$u=\begin{bmatrix} u & v & w \end{bmatrix}^{T}$$

Now, consider virtual displacement δu^e. Then, the displacement and the strain within the element are given by:

$$\delta u = N \delta u^e \tag{2-7}$$

$$\delta \varepsilon = B \delta u^e \tag{2-8}$$

$$\sigma = D\varepsilon - \alpha \bar{I} p - \gamma D \bar{I} \Delta T \tag{2-9}$$

The external work induced by $\mathbf{T}$:

$$\delta W = \int_{\mathbf{S}} (\delta u)^T \mathbf{T} d\Gamma \tag{2-10}$$

The strain energy stored within the domain is given by:

$$\delta U = \int_V \left(\delta \varepsilon^T \sigma - \delta u^T F \right) d\Omega \tag{2-11}$$

If the structure is in equilibrium, we have $\delta U + \delta W = 0$:

$$\int_S (\delta u)^T \mathbf{T} d\Gamma + \int_V \left(\delta \varepsilon^T \sigma - \delta u^T F \right) d\Omega = 0 \tag{2-12}$$

$$\left(\delta u^e \right)^T \int_{S^e} N^T \mathbf{T} d\Gamma + \left(\delta u^e \right)^T \int_{V^e} \left(B^T \sigma - N^T F \right) d\Omega = 0 \tag{2-13}$$

If this equation holds for arbitrary displacement, the following equation holds:

$$\int_{S^e} N^T \mathbf{T} d\Gamma + \int_{V^e} \left(B^T \sigma - N^T F \right) d\Omega = 0 \tag{2-14}$$

For linear and non-linear plasticity problems, the neutral stress does not affect the calculation of the stress, strain, and displacement after the neutral stress is applied. Hence, we need only consider the net stress as the initial condition after subtracting the initial pore pressure. Then, after the calculation is completed, the neutral stress is added if the total stress needs to be determined.

Hence, we have:

$$\int_{S^e} N^T \mathbf{T} d\Gamma + \int_{V^e} \left(B^T \sigma^{net} - N^T F \right) d\Omega = 0 \tag{2-15}$$

Plugging in the following equation.

$$\sigma^{net} = D\varepsilon - \alpha \bar{I} p - \gamma D \bar{I} \Delta T \tag{2-16}$$

We have:

$$\int_{S^e} N^T \mathbf{T} d\Gamma + \left(\int B^T D B d\Omega \right) u^e - \left(\alpha \int B^T \bar{I} N d\Omega \right) p^e - \left(\gamma \int B^T D \bar{I} N d\Omega \right) \Delta T^e - \int_{V^e} N^T F d\Omega = 0 \tag{2-17}$$

Geomechanical Code

The Geomechanical model is coded by FORTRAN, and the program is named GEO3D. GEO3D simulates the earth's movement under various loading conditions. The following figure is the workflow for the geomechanics code (Fig. 2-1). First, initialize the program and determine the dimensions of variables. Second, input mesh information, rock properties, initial stress field, and loading steps. Third, load the original stress field to the formation. Forth, load external forces, which include changes of pressure and temperature fields obtained from Eclipse at the current time step. The next procedure is to calculate the stiffness matrix and solve the equation by the solver Pardiso. Then calculate residual force and check convergence. If convergent, continue to output results. If not convergent, start the next iteration after outputting the results of the current time step. The next step begins and goes back to the loading increment.

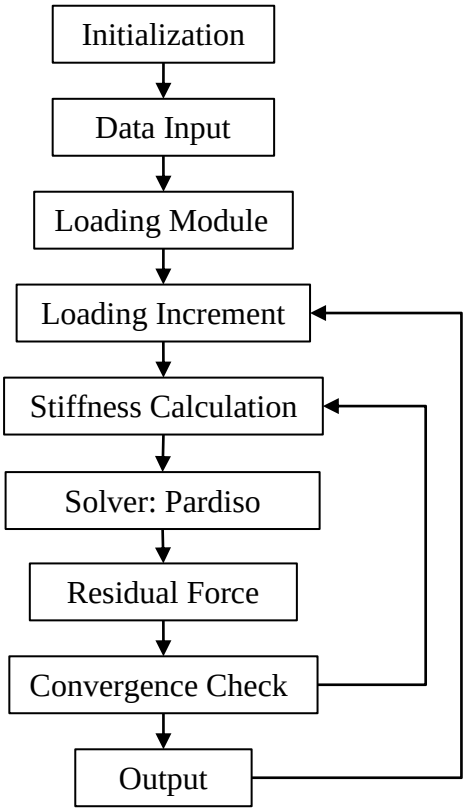

Figure 2-1 Geomechanics code workflow

Accuracy of Geomechanical Code

The geomechanics model is able to simulate geomechanical effects induced by temperature and pressure change. During CO2 injection, the formation pressure will increase and, therefore, leads to formation expansion and ground surface uplift. On the other hand, cold CO2 will reduce the formation temperature, which causes ground subsidence and formation contraction. The fluid flow model, Eclipse, has been used for so many years so that we do not need to verify the model's accuracy. Thus, we need to check the accuracy of our geomechanical code before coupling with Eclipse. In this

section, we check the accuracy of this model under temperature and pressure load separately. The solution of our model will be compared with an analytical solution with respect to the earth's surface subsidence and reservoir compaction. In order to satisfy the accuracy requirement in engineering applications, errors are controlled in the range of 0.5%. The accuracy is checked for the radially symmetric compaction problem, as shown in Fig. 2-2. An analytical solution is available for the problem if the elastic moduli of the overburden and reservoir formation are the same.

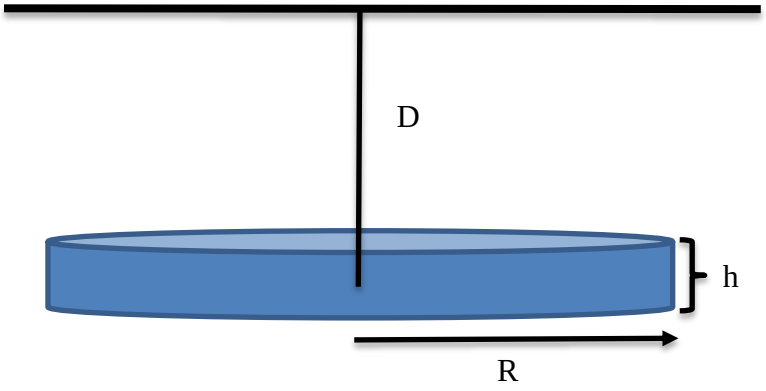

Fig.2-2 Circular reservoir for subsidence and compaction problems

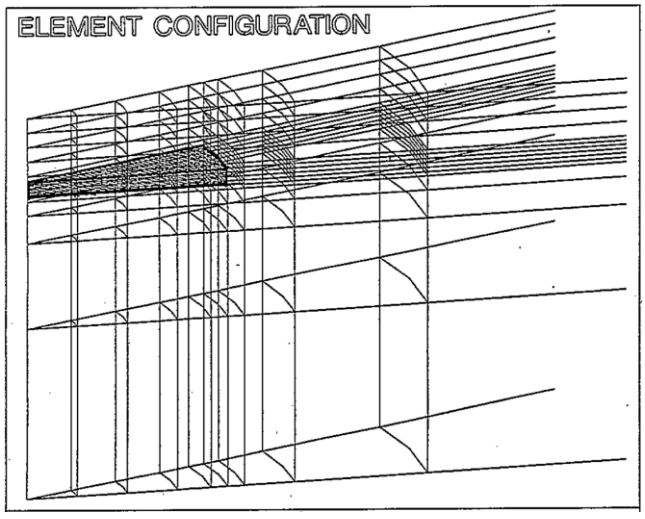

Fig.2-3 Element configuration for radially symmetric subsidence and compaction problems

All the simulations were performed using a radial model with 20 elements in the radial direction and 70 elements in the vertical direction (see Fig.2.3 and Table 2-1 for full details of the model).

Table 2-1 Geometrical and Geomechanical Property

Property	**Value**
Depth to the base rock	93442 ft.
Model radius, r	300000 ft.
Coefficient of linear thermal expansion, γ	2.3E-5 K^{-1}
Aquifer	
Depth of aquifer center, D	3050 ft.
Thickness, h	100 ft.
Reservoir radius, R	9842.87 ft.
Bulk young's modulus, E	2E6 psi
Bulk poisson's ratio, v	0.2
Young's modulus of matrix, E_m	9.825E6 psi
Poisson's ratio of matrix, v_m	0.2
Over-, under-burden and side rock	
Bulk young's modulus, E	2E6 psi
Bulk poisson's ratio, v	0.2
Young's modulus of matrix, E_m	9.825E6 psi
Poisson's ratio of matrix, v_m	0.2

Accuracy of Pressure-Induced Formation Deformation

A pressure increment of 1000 psi is uniformly loaded in the aquifer, while pressure remains constant in other sections. The formation will expand, and uplift will occur at the ground surface. Therefore, the solution of reservoir expansion and ground surface uplift

are two aspects which we checked accuracy the numerical solutions are compared with analytical solutions.

The analytical solution of subsidence at the center of the ground surface is calculated by the following equation (see Appendix A):

$$u_z(0,0) = 2C_M h\Delta p(1-v)\left[1-\frac{1}{\sqrt{1+R/D}}\right] \tag{2-18}$$

Where: $C_M = \frac{\alpha(1-2v)(1+v)}{E(1-v)}$ and $\alpha = 1-\frac{1-2v_m}{E_m}\Big/\frac{1-2v}{E}$ is the Biot's constant.

The results of subsidence are shown in the following table:

Table 2-2 Solutions for ground subsidence induced by pressure increasing

Analytical Solution	Geo3D	Error
0.04037 ft	0.04038 ft	0.023%

In addition to the solution at the center, surface uplift with respect to radius also has been investigated by the strain nuclei method (see Appendix A).

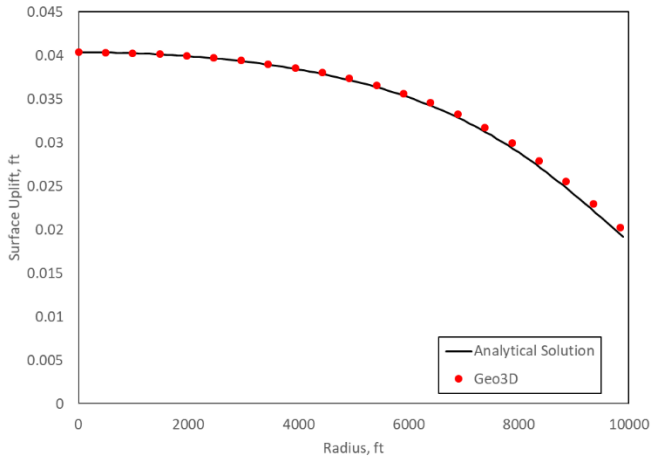

Figure 2-4 Pressure-induced ground surface uplift with respect to radius

The analytical solution of expansion at the center of the reservoir is calculated by the following equation:

$$\Delta H = C_M h \Delta p \tag{2-19}$$

The result of reservoir expansion is shown in the following table:

Table 2-3 Solutions for reservoir expansion induced by pressure increasing

Analytical Solution	Geo3D	Error
0.03584 ft	0.03578 ft	0.167%

Accuracy of Temperature-Induced Formation Deformation

A temperature reduction of $10°C$ is uniformly loaded in the aquifer, while the temperature remains constant in other sections. The formation will contract, and subsidence will occur at the ground surface due to thermal contraction induced by the injection of cold fluid. Therefore, the solution of reservoir contraction and ground surface subsidence are two aspects that we consider for an accuracy check. The numerical solutions are compared with analytical solutions.

The analytical solution of subsidence at the center of the ground surface is calculated by the following equation (see Appendix A):

$$u_z(0,0) = 2C_T h \Delta T (1-\nu)\left[1 - \frac{1}{\sqrt{1+R/D}}\right] \tag{2-20}$$

Where $C_T = \frac{\gamma(1+\nu)}{(1-\nu)}$ and γ is the coefficient of linear thermal expansion.

The results of subsidence are shown in the following table:

Table 2-4 Solutions for ground subsidence induced by temperature reduction

Analytical Solution	Geo3D	Error
-0.02196 ft	-0.02197 ft	0.023%

In addition to the solution at the center, surface uplift with respect to radius also has been investigated by the strain nuclei method (See appendix A, Fig. 2-5).

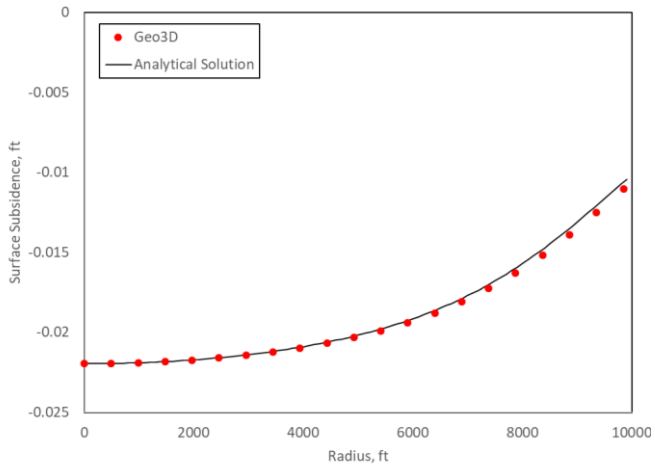

Figure 2-5 Temperature-induced ground surface subsidence with respect to radius

The analytical solution of compaction at the center of the reservoir is calculated by the following equation:

$$\Delta H = C_T h \Delta T \tag{2-21}$$

The results of subsidence are shown in the following table:

Table 2-5 Solutions for reservoir compaction induced by temperature reduction

Analytical Solution	Geo3D	Error
-0.01950	-0.019471	0.149%

Fluid Flow Model

Reservoir simulation is a direct numerical modeling method to simulate fluid flow in a reservoir. In this study, we are using Eclipse to conduct this process. Eclipse has been applied in the oil and industries for a long time and validated by practical applications. Some equations are used in fluid flow simulators, and the continuity equation is the main base of the simulation. The conservation law in the reservoir, including conservation of mass, energy, and momentum, is crucial for material balance and the continuity equation. Generally, the material balance and flow equation are solved for each grid.

The fluid flow is simulated by the compositional model in Eclipse. In this part, we will elaborate on equations that are solved in the model. The fluid mixture in the reservoir could be a gas phase or liquid phase or both, because of the composition of the fluid and the system's temperature and pressure. When pressure and temperature change, the ratio of every composition in different phases would change. For example, when the pressure goes up, the ratio of gaseous water decreases while liquid water increases. In our model, we have only two components and two phases flowing in the reservoir. The two phases are gas and water. H2O and CO2 are the two components. The mass transport could occur between two phases.

In the following equations, we use g and w to represent gas phase and water phase, and i represents different compositions. $i=1$ represents H_2O and $i=2$ represents CO_2. c_{ig} is the weight fraction of the component i in gas phase, and c_{iw} is the weight fraction the

component i in the water phase. Assuming a geometrical index α , and it is equal to 1 in the 3D model.

Mass flow rate of each phase:

$$\rho_g \mathbf{v}_g, \rho_w \mathbf{v}_w \tag{2-22}$$

Mass flow rate of the component i :

$$c_{ig}\rho_g \mathbf{v}_g + c_{iw}\rho_w \mathbf{v}_w \tag{2-23}$$

Weight of the component i in unit pore volume:

$$\phi\left(c_{ig}\rho_g s_g + c_{iw}\rho_w s_w\right) \tag{2-24}$$

According to the continuity equation for fluid flow, the mass conservation equation of component i is:

$$-\nabla\cdot\left[\alpha\left(c_{ig}\rho_g \mathbf{v}_g + c_{iw}\rho_w \mathbf{v}_w\right)\right] + \alpha q_i = \alpha\frac{\partial}{\partial t}\left[\phi\left(c_{ig}\rho_g s_g + c_{iw}\rho_w s_w\right)\right] \tag{2-25}$$

Where: q_i is injection rate of component i

Darcy's law considering gravity:

$$\begin{cases} \mathbf{v}_g = -\dfrac{\mathbf{k}k_{rg}}{\mu_g}\left(\nabla p_g - \rho_g g\nabla D\right) \\ \mathbf{v}_w = -\dfrac{\mathbf{k}k_{rw}}{\mu_w}\left(\nabla p_w - \rho_w g\nabla D\right) \end{cases} \tag{2-26\&27}$$

Where: D is depth

Plugging Darcy's law into the continuity equation, we have the mass conservation equation:

$$-\nabla\cdot\left[\frac{\alpha c_{ig}\rho_g \mathbf{k}k_{rg}}{\mu_g}\left(\nabla p_g-\rho_g g\nabla D\right)+\frac{\alpha c_{iw}\rho_w \mathbf{k}k_{rw}}{\mu_w}\left(\nabla p_w-\rho_w g\nabla D\right)\right]+\alpha q_i = \alpha\frac{\partial}{\partial t}\left[\phi\left(c_{ig}\rho_g s_g+c_{iw}\rho_w s_w\right)\right] \tag{2-28}$$

Auxiliary Equation

Assuming the formation is fully saturated by fluids, so we have:

$$s_g+s_w=1 \tag{2-29}$$

The total fraction of each component in one phase should be equal to 2. Therefore, we have the following equation for the water and gas phase:

$$\sum_{i=1}^{2} c_{iw}=1 \tag{2-30}$$

$$\sum_{i=1}^{2} c_{ig}=1 \tag{2-31}$$

The equilibrium constant:

$$\frac{c_{ig}}{c_{iw}}=k_{igw}\left(T,p_g,p_w,c_{ig},c_{iw}\right) \tag{2-32}$$

Capillary pressure between water and gas phase:

$$p_{cgw}=p_g-p_w \tag{2-33}$$

Heat Transport Model

To obtain the equation of energy conservation, we need to start from the first law of thermodynamics, which states that the variation of the total energy of a system is due to

the work of acting forces and heat transmitted to the system. The total energy per unit mass e (specific energy) can be determined as the sum of internal energy i and specific kinetic energy $v^2/2$. Internal energy is caused by molecular movement. Thus, the conservation quantity for energy balance is defined by:

$$\psi^e = \rho e = \rho\left(i + v^2/2\right) \tag{2-34}$$

According to mass conservation, we can get the balance equation for the internal energy:

$$\rho\frac{di}{dt} = \rho q^i - \nabla\cdot\mathbf{j}_{th} + \sigma\cdot\nabla\mathbf{v} \tag{2-35}$$

Where q^i is the heat source, and $\mathbf{j}_{th}$ is the diffusive heat flux.

According to the chain rule, the left-hand side of the above equation gives:

$$\rho\frac{di}{dt} = \rho\frac{dcT}{dt} = \rho T\frac{dc}{dt} + \rho c\frac{dT}{dt} \tag{2-36}$$

Applying the definition of the material derivative, we have:

$$\frac{dT}{dt} = \frac{\partial T}{\partial t} + \mathbf{v}\cdot\nabla T \tag{2-37}$$

Then the heat energy balance equation can be obtained:

$$\rho c\frac{dT}{dt} + \rho c\mathbf{v}\cdot\nabla T - \nabla\cdot\lambda\nabla T + \rho T\frac{dc}{dt} - \sigma\cdot\nabla\mathbf{v} = \rho q_{th} \tag{2-38}$$

Coupling Model

For most reservoir production problems, since the compressibility of oil and gas are significantly higher than the rock compressibility, the rock compressibility can be ignored, and the reservoir model may be independently run without coupling the geomechanical

code. After the pore pressure is calculated from the reservoir model, the geomechanical code calculates formation deformation using the pore pressure change calculated from the reservoir model.

However, if porosity exceeds 30%, the rock compressibility cannot be ignored. Or, for water injection wells, the water compressibility has similar order to the rock compressibility. Regardless of injection or production well, the extent of pore pressure change in the lateral direction is significantly larger than the vertical change except for the initial period. Then, the uniaxial compaction or uniaxial volume change assumption holds. The compressibility of the reservoir model is then the sum of the fluid compressibility and the rock compressibility with the uniaxial compaction assumption. The reservoir model gives good results except for the reservoir periphery, where the uniaxial compaction assumption does not hold. After the pore pressure is calculated from the reservoir model, the geomechanical code uses the pore pressure change calculated from the reservoir model.

During the reservoir compaction, the pressure in the overburden formation significantly changes in the vertical direction and lateral direction. However, the flow in the vertical direction is prevented since the permeability in the vertical direction is close to zero due to the lamination of shale streaks. In the horizontal direction, the deformation uniformly occurs in the vast lateral region so that the pressure gradient in the horizontal direction is close to zero. Because of these reasons, the overburden formation can use undrained Young's modulus and Poisson's ratio, assuming the fluid flow is not significant though the pore pressure changes significantly due to rock pore deformation.

In order to couple the fluid flow and geomechanical effects, three sequential coupling methods can be applied, including the fixed strain method, fixed total stress method, and undrained split. Among the above three, the second and the third methods are unconditionally stable with respect to time step and mesh size. The first method is unconditionally stable if the fluid compressibility is several times larger than the pore volume compressibility. For our project, the fixed stress method is applied. The flow problem is solved first while fixing the rate of the total mean stress. Then pore pressure distribution will be calculated in the flow model, and the geomechanical model will calculate deformation.

$$\begin{bmatrix} p^n \\ u^n \end{bmatrix} \rightarrow \begin{bmatrix} p^{n+1} \\ u^* \end{bmatrix}_{\delta\sigma_v=0} \rightarrow \begin{bmatrix} p^{n+1} \\ u^{n+1} \end{bmatrix} \tag{2-39}$$

Porosity Change for Coupling

This part will investigate the pore volume change induced by the geomechanical effect due to pressure and temperature change in the reservoir. The standard flow model uses porosity change as the pore volume change using:

$$\phi^* = V_{pore} / V_0 \tag{2-40}$$

where V_0 is a fixed bulk volume of each element.

Therefore, when the element volume changes, ϕ^* is no longer the true porosity. ϕ^* is given by

$$\phi^* = \phi_0 \left(1 + c_p dp - c_T dT + c_\sigma d\sigma_m + c_\varepsilon d\varepsilon_m\right) \tag{2-41}$$

where $d\sigma_m = \frac{1}{3} d\sigma_{kk}$ and the negative mean stress represents compression

The rock bulk, after deformation, becomes:

$$V = V_0(1+\varepsilon_{kk}) \tag{2-42}$$

Where $\varepsilon_{kk} = c_p dp - c_T dT + c_\sigma d\sigma_m + c_\varepsilon d\varepsilon_m$

The relation between ϕ^* and the real porosity ϕ is given by:

$$\phi^* = \phi(1+\varepsilon_{kk}) \tag{2-43}$$

Suppose the fixed total stress method is used for the fluid flow model, then, the pore volume change is given by:

$$\delta V_{pore} = \frac{1}{3}(c_b - c_m) d\sigma_{kk} + \left[c_b \alpha^2 + (\alpha - \phi) c_m\right] \delta p \tag{2-44}$$

For the isotropic linear elasticity or non-linear problems, the incremental pore volume change is given by

$$\delta\bar{\theta} = \left[\bar{I}^T \left(D_{ep}^{-1} - \frac{1}{3} c_m I)\right)^T \left(I - \frac{1}{3} c_m D_{ep} \hat{I}\right) \bar{I} + c_m \left(1 - \phi_0 - \frac{1}{9} c_m \bar{I}^T D_{ep} \bar{I}\right)\right] \delta p + \bar{I}^T \left(D_{ep}{}^{-1} - \frac{1}{3} c_m \hat{I}\right) d\sigma \tag{2-45}$$

Since $\delta\bar{\theta} = \phi^* - \phi_0$, we have

$$\phi^* - \phi_0 = \frac{1}{3}(c_b - c_m) d\sigma_{kk} + \left[c_b \alpha^2 + (\alpha - \phi) c_m\right] \delta p \tag{2-46}$$

Or for non-linear problems,

$$\phi^{*}-\phi_0=\left[\left((I-\frac{1}{3}c_m D_{ep})\,\bar{\mathrm{I}}\right)^T(\mathrm{D}_{ep}{}^{-1})^T\left(I-\frac{1}{3}c_m D_{ep}\hat{I}\right)\bar{I}+c_m\left(1-\phi_0-\frac{1}{9}c_m\bar{I}^T D_{ep}\bar{I}\right)\right]\delta p$$
$$+\bar{I}^T\left(D_{ep}{}^{-1}-\frac{1}{3}c_m\hat{I}\right)d\sigma \tag{2-47}$$

The porosity ϕ^* used in the flow model must be updated using the above equations.

If we use $\phi^*=\phi\left(1+c_p dp-c_T dT+c_\sigma dc_m+c_\varepsilon d\varepsilon_m\right)$, then we have:

$$c_\sigma=\frac{1}{3}\left(c_b-c_m\right)\Big/\phi_0 \tag{2-48}$$

$$c_p=\left[c_b\alpha^2+\left(\alpha-\phi\right)c_m\right]\Big/\phi_0 \tag{2-49}$$

for linear elasticity problems. While for non-linear problems, we have:

$$\delta V_{pore}=\left[\left\{(\mathrm{I}-\frac{1}{3}c_m D_{ep})\bar{I}\right\}^T\left(D_{ep}^{-1}-\frac{1}{3}c_m\hat{I}\right)\bar{I}+c_m\left(1-\phi_o-\frac{1}{9}c_m\bar{I}^T D_{ep}\bar{I}\right)\right]\delta p+\bar{I}^T\left(D_{ep}{}^{-1}-\frac{1}{3}c_m\hat{I}\right)d\sigma \tag{2-50}$$

Then, the following modifications are made for each iteration.

$$c_\sigma d\sigma_m=\bar{I}^T\left(D_{ep}{}^{-1}-\frac{1}{3}c_m\hat{I}\right)d\sigma\Big/\phi \tag{2-51}$$

$$c_p=\left[\left\{(\mathrm{I}-\frac{1}{3}c_m D_{ep})\bar{I}\right\}^T\left(D_{ep}^{-1}-\frac{1}{3}c_m\,\hat{\mathrm{I}}\right)\bar{I}+c_m\left(1-\phi_o-\frac{1}{9}c_m\bar{I}^T D_{ep}\bar{I}\right)\right]\Big/\phi_0 \tag{2-52}$$

The calculations are performed using the following explicit form.

$$D_{ep}{}^{-1}=\begin{pmatrix} b_{11} & b_{12} & b_{13} & b_{14} & b_{15} & b_{16}\\ b_{21} & b_{22} & b_{23} & & & \\ b_{31} & b_{32} & b_{33} & & & \\ b_{41} & & & & & \\ b_{51} & & & & & \\ b_{61} & & & & & b_{66}\end{pmatrix} \tag{2-53}$$

$$\left(D_{ep}{}^{-1}-\frac{1}{3}c_m\hat{I}\right)=\begin{pmatrix} b_{11}-\frac{1}{3}c_m & b_{12} & b_{13} & b_{14} & b_{15} & b_{16} \\ b_{21} & b_{22}-\frac{1}{3}c_m & b_{23} & & & \\ b_{31} & b_{32} & b_{33}-\frac{1}{3}c_m & & & \\ b_{41} & & & & & \\ b_{51} & & & & & \\ b_{61} & & & & & b_{66} \end{pmatrix} \tag{2-54}$$

$$\bar{I}^T\left(D_{ep}{}^{-1}-\frac{1}{3}c_m\hat{I}\right)=\begin{pmatrix} b_{11}+b_{21}+b_{31}-\frac{1}{3}c_m \\ b_{12}+b_{22}+b_{32}-\frac{1}{3}c_m \\ b_{13}+b_{23}+b_{33}-\frac{1}{3}c_m \\ b_{14}+b_{24}+b_{34} \\ b_{15}+b_{25}+b_{35} \\ b_{16}+b_{26}+b_{36} \end{pmatrix}^T \tag{2-55}$$

$$c_\sigma d\sigma_m=\frac{1}{\phi}\bar{I}^T\left(D_{ep}{}^{-1}-\frac{1}{3}c_m\hat{I}\right)d\sigma=\frac{1}{\phi}\begin{pmatrix} d\sigma_{11} & d\sigma_{22} & d\sigma_{33} & d\sigma_{23} & d\sigma_{31} & d\sigma_{12} \end{pmatrix}\begin{pmatrix} b_{11}+b_{21}+b_{31}-\frac{1}{3}c_m \\ b_{12}+b_{22}+b_{32}-\frac{1}{3}c_m \\ b_{13}+b_{23}+b_{33}-\frac{1}{3}c_m \\ b_{14}+b_{24}+b_{34} \\ b_{15}+b_{25}+b_{35} \\ b_{16}+b_{26}+b_{36} \end{pmatrix} \tag{2-56}$$

$$c_p=\left[\left\{(\mathrm{I}-\frac{1}{3}c_m D_{ep})\bar{I}\right\}^T(D_{ep}^{-1}-\frac{1}{3}c_m\hat{\mathrm{I}})\bar{I}+c_m(1-\phi_o-\frac{1}{9}c_m\bar{I}^T D_{ep}\bar{I})\right]/\phi_0 \tag{2-57}$$

$$\left\{(\mathrm{I}-\frac{1}{3}c_m D_{ep})\bar{I}\right\}^T(D_{ep}^{-1}-\frac{1}{3}c_m\hat{\mathrm{I}})\bar{I}=\begin{pmatrix} b_{11}+b_{21}+b_{31}-\frac{1}{3}c_m \\ b_{12}+b_{22}+b_{32}-\frac{1}{3}c_m \\ b_{13}+b_{23}+b_{33}-\frac{1}{3}c_m \\ b_{14}+b_{24}+b_{34} \\ b_{15}+b_{25}+b_{35} \\ b_{16}+b_{26}+b_{36} \end{pmatrix}^T\begin{pmatrix} b_{11}+b_{21}+b_{31}-\frac{1}{3}c_m \\ b_{12}+b_{22}+b_{32}-\frac{1}{3}c_m \\ b_{13}+b_{23}+b_{33}-\frac{1}{3}c_m \\ b_{14}+b_{24}+b_{34} \\ b_{15}+b_{25}+b_{35} \\ b_{16}+b_{26}+b_{36} \end{pmatrix} \tag{2-58}$$

$$\bar{I}^T D_{ep}\bar{I}=d_{11}+d_{21}+d_{31}+d_{12}+d_{22}+d_{32}+d_{13}+d_{23}+d_{33} \tag{2-59}$$

$$c_p = \left[\begin{pmatrix} b_{11}+b_{21}+b_{31}-\frac{1}{3}c_m \\ b_{12}+b_{22}+b_{32}-\frac{1}{3}c_m \\ b_{13}+b_{23}+b_{33}-\frac{1}{3}c_m \\ b_{14}+b_{24}+b_{34} \\ b_{15}+b_{25}+b_{35} \\ b_{16}+b_{26}+b_{36} \end{pmatrix}^T \begin{pmatrix} b_{11}+b_{21}+b_{31}-\frac{1}{3}c_m \\ b_{12}+b_{22}+b_{32}-\frac{1}{3}c_m \\ b_{13}+b_{23}+b_{33}-\frac{1}{3}c_m \\ b_{14}+b_{24}+b_{34} \\ b_{15}+b_{25}+b_{35} \\ b_{16}+b_{26}+b_{36} \end{pmatrix}\right] \quad \text{(2-60)}$$

$$+c_m(1-\phi_o-\frac{1}{9}c_m(d_{11}+d_{21}+d_{31}+d_{12}+d_{22}+d_{32}+d_{13}+d_{23}+d_{33}))$$

For one phase finite element flow model, we have

$$\bar{K}^e(p^e)^{n+1}+S_p(p^e)^{n+1}=F_q^e+F_Q^e-[H^t(\sigma)^{n+1}-H^t(\sigma)^n]+S_p(p^e)^n \quad \text{(2-61)}$$

where: $\bar{K}^e=\frac{\Delta t}{(\rho)_{center}}(\frac{\rho k\delta}{\mu})_{up}\int(\nabla N)^T K(\nabla N)d\Omega$

$$H^t(\sigma)^n=\int N^T \begin{pmatrix} d\sigma_{11} & d\sigma_{22} & d\sigma_{33} & d\sigma_{23} & d\sigma_{31} & d\sigma_{12} \end{pmatrix} \begin{pmatrix} b_{11}+b_{21}+b_{31}-\frac{1}{3}c_m \\ b_{12}+b_{22}+b_{32}-\frac{1}{3}c_m \\ b_{13}+b_{23}+b_{33}-\frac{1}{3}c_m \\ b_{14}+b_{24}+b_{34} \\ b_{15}+b_{25}+b_{35} \\ b_{16}+b_{26}+b_{36} \end{pmatrix} d\Omega$$

$$S_p=[(V_{pore}c_f)_{center}]\int N^T N d\Omega+\int N^T c_p N d\Omega$$

$$F_q^e=-\frac{\Delta t}{\rho_{center}}\int N^T q dl$$

$$F_Q^e=-\frac{\Delta t}{\rho_{center}}\int_{\Gamma_1} N^T \bar{q}\, d\Gamma$$

Coupling between ECLIPSE and Geo3D

We apply the two-way coupling method to simulate the coupled processes during CO2 injection (Fig. 2-6). The whole coupling loop is controlled by an interface program which is coded by Python. First, we run the first step in ECLIPSE and pause the simulation at the end of this step. Then, the interface program extracts the original and updated pressure and temperature from ECLIPSE, and transfer temperature and pressure increments from the grid center to node points of the finite elements. To simplify this process, we make the grid systems of the reservoir model and the geomechanics model overlap each other as much as possible (see Fig.2-7). Fig. 2-8 demonstrates the data communication workflow in coupling loops. From ECLIPSE to Geo3D, pressure and temperature increment at Geo3D node points will be obtained by averaging the pressure value of neighboring ECLIPSE grids. When updating porosity and permeability, pore-volume change at Geo3D gauss points would be transferred to ECLIPSE grids. Therefore, porosity changes can be obtained by Eq. 2-50. The pore volume change calculated in Eq. 2-50 involves two aspects of deformation. The first is related to pore space; the second is about rock compressibility. Considering rock volume in ECLIPSE is constant, Eq. 2-50 can be rewritten as Eq. 2-62. And permeability can be updated by Eq. 2-63.

$$\delta\phi = \left[\left\{ (\mathrm{I} - \frac{1}{3} c_m D_{ep}) \bar{I} \right\}^T (D_{ep}^{-1} - \frac{1}{3} c_m \hat{\mathrm{I}}) \bar{I} + c_m (1 - \phi_o - \frac{1}{9} c_m \bar{I}^T D_{ep} \bar{I}) \right] \delta p + \bar{I}^T \left(D_{ep}^{-1} - \frac{1}{3} c_m \hat{I} \right) d\sigma \quad (2\text{-}62)$$

$$\frac{k_{n+1}}{k_n} = \frac{\phi_{n+1}^3}{(1-\phi_{n+1})^2} \times \frac{(1-\phi_n)^2}{\phi_n^3} \quad (2\text{-}63)$$

After transferring data from ECLIPSE to Geo3D, the first step will start in Geo3d. Then the updated stress and strain fields can be obtained, and next, we can update porosity and permeability based on the new stress field. After updating rock properties in ECLIPSE, the next coupling loop will start. The loop will keep running until all time steps are covered.

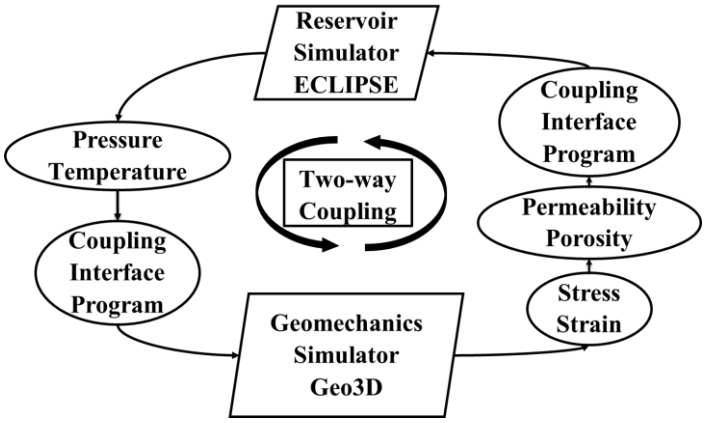

Figure 2-6 Two-way coupling loop

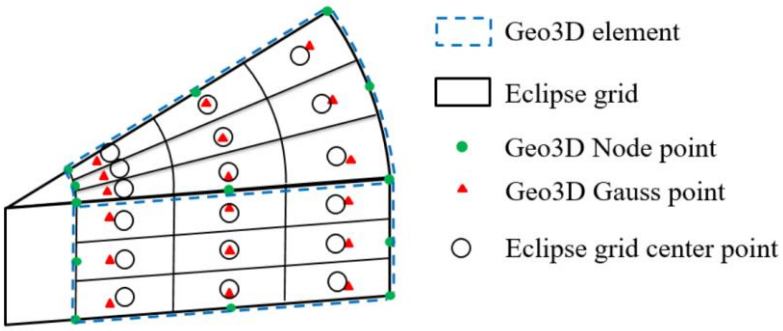

Figure 2-7 Mapping system for data communication

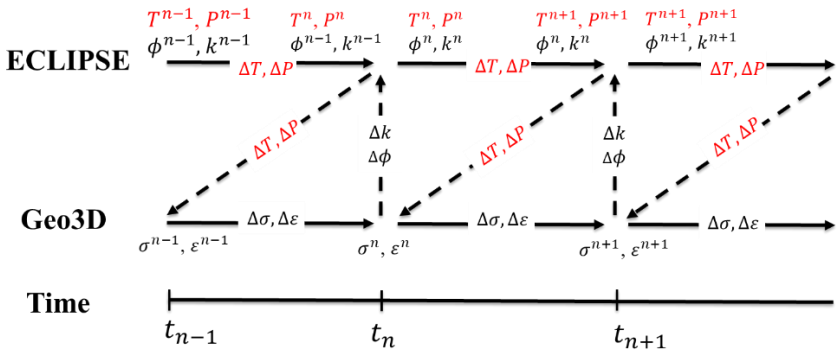

Figure 2-8 Data communication in time steps

Validation of the Coupling Model

In this part, we are going to validate the coupling model, the coupled Geo3D, and Eclipse.

The accuracy is checked by using Terzaghi's 1-D uniaxial compaction problem (Fig.2-9)

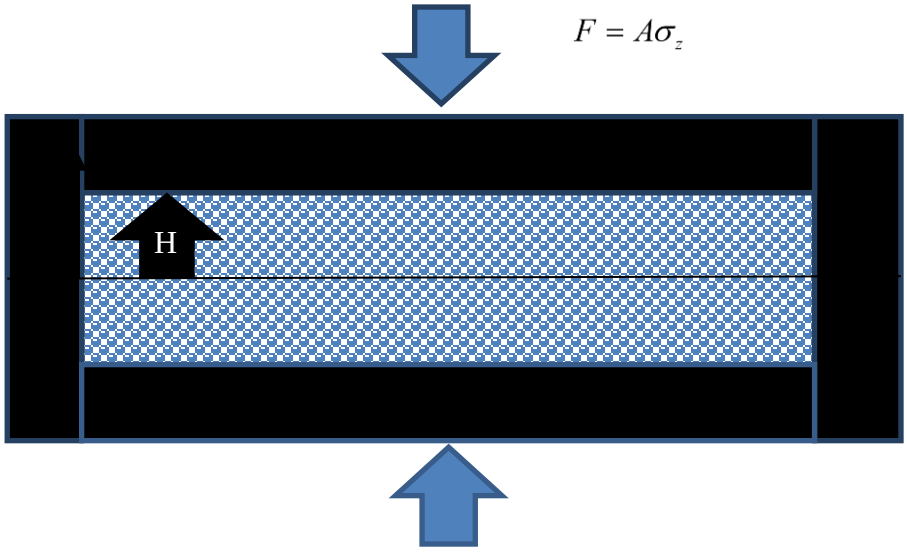

Figure 2-9 Terzhagi's uniaxial compaction problem

The following equations describe the flow and mechanical problem (see Appendix B):

$$\frac{k_z}{\mu}\frac{\partial^2 p}{\partial z^2} = \frac{1}{M}\frac{\partial p}{\partial t} + \alpha\frac{\partial}{\partial t}\frac{\partial u}{\partial z} \tag{2-64}$$

$$\overline{K}_{dr}\frac{\partial}{\partial z}\left(\frac{\partial u}{\partial z}\right)-\alpha\frac{\partial p}{\partial z}=0 \tag{2-65}$$

Let $M=1/\left[\phi c_f+(\alpha-\phi)c_m\right]$. The boundary condition includes constant stress at the upper surface and constant pressure of zero at the upper and bottom boundary. Since σ_z is constant during the uniaxial compaction, we have:

$$\frac{k_z}{\mu}\frac{\partial^2 p}{\partial z^2}=\frac{1}{M}\frac{\partial p}{\partial t}+\frac{\alpha^2}{\overline{K}_{dr}}\frac{\partial p}{\partial t} \tag{2-66}$$

And Eq. 2-64 can be written as:

$$c_v\frac{\partial^2 p}{\partial z^2}=\frac{\partial p}{\partial t} \tag{2-67}$$

Where: $c_v=\dfrac{k_z}{\mu}\dfrac{1}{\phi c_f+(\alpha-\phi)c_m+\dfrac{\alpha^2}{\overline{K}_{dr}}}$

Therefore, the pressure with respect to height and time is given by:

$$\frac{p}{p_0}=\frac{4}{\pi}\sum_{j=1}^{\infty}\left\{\frac{1}{2j-1}\sin\left[(2j-1)\frac{\pi}{2}\frac{z}{h}\right]e^{-(2j-1)^2\frac{\pi^2}{4}\frac{c_v t}{h^2}}\right\} \tag{2-68}$$

The total compaction for pressure change Δp is given by:

$$\Delta H=\frac{\alpha(1-2v)(1+v)}{E(1-v)}2h\Delta p \tag{2-69}$$

So, the transient compaction can be calculated by the following equation:

$$\Delta h=\Delta H\left\{1-\frac{8}{\pi^2}\sum_{j=1}^{\infty}\left[\frac{1}{(2j-1)^2}e^{-(2j-1)^2\frac{\pi^2}{4}\frac{c_v t}{h^2}}\right]\right\} \tag{2-70}$$

The parameters in Table 2-6 are used in obtaining analytical solutions and numerical solutions of pressure distribution and formation compaction. For the analytical solution, Eq. 2-68 and Eq. 2-70 are applied, and we define $\frac{c_v t}{h^2}$ as the dimensionless time to evaluate pressure distribution and compaction. The numerical solutions are obtained by coupling between ECLIPSE and Geo3D. Simulation in ECLIPSE is set up by using parameters in Table 2-6. Fig. 2-10 displays the analytical solution and numerical solution of pressure distribution at a different height. And Fig. 2-11 shows the analytical solution and numerical solution of compaction at the formation center with respect to thr dimensionless time. According to the comparison, the coupling model is able to obtain enough accuracy when handling the compaction problem during the CO2 injection.

Table 2-6 Parameters for one dimension compaction problem

Parameters	**Value**
E, kPa	1.38E+07
v	0.2
$c_f, 1/kPa$	4.08E-07
$\rho_f, g/cm^3$	0.94
ϕ	0.2
k, m^2	9.87E-14
$\mu, kPa \cdot s$	1.22E-06
Half height h, m	15
α	7.96E-01
Boundary stress σ_z, psi	1000

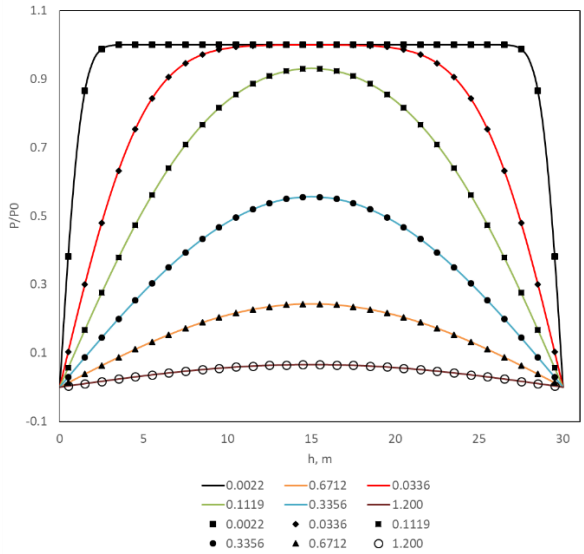

Figure 2-10 Pressure distribution

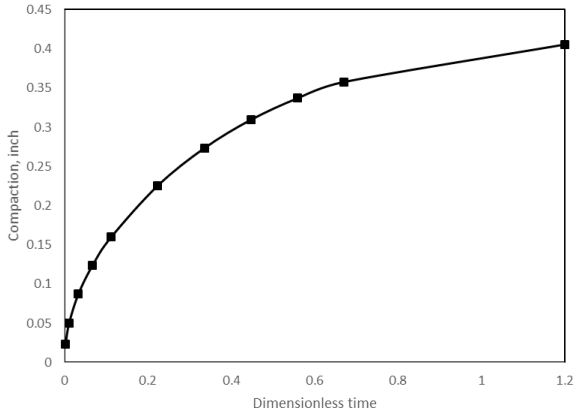

Figure 2-11 Compaction with respect to dimensionless time

CHAPTER III

COUPLING SIMULATION OF CARBON STORAGE IN WATER FORMATION

This chapter introduces a field application that applies the validated coupling model in Chapter 2, and the modeling procedure, reservoir, and fluid properties, and reservoir geometry will be introduced. Simulation results, such as pressure and stress distribution, CO2 plume distribution, and ground surface and reservoir deformation, will be evaluated.

Simulation Model

Geological Model

As a field application, the reservoir conditions similar to the Sleipner storage project, located in the mid-central North Sea (Figure 2-11), are assumed. The coupled geomechanics and reservoir model is applied to evaluate the reservoir performance during injection and storage. We used simplified cylindrical models instead of complex reservoir mesh to illustrate the parameter effects. The injection and storage of CO2 were simulated by using the ECLIPSE 300 compositional and thermal simulator, which applies the CO2STORE module. The geomechanical simulation is conducted by Geo3D, which is an in-house program considering non-linear stress and strain relation, and this simulator is able to handle both pressure and temperature changes.

The rock and fluid properties used for fluid flow and geomechanical simulations are shown in Table 3-1. For the fluid flow model, a grid of $36\times36\times60$ was employed, and the model has a radius of 3600 m, a height of 600 m, and the cylindrical model was divided

into 36 sections in the azimuthal direction. We use 700 m as the depth of the top face of the model. For the geomechanics model, there are 20 elements in the radial direction and 80 elements in the vertical direction. Among these elements, only 12 elements in the radial direction and 20 elements in the vertical direction will be coupled with fluid flow simulations. The model was divided into 12 sections in the azimuthal direction, and the geomechanical simulator only calculates one section of 12 due to the symmetry. The geomechanical model involves the entire formation from the ground surface to the depth of 28731 m. Some primary parameters of the fluid flow and geomechanical model can be found in Fig. 3-1. The boundary of the aquifer system was taken to be finite, meaning that the formation water cannot flow away as it is displaced by the carbon dioxide, and the pressure would increase rapidly. Since the fluid flow is assumed to be radially symmetric, the formation deformation and the stress changes are also radially symmetric if the linear isotropic elastic moduli are used. Therefore, for the three faulting regimes, the original directional stresses are superimposed to the stress changes induced by the radial fluid flow.

Table 3-1 Parameters for coupling simulation

Parameters	**Value**
E, Pa	1.38E+07, 6.89E+6 (soft aquifer)
v	0.2
ϕ (caprock, aquifer and bedrock)	1E-3, 0.1, 1E-3
k, mD (caprock, aquifer and bedrock)	1E-5, 50, 1E-5
k_v / k_h	0.1
Depth to top face of aquifer, m	1000
Temperature gradient, $°C / km$	29
Ground surface temperature, $°C$	20

Bottom hole pressure limit, bar	202.65
Rock density, g / cm^3	2.26
Fluid injection rate, tones/Day	417.95871
Injection period, year	10
Monitoring period, year	10

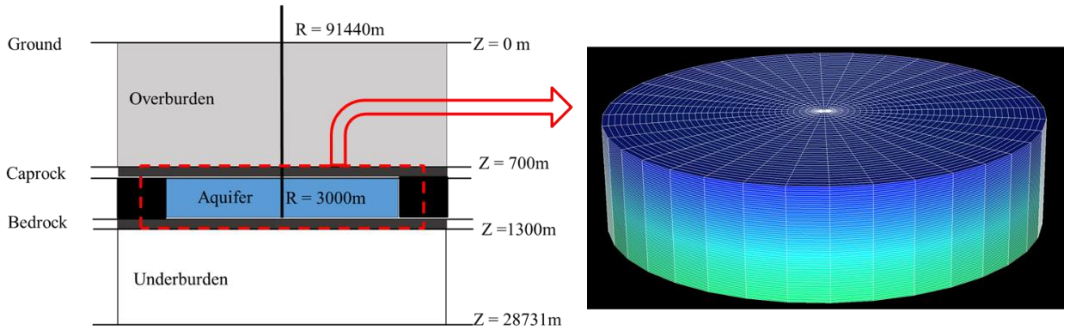

Figure 3-1 Geometrical models of coupling simulation

Reservoir and Fluid Properties

The target storage site comprises sandstones and tight shale. The sandstones are the target reservoir which has a thickness of 300 m with good porosity and permeability and occurs at depths of 850 m to 1150 m. The shale formation acts as a caprock or seal which prevents carbon dioxide escapes by buoyance.

Two different porosity and permeability regions were considered for simulations (Table 3-1). The vertical permeability was derived from a generic vertical to horizontal permeability ratio of 1:10. Based on the permeability values, we assume that the overlying and underlying boundaries of the aquifer are impermeable due to the presence of effective

caprock and bed rock. We applied the following relative permeability curves (Fig. 3-2) in simulations.

For carbon dioxide storage reservoir simulations, the capillary pressure is significant. The capillary pressure, which is the pressure difference between the non-wetting phase and wetting phase, is given by Eq. 3-1:

$$P_c = P_n - P_w \tag{3-1}$$

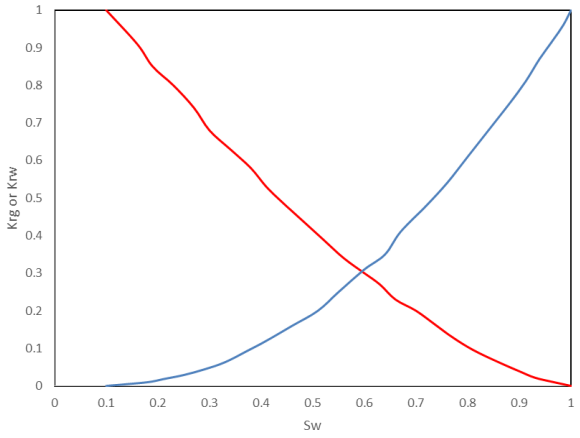

Figure 3-2 Relative permeability curves

The CO2 gas does not leak through the cap rock due to the capirally pressure below the irreducible gas saturation. The compositional model in E300 applies a modified Peng-Robinson equation of state, which is able to correctly compute the density, viscosity, and compressibility of CO2 as a function of temperature and pressure, as well as the mutual solubility of CO2 and brine. The fluid properties would be automatically calculated by the simulator.

The thermal option of E300 is able to calculate temperature distribution induced by the injection of cold carbon dioxide. Thermal parameters are taken from the standard thermal

CO2STORE option. Temperature changes would induce contract or expansion in the formation. Geo3D handles the thermal effects by applying the linear thermal expansion coefficient mentioned in Chapter 2. The density of the CO2-rich phase and the water vapor is computed for the standard CO2STORE option. The CO2 and H2O component is also defaulted by using CO2STORE option. The thermal parameters which are applied in simulations are shown in Table 3-2.

Table 3-2 Thermal parameters

Parameters	**Value**
Rock heat capacity, $kJ / m^3 / K$	1987.5
Rock conductivity,	302.4
1st coefficient of the component liquid specific heat	0.835 (CO2), 4.813 (H2O)
2nd coefficient of the component liquid specific heat	0.001 (CO2), 0.021 (H2O)
1st coefficient of the component gaseous specific heat	0.835 (CO2), 4.813 (H2O)
2nd coefficient of the component gaseous specific heat	0.001 (CO2), 0.021 (H2O)

Results and Discussion

This part will demonstrate and compare the results of coupled and Eclipse-only simulations. Two case studies will be involved, including homogeneous formation with the same Young's modules and a case with softer aquifer formation and harder over- and under-burden rocks, and both cases are initialized with normal-fault stress states.

Case 1: Homogeneous Formation

In this case, the whole formation has the same Young's modules. Due to the injection of cold supercritical carbon dioxide, the formation pressure increases significantly, and

temperature reduces. Increasing pressure inclines to expand the pore volume and porosity, and, therefore, permeability would increase, however, the cold supercritical CO2 incduce rock contraction which has opposite effects on porosity and permeability. Eq. (2-63) is applied to update permeability based on updated porosity values. Increasing permeability could reduce the resistance of fluid flow, and a lower injection pressure would be induced. The increasing permeability values can be found in Fig 3-3. Due to the increasing pore volume with a constant injection rate, the field pressure could be lower than the simulation without coupling with geomechanics effects.

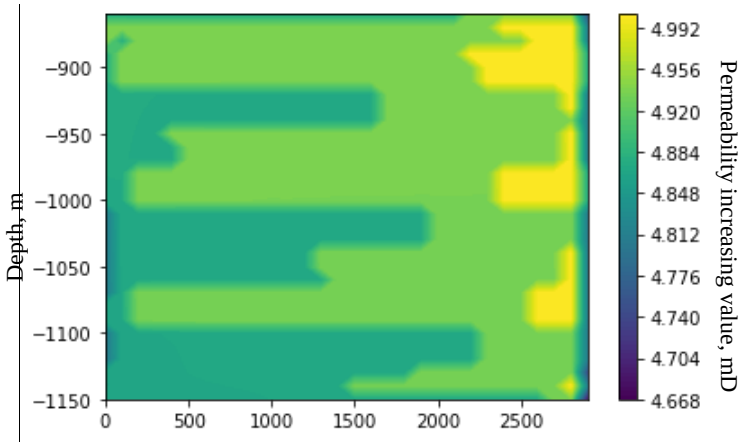

Figure 3-3 Aquifer permeability variation after injection

Fig. 3-4 shows the average pressure curves of three formation sections which are caprock, aquifer, and bed rock. At the end of a 10-year injection and a 10-year monitoring period, pressure differences in the ECLIPSE-only simulation occurred in three sections: 1.132, 0.436, and 1.036 bars. So, we see more significant geomechanical effects induced by pressure occur in the caprock and bed rock than that in the aquifer. Even the injection period ends, the geomechanical effect is getting stronger. This is because the increased pressure in the aquifer spreads through the caprock and bed rock. The pressure distribution

maps at the beginning of the injection and the end of the simulation are shown in Fig. 3-5. The dashed line represents the boundary of the aquifer. They demonstrate that pressure increases rapidly within the aquifer section and starts to spread to the over- and under-burden formation.

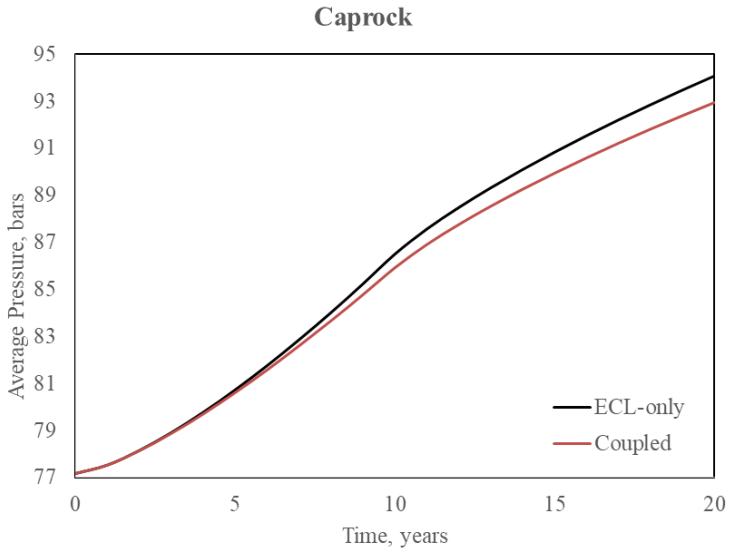

Figure 3-4a Average pressure of the caprock

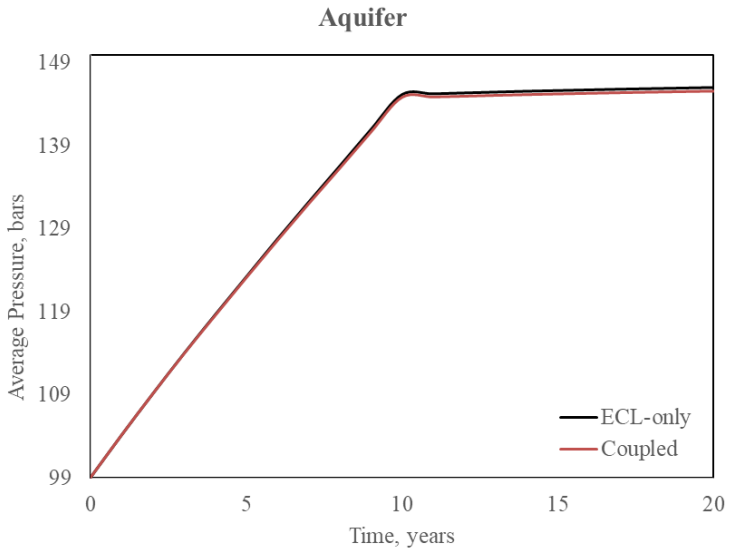

Figure 3-4b Average pressure of the aquifer

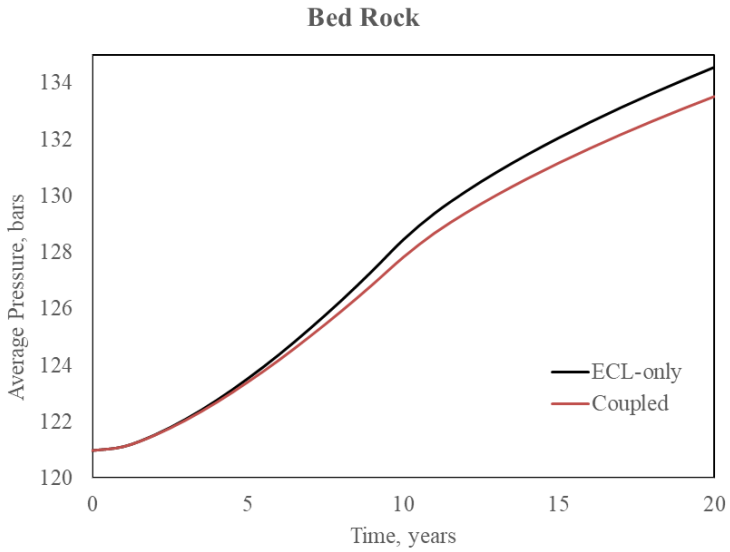

Figure 3-4c Average pressure of bed rock

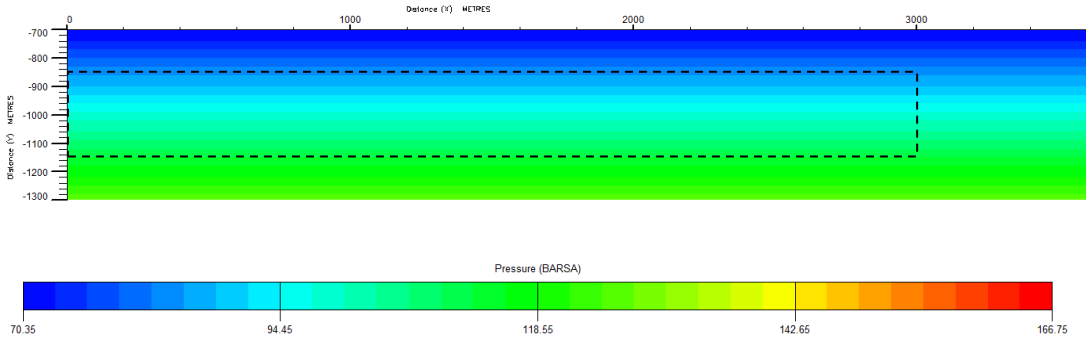

Figure 3-5a Initial pressure distribution

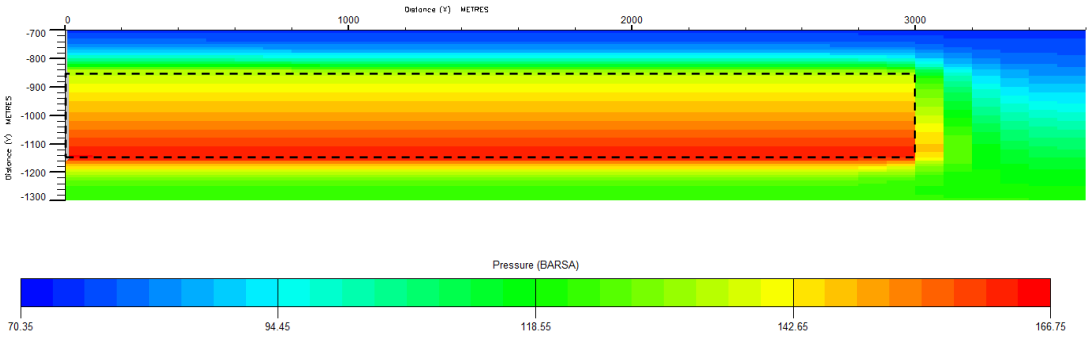

Figure 3-5b Pressure distribution after 10-year injection and 10-year monitoring

From Fig. 3-6, we can see temperature continues to drop during the injection, and the aquifer section has a larger temperature reduction due to the cold supercritical carbon dioxide. By comparison, the aquifer area has a larger temperature difference from the ECLIPSE-only results than that of the surrounding formation. Because of the temperature gradient between the aquifer and the surrounding formation, heat transfers to the aquifer. After the 10-year injection, heat continues to flow into the aquifer, which leads to increasing temperature in the aquifer and reduction in the surrounding formation.

Fig. 3-7 displays the temperature distribution before the injection and after a 20-year simulation. Because the whole model shares the same heat conductivity and heat capacity and their values are large, heat dissipates rapidly through the whole model, and temperature distributes averagely after the injection. However, we can find an apparent temperature gradient with a distance of 200m from the wellbore (see Fig. 3-7c). After 10-year injection and 10-year monitoring, the ground surface occurs deformation in the horizontal and vertical direction shown in Fig. 3-8. The largest movement is close to 0.4ft.

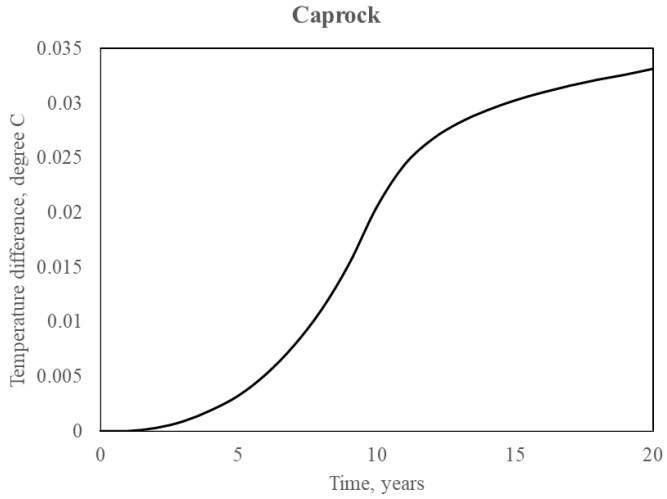

Figure 3-6a Average well-bore-vicinity temperature difference of caprock

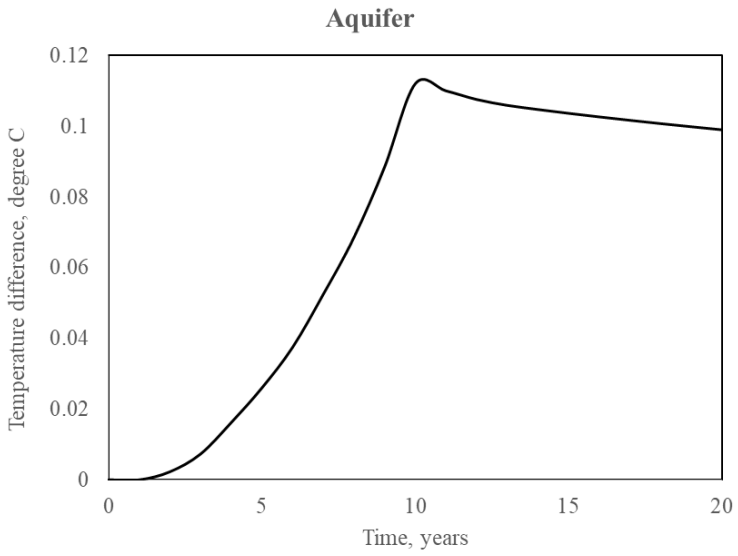

Figure 3-6b Average well-bore-vicinity temperature difference of aquifer

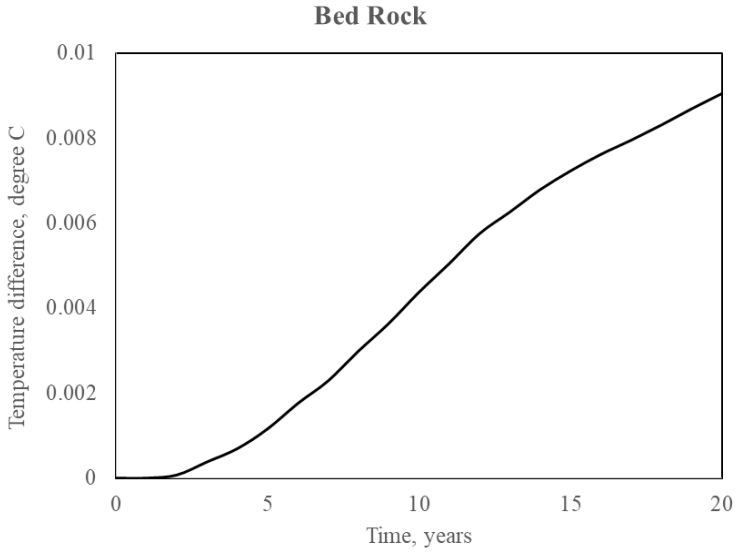

Figure 3-6c Average well-bore-vicinity temperature difference of bed rock

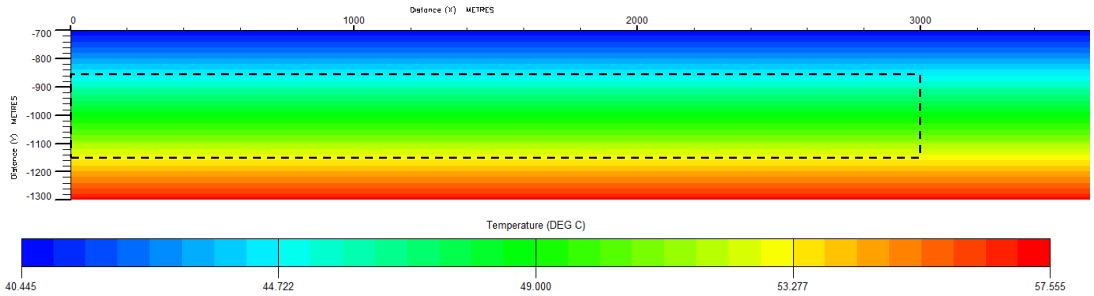

Figure 3-7a Temperature distribution before injection

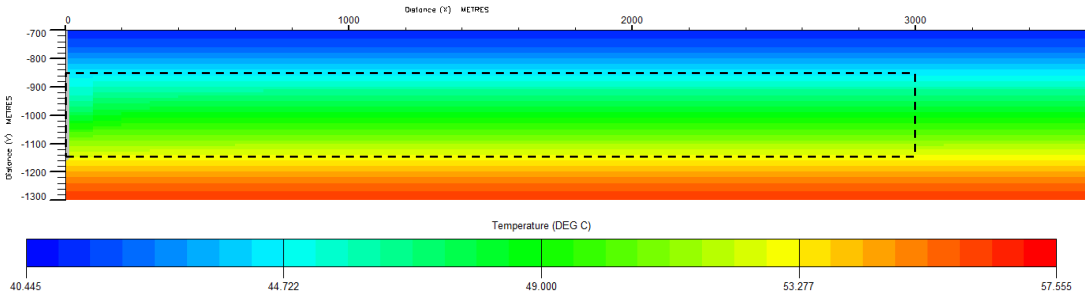

Figure 3-7b Temperature distribution after injection and monitoring

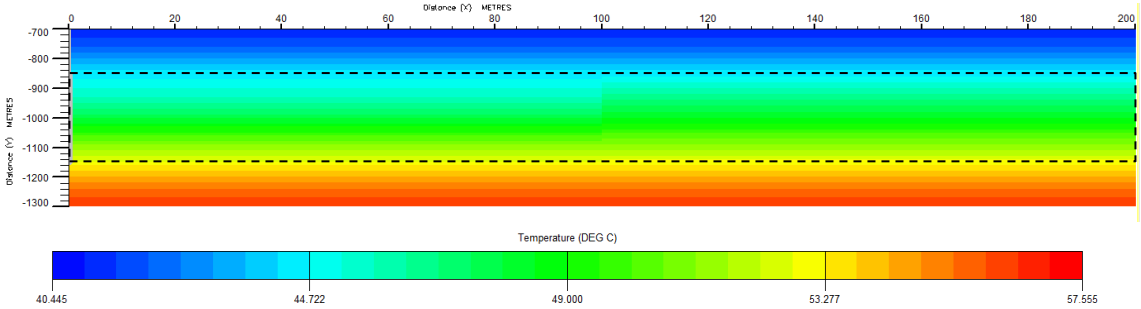

Figure 3-7c Temperature distribution after injection and monitoring within the distance of 200m

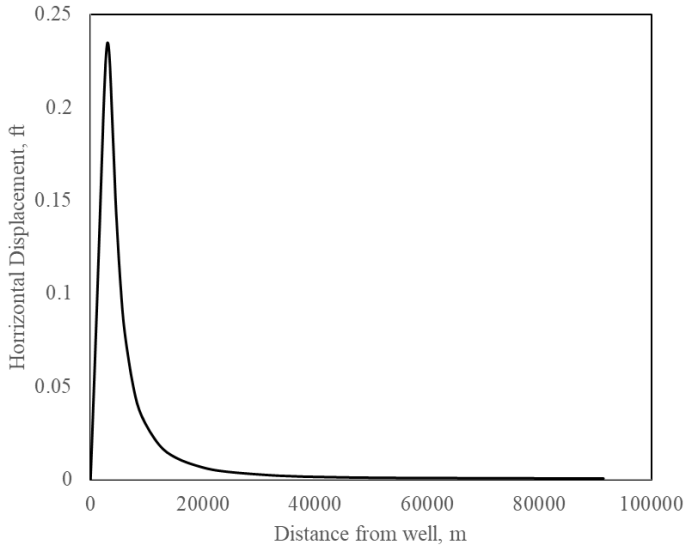

Figure 3-8a Horizontal displacement

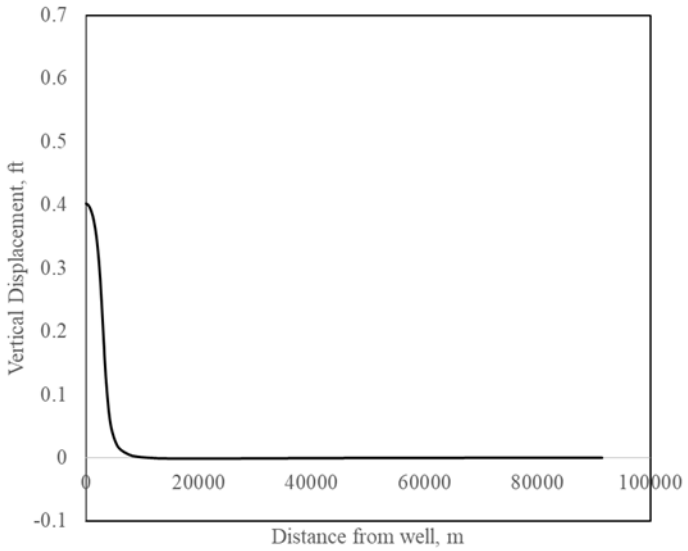

Figure 3-8b Vertical displacement

Case 2: Soft Aquifer Formation

In this case, the whole formation has the same Young's modules. Due to the injection of cold supercritical carbon dioxide, the formation pressure increases significantly, and

temperature reduces. Increasing pressure inclines to expand the pore volume and porosity, and, therefore, permeability would increase. Eq. (2-63) is applied to update permeability based on updated porosity values. Increasing permeability could reduce the resistance of fluid flow, and a lower injection pressure would be induced. The increasing permeability values can be found in Fig 3-9. Due to the increasing pore volume with a constant injection rate, the field pressure could be lower than the simulation without coupling with geomechanics effects.

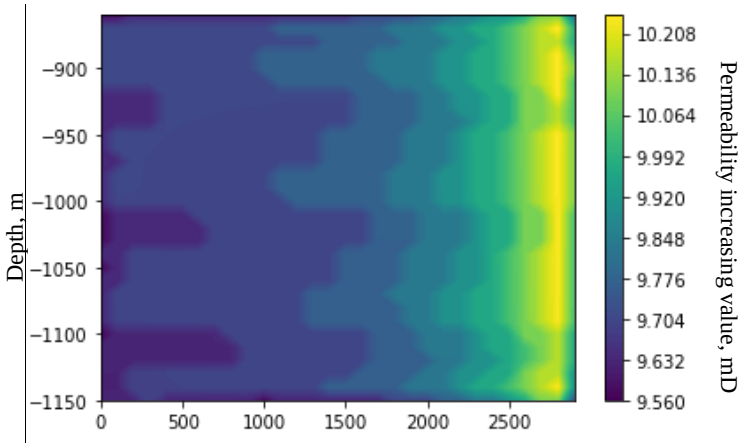

Figure 3-9 Permeability variation after injection

Fig. 3-10 shows the average pressure curves of three formation sections which are caprock, aquifer, and bed rock. At the end of a 10-year injection and a 10-year monitoring period, pressure differences from the ECLIPSE-only simulation occurred in three sections: 1.236, 0.752, and 1.166 bars. So, we see a more significant geomechanical effect induced by pressure occur in the caprock and bed rock than that in the aquifer. Even the injection period ends, the geomechanical effect is getting stronger. This is because the increased pressure in the aquifer spreads through the caprock and bed rock. The pressure distribution maps at the beginning of the injection and the end of the simulation are shown in Fig. 3-

11. The dashed line represents the boundary of the aquifer. They demonstrate that pressure increases rapidly within the aquifer section and starts to spread to the over- and under-burden formation.

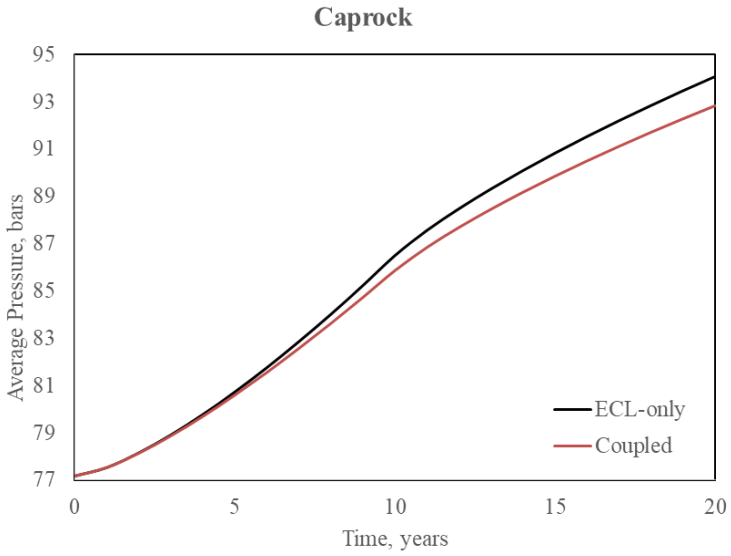

Figure 3-10a Average pressure of caprock

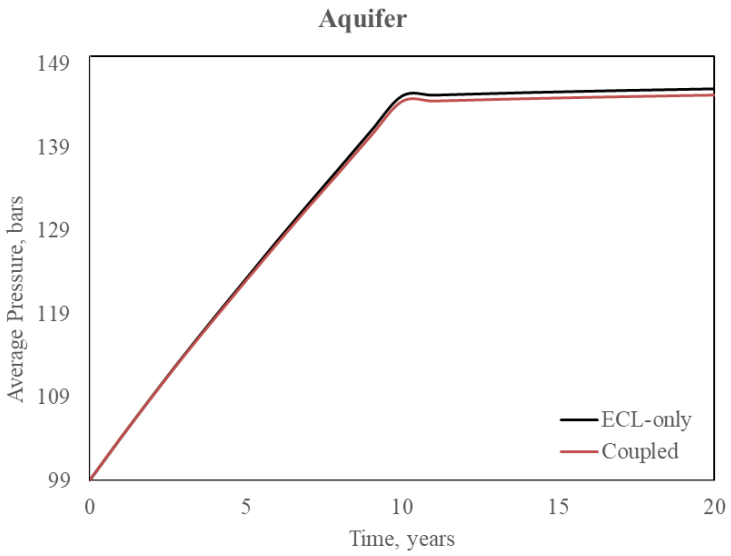

Figure 3-10b Average pressure of the aquifer

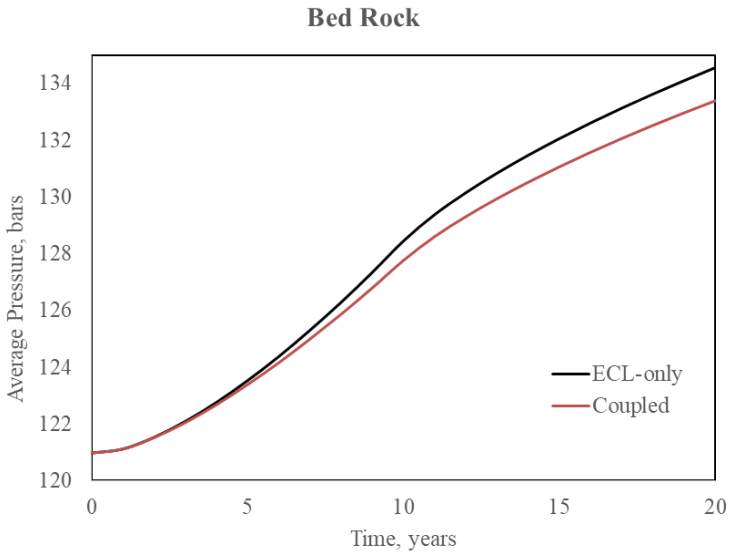

Figure 3-10c Average pressure of the bedrock

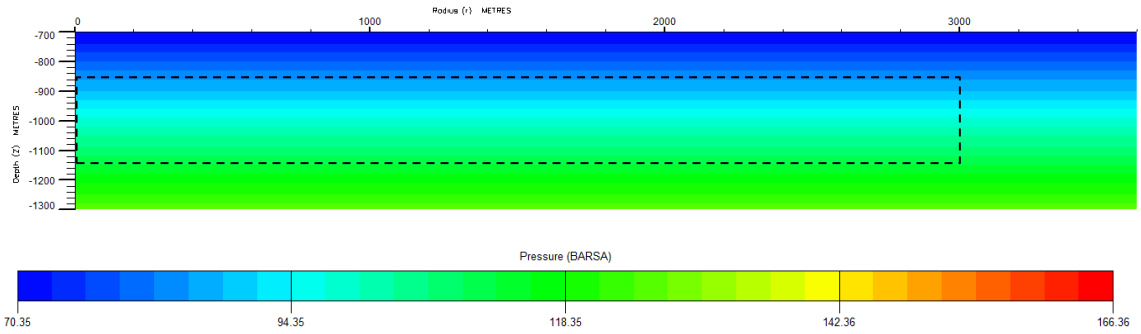

Figure 3-11a Initial pressure distribution

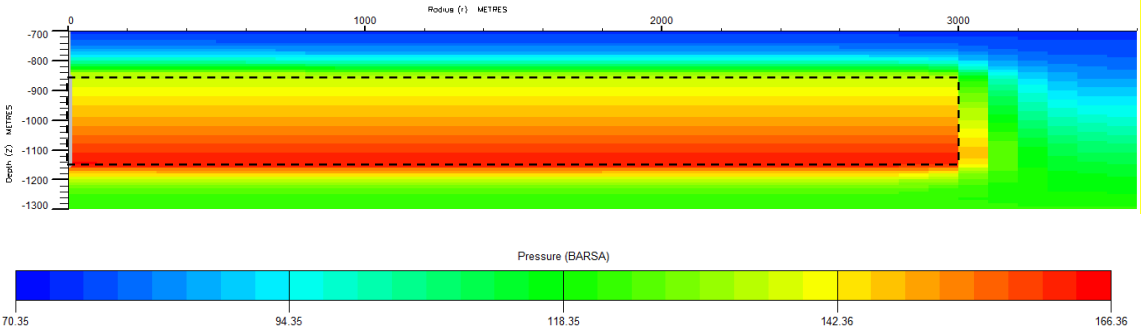

Figure 3-11b Pressure distribution after 10-year injection and 10-year monitoring

From Fig. 3-12, we can see temperature continues to drop during the injection, and the aquifer section has a larger temperature reduction due to the colder supercritical carbon dioxide. By comparison, the aquifer area has a larger temperature difference from the ECLIPSE-only results than that of the surrounding formation. Because of the temperature gradient between the aquifer and the surrounding formation, heat transfers to the aquifer. After the 10-year injection, heat continues to flow into the aquifer, which leads to increasing temperature in the aquifer and reduction in the surrounding formation.

Fig. 3-13 displays the temperature distribution before the injection and after a 20-year simulation. Because the whole model shares the same heat conductivity and heat capacity and their values are large, heat dissipates rapidly through the whole model, and temperature distributes averagely after the injection. However, we can find an apparent temperature gradient with a distance of 200m from the wellbore (see Fig. 3-13c).After 10-year injection and 10-year monitoring, the ground surface occurs deformation in the horizontal and vertical direction shown in Fig. 3-14. The largest movement is about 0.658ft in the vertical direction.

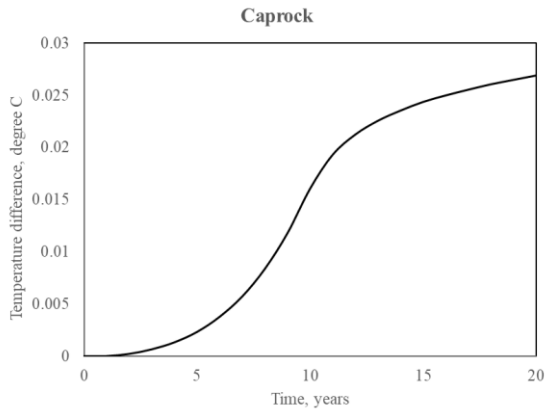

Figure 3-12a Average well-bore-vicinity temperature difference of caprock

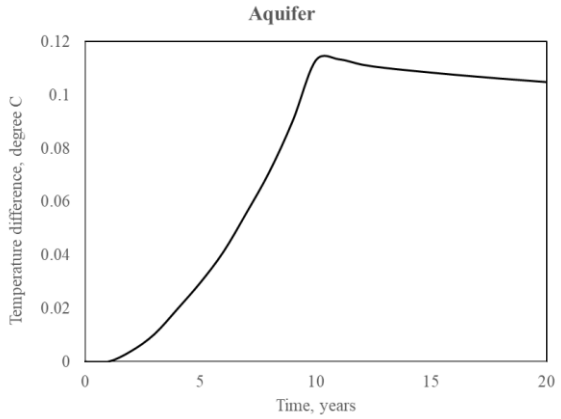

Figure 3-12b Average well-bore-vicinity temperature difference of aquifer

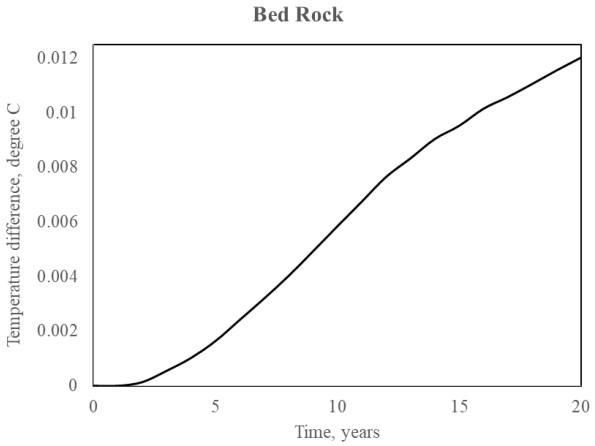

Figure 3-12c Average well-bore-vicinity temperature difference of bed rock

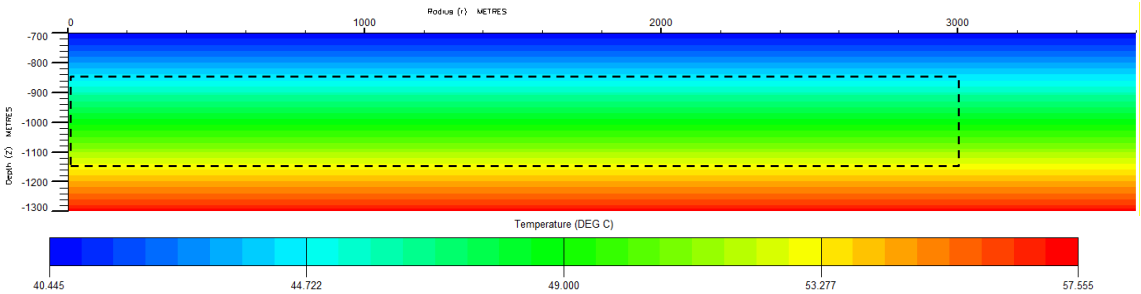

Figure 3-13a Temperature distribution before injection

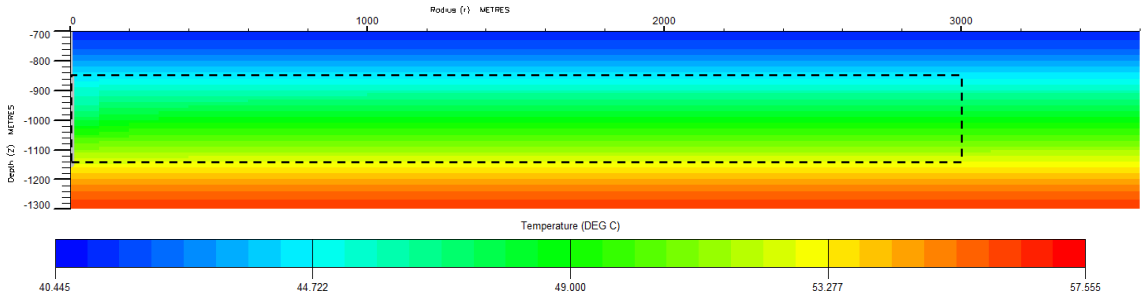

Figure 3-13b Temperature distribution after injection and monitoring

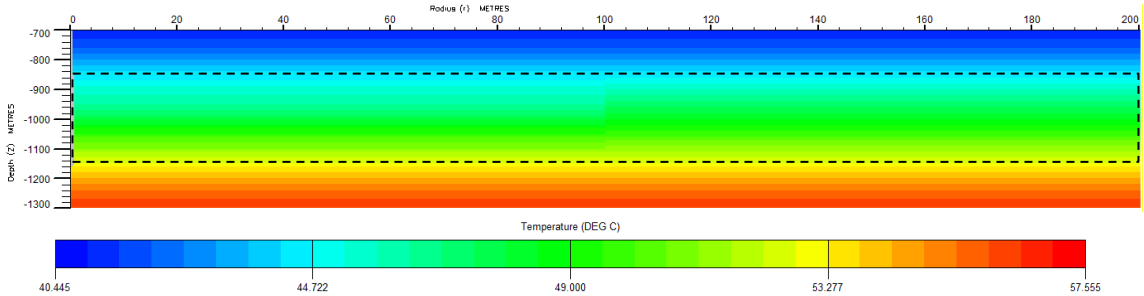

Figure 3-13c Temperature distribution after injection and monitoring within the distance of 200m

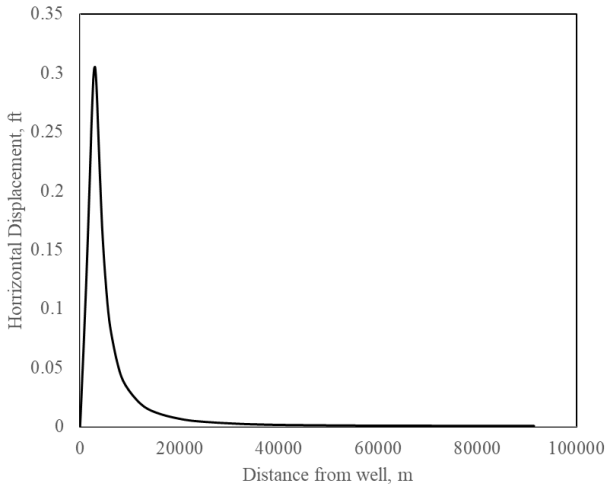

Figure 3-14a Horizontal displacement

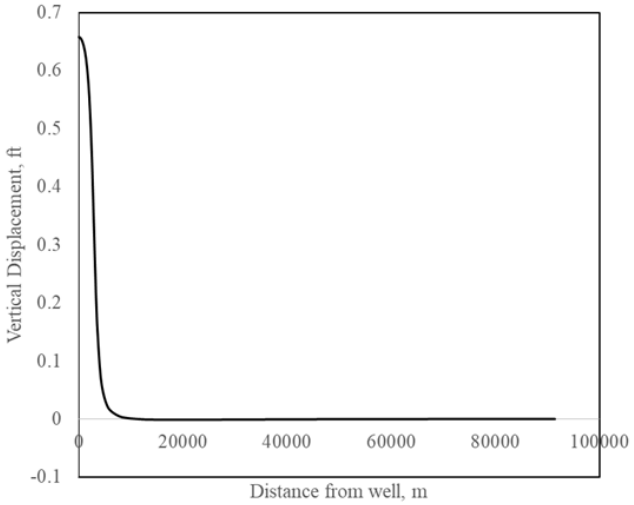

Figure 3-14b Vertical displacement

CHAPTER IV

FORMATION STABILITY ANALYSIS

In this chapter, we conducted six case studies which include two types of formation: homogeneous formation and formation with a soft aquifer. The soft aquifer has a smaller Young's module, which is half of the surrounding formation. In each type of formation, three types of initial stress states are involved, which are normal faulting, strike-slip faulting, and reverse faulting regimes. Then, the following equations are applied to calculate the limit value of minimum horizontal stress and maximum horizontal stress.

$$\text{Normal faulting: } \frac{\sigma_{max}^{e}}{\sigma_{min}^{e}} = \frac{S_v - P_p}{S_{hmin} - P_p} \leq \left[\sqrt{\mu^2 + 1} + \mu\right]^2 \tag{4-1a}$$

$$\text{Strike-slip faulting: } \frac{\sigma_{max}^{e}}{\sigma_{min}^{e}} = \frac{S_{Hmax} - P_p}{S_{hmin} - P_p} \leq \left[\sqrt{\mu^2 + 1} + \mu\right]^2 \tag{4-1b}$$

$$\text{Reverse faulting: } \frac{\sigma_{max}^{e}}{\sigma_{min}^{e}} = \frac{S_{Hmax} - P_p}{S_v - P_p} \leq \left[\sqrt{\mu^2 + 1} + \mu\right]^2 \tag{4-1c}$$

Where: μ is friction coefficient, 0.6, and $\left[\sqrt{\mu^2 + 1} + \mu\right]^2$ is defined as the limit of formation stability coefficient, 3.12.

Based on stress polygon and formation stability coefficient $\frac{\sigma_{max}^{e}}{\sigma_{min}^{e}}$, we will analyze the formation stability during and after carbon dioxide storage in water formation. The stability evaluation includes two aspects. One is to evaluate caprock, aquifer, and bedrock as a whole structure accordingly using the average formation stability coefficient. As shown in Fig. 4-0, the section with dash line is evaluated. For the caprock, the average value of the formation stability coefficient is taken from the upper part of the caprock. In

contrast, for the bedrock, the average value comes from the lower part of the bedrock. On the other hand, the formation stabilities at three evaluation sites from caprock, aquifer, and bedrock are evaluated by stress polygons, including the first site, which is close to the wellbore and the boundary between caprock and aquifer, the second site, which is close to the wellbore at the middle of the aquifer, and the third site, close to the wellbore, which locates at the boundary between the bedrock and the aquifer. Three evaluation sites are located by the red points in Fig. 4-1. In order to avoid the negative influence near the borehole, the first element was ignored when evaluating the formation stability. As the injection of supercritical CO2 progresses, the stress polygon would shrink, and the stress state would change. In stress polygon figures, the dash-line polygons represent the initial stress state, and the solid line represents the stress polygon at the specific injection year.

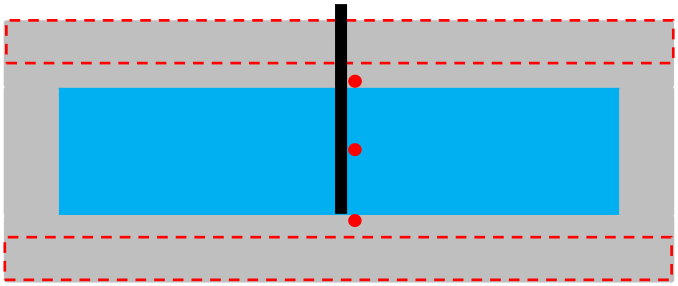

Figure 4-1 Evaluation sites of formation stability analysis

Homogeneous Formation

All parameters applied in simulations are the same as parameters in Chapter 3. Homogeneous Young's moduli are considered, so the aquifer and the surrounding formation have identical Young's moduli. Three faulting regimes will be evaluated.

Normal Faulting

For the normal faulting environment, $S_v \geq S_{Hmax} \geq S_{hmin}$ is applied on in situ stress, and the stress limits are shown in the following figure (Fig. 4-2). In the normal faulting environment in which pore pressure is hydrostatic, Eq. (4-1a) defines the lowest value of the minimum principal stress with depth. It is straightforward to show that in an area of critically stressed normal faults when pore pressure is hydrostatic, the lower bound value of the least principal stress S_{hmin}~$0.621S_v$, as illustrated by the heavy dashed line in Fig. 4-2. The magnitude of the least principal stress cannot be lower than this value because well-oriented normal faults would slip. The initial principal stress is S_{hmin}~$0.686S_v$ and S_{Hmax}~$0.885S_v$. After the injection and monitoring period for 20 years, the stress state changes in the caprock, aquifer, and bedrock section. In the following parts, three sections will be analyzed accordingly.

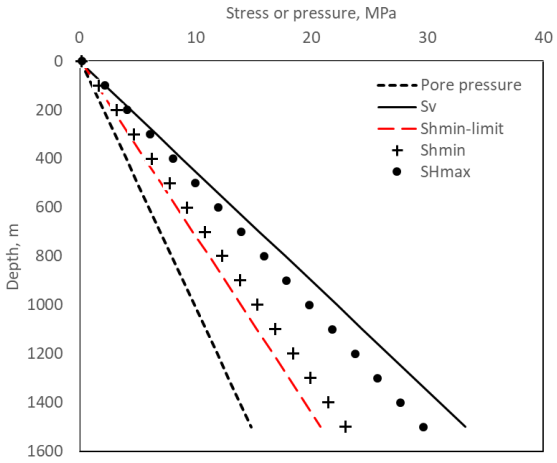

Figure 4-2 In situ stress and pore pressure for normal faulting environment

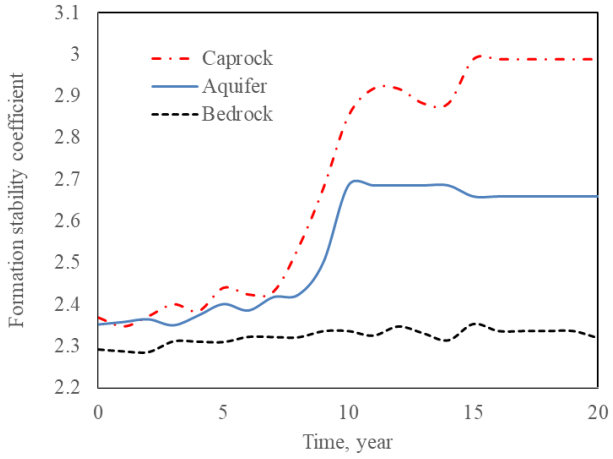

Figure 4-3 Formation stability coefficient at the evaluation sites for normal faulting environment

Caprock

During the injection and monitoring period, the horizontal and vertical effective stress keep reducing because the pore pressure increases both in reservoir section and cap rock. The vertical effective stress reduces at a slow rate during the 10-year injection. It reduces faster after the end of the injection period. For the horizontal effective stress, the injection period has a larger reduction rate than the monitoring period. The caprock became more and more unstable during the injection as the formation stability coefficient kept increasing. It started to stabilize during the monitoring period according to the slightly dropping formation stability coefficient. As shown in Fig. 4-4, the average formation stability coefficient (shown in the area of dash-line) did not reach the limit of the stability coefficient, 3.12. Therefore, the caprock remains intact in the given normal faulting environment. (Fig. 4-4)

Fig. 4-5 shows the stress polygons of the evaluation site of the caprock, close to the wellbore and the boundary between caprock and aquifer. As shown in Fig. 4-5a and b, this

evaluation site remains stable but the stress state keeps approaching the polygon periphery. After the end of the injection, the stress state became closer to induce faulting because the high pressure in the aquifer pushes the caprock, which would lead to instability (see Fig. 4-5c). This can also be found in Fig. 4-3. During the injection period, the formation stability coefficient increases to 2.8513. After this period, the coefficient continues to increase and reaches 2.9876 at the end of the monitoring period. So it can be found that the stress state at 20 years is closer to the periphery of the stress polygon than that at ten years. In contrast to the upper part of the caprock, the formation stability coefficient of the evaluation site at caprock is larger, indicating that the upper part of the caprock is more stable.

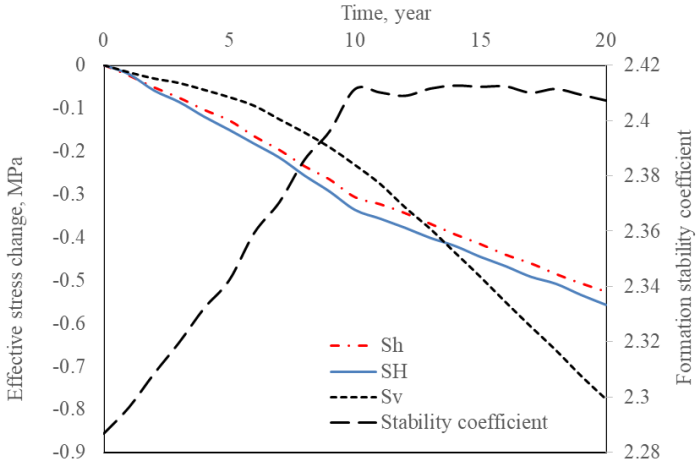

Figure 4-4 Effective stress and formation stability coefficient of caprock for normal faulting environment

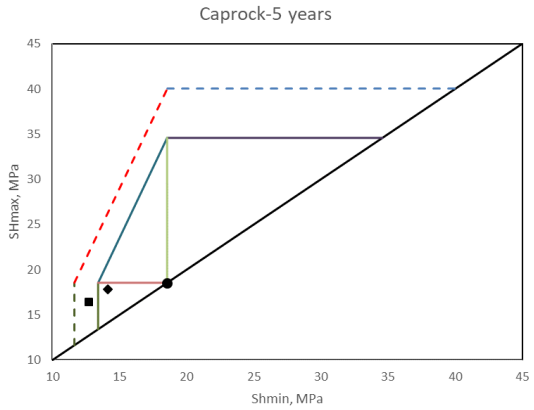

Figure 4-5a Stress polygon of caprock after 5-year injection

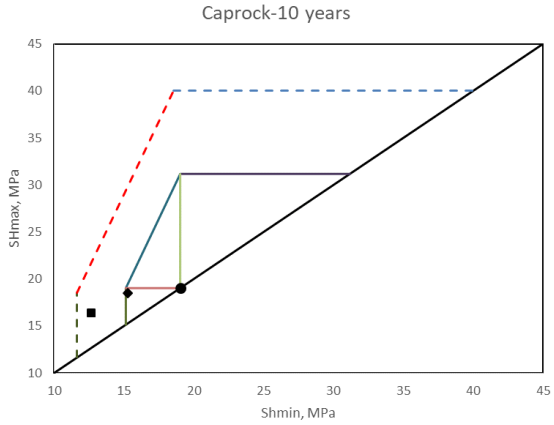

Figure 4-5b Stress polygon of caprock after 10-year injection

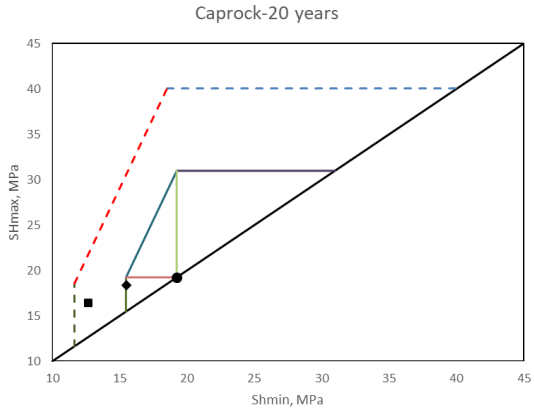

Figure 4-5c Stress polygon of caprock after the injection and monitoring period

Aquifer

During the injection period, the horizontal and vertical effective stresses keep reducing. By comparison, the vertical effective stress has a larger reduction than the horizontal effective stress. After the 10-year injection, the effective stress slightly bounces back. It then becomes nearly constant, indicating that formation stability increases at the beginning of the monitoring period, but the stability remains similar in the following years. This result can also be concluded by the formation stability coefficient. Fig. 4-6 illustrates that the formation stability coefficient of the aquifer continues to rise during the injection period and drops slightly at the beginning of the monitoring period before remaining constant. At the end of the simulation, faults are not induced, and the aquifer is still intact after injection and monitoring periods. Fig. 4-3 indicates that the evaluation site at the aquifer is more inclined to induce seismic events than the aquifer as a whole structure.

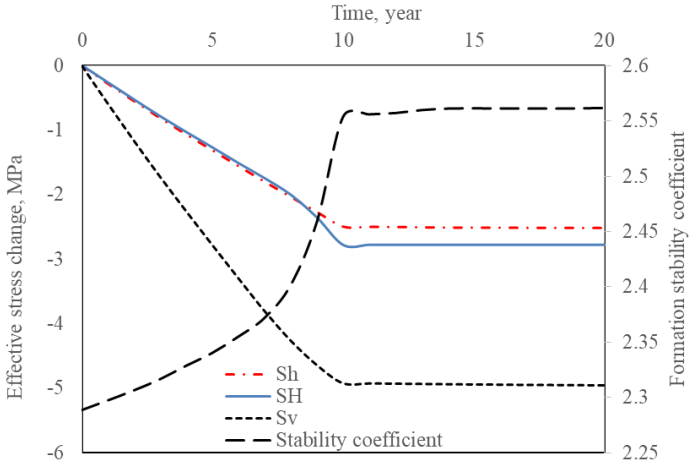

Figure 4-6 Effective stress and formation stability coefficient of the aquifer for normal faulting environment

Fig. 4-7 shows the stress polygons of the evaluation site of the aquifer. As shown in Fig. 4-7a and b, this evaluation site remains stable, but the stress state keeps approaching the

polygon periphery during the injection period. And the stability coefficient in Fig. 4-3 indicates the same result and reaches 2.6854 at ten years. After the injection period, the stress state in Fig 4-7c moves away from the stress polygon periphery, and the formation stability coefficient decreases to 2.6590, indicating enhancing formation stability.

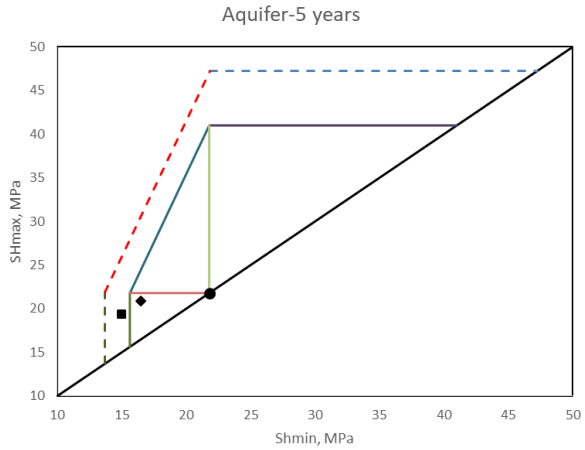

Figure 4-7a Stress polygon of aquifer after 5-year injection

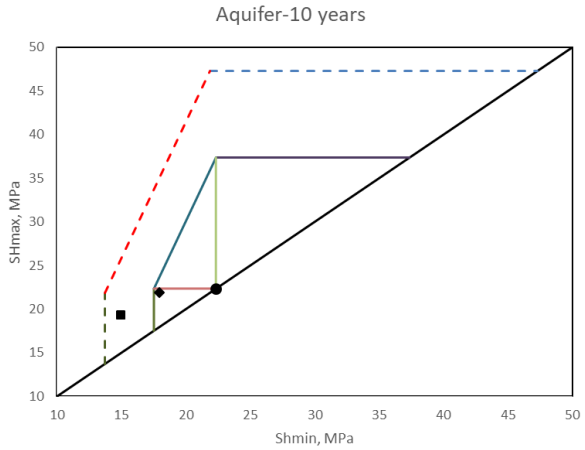

Figure 4-7b Stress polygon of aquifer after 10-year injection

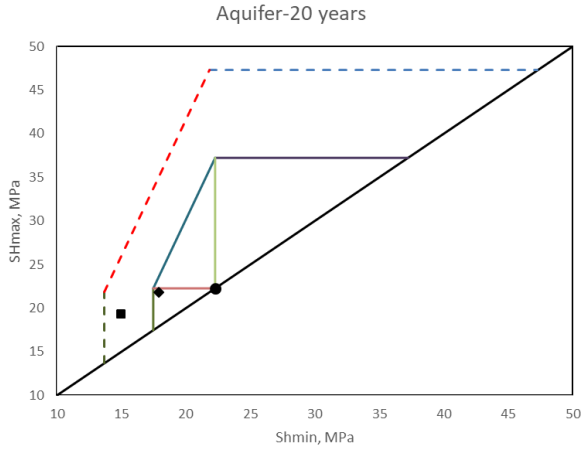

Figure 4-7c Stress polygon of aquifer after the injection and monitoring period

Bedrock

Fig. 4-8 shows that the horizontal effective stress reduces during the injection and monitoring periods, and the vertical stress increases before reduction at the sixth year of the injection period. The formation stability coefficient continuously increases during the whole simulation, indicating increasing formation instability. However, the bedrock remains stable at the end of the simulation.

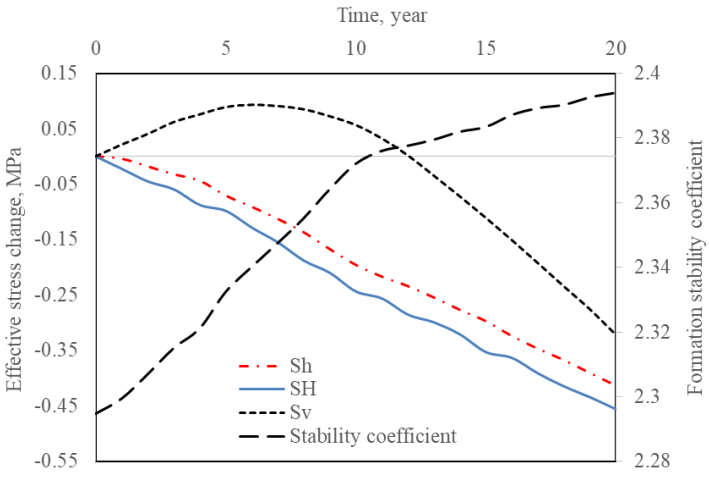

Figure 4-8 Effective stress and formation stability coefficient of bedrock for normal faulting environment

As shown in Fig. 4-3, the formation stability continues to increase after the injection period, and the bedrock evaluation site remains stable during the injection and monitoring period. As shown in Fig. 4-9, the stress state is inclined to switch to the strike-slip faulting environment. At last, the stress state does not cross the stress polygon, and the formation is stable at this time.

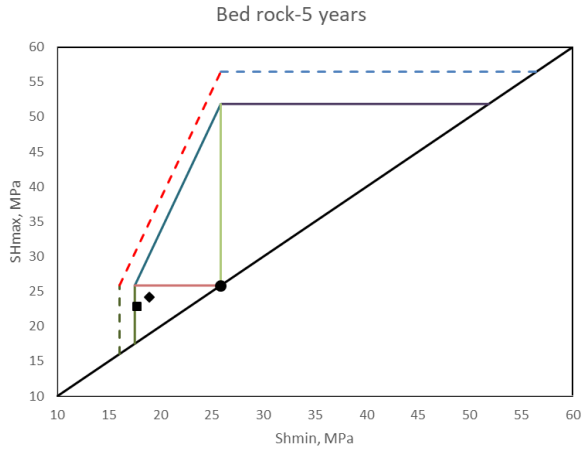

Figure 4-9a Stress polygon of bedrock after 5-year injection

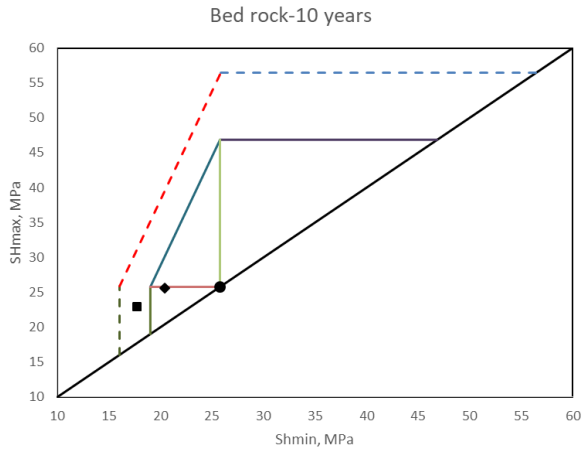

Figure 4-9b Stress polygon of bedrock after 10-year injection

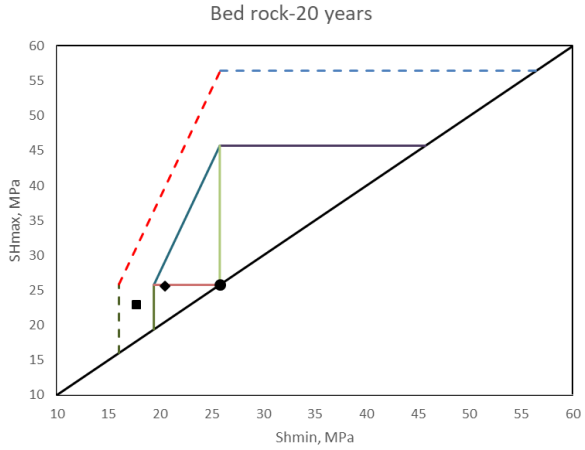

Figure 4-9c Stress polygon of bedrock after the injection and monitoring

Strike-Slip Faulting

For the strike-slip faulting environment, $S_{Hmax} \geq S_v \geq S_{hmin}$ is applied on in situ stress, and stress limits are shown in the following figure (Fig. 4-10). In the strike-slip faulting environment in which pore pressure is hydrostatic, Eq. (4-1b) defines the highest value of the maximum principal stress and the lowest value of the minimum principal stress with depth. The maximum value of S_{Hmax} depends on the magnitude of the minimum horizontal stress, S_{hmin}. If the value of the minimum principal stress is known, Eq. (4-1b) can be used to put an upper bound on S_{Hmax}. When pore pressure is hydrostatic, the upper bound value of the largest principal stress S_{Hmax}~$1.41S_v$ and the lower bound value of the least principal stress S_{hmin}~$0.669S_v$, as illustrated by the red dashed line in Fig. 4-10. The initial principal stresses are S_{hmin}~$0.752S_v$ and S_{Hmax}~$1.15S_v$. After the injection and monitoring period for 20 years, the stress state changes in the caprock, aquifer, and bedrock section. In the following parts, three sections will be analyzed accordingly.

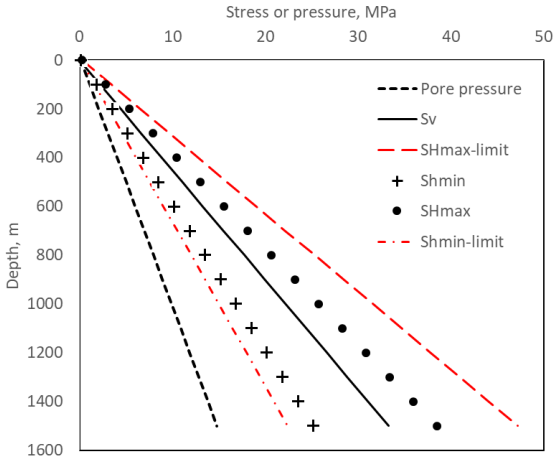

Figure 4-10 In situ stress and pore pressure for strike-slip faulting environment

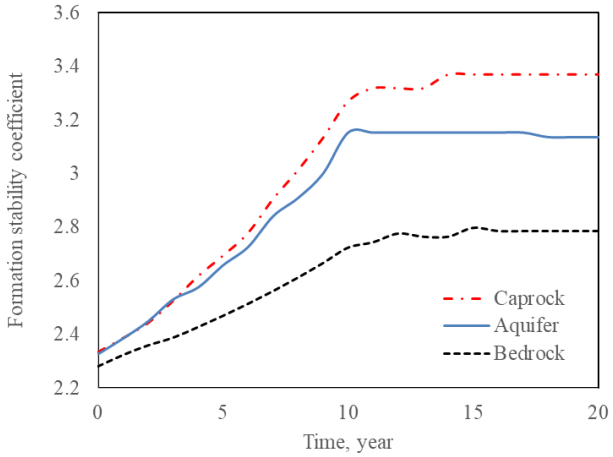

Figure 4-11 Formation stability coefficient at the evaluation sites for strike-slip faulting environment

Caprock

In Fig. 4-12, the effective stresses reduce through the 20-year simulation, and the reduction rate of the horizontal effective stresses becomes smaller when the monitoring period starts. In contrast, the vertical effective stress decreases at a higher rate when the monitoring period starts. By comparison, the vertical effective stress has a larger reduction. The formation stability coefficient continuously rises during the injection and monitoring period, and its increasing rate almost keeps constant. For the whole caprock, it is stable and intact since the average formation stability coefficient is less than 3.12.

At the fifth year of the injection, the evaluation site at the caprock is stable, and no faults would be activated at the evaluation site because the stress state is shown in Fig. 4-13a stays in the stress polygon, and the stability coefficient in Fig. 4-11 is 2.6939. Fig. 4-13b demonstrates that the stress state falls out of the stress polygon and the stability coefficient is 3.2685. So we can conclude that the strike-slip fault is activated before the end of the injection at the evaluation point of the caprock though the caprock structure as a whole is

intact. During the monitoring period, the stability coefficient of the evaluation site increases to 3.3689, which is much higher than its average value of the lower bedrock, and this site becomes more unstable.

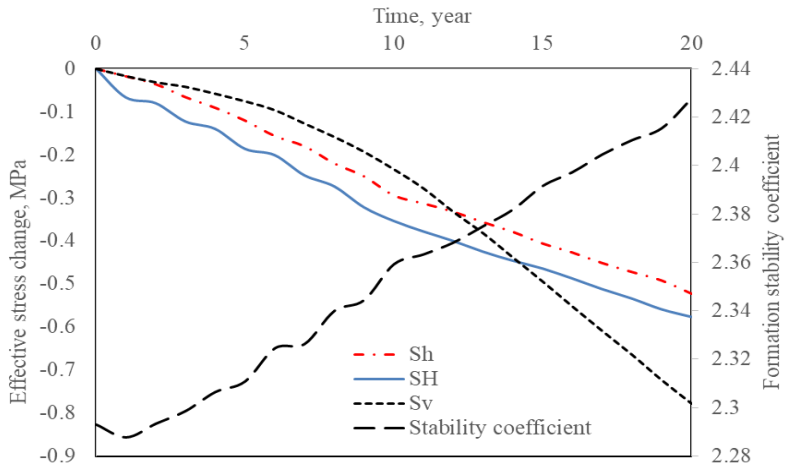

Figure 4-12 Effective stress and formation stability coefficient of caprock for strike-slip faulting environment

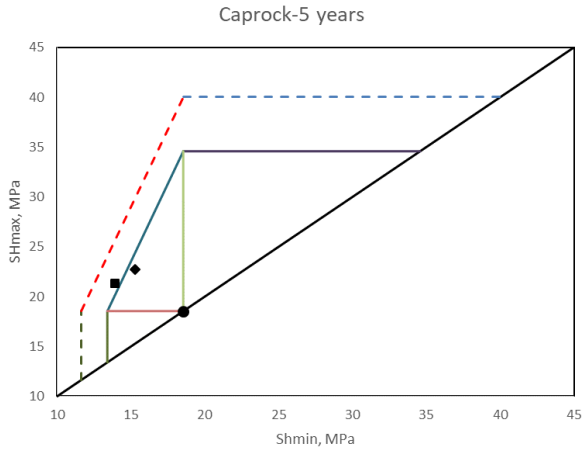

Figure 4-13a Stress polygon of caprock after 5-year injection

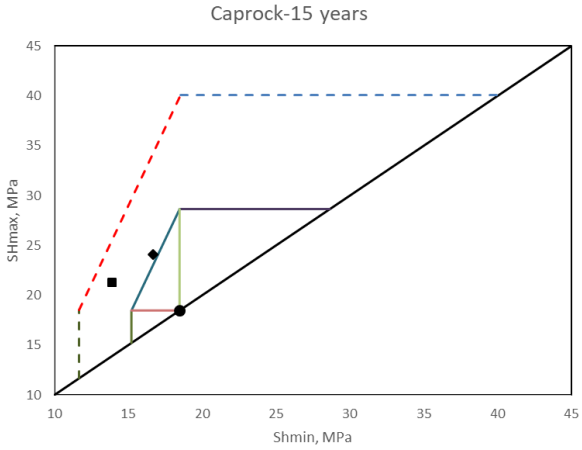

Figure 4-13b Stress polygon of caprock after 10-year injection

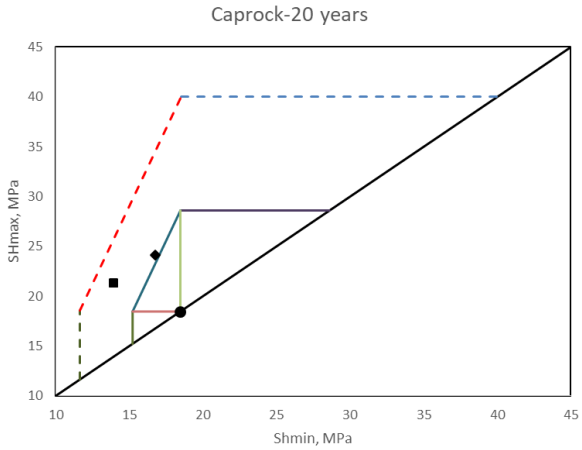

Figure 4-13c Stress polygon of caprock after the injection and monitoring period

Aquifer

During the injection period, the horizontal and vertical effective stresses keep reducing. By comparison, the vertical effective stress has a larger reduction than the horizontal effective stress. After the 10-year injection, the effective stress slightly bounces back and then becomes nearly constant, which indicates formation stability increasing at the beginning of the monitoring period, and the stability is kept in the following years. This

can also be concluded by the formation stability coefficient. Fig. 4-14 illustrates that the formation stability coefficient of the aquifer continues to rise during the injection period and drops slightly at the beginning of the monitoring period before being constant. At the end of the simulation, faulting is close to happening since the stability coefficient is over 3.03, which is approaching the limit, and the aquifer is still intact after injection and during monitoring period. (Fig 4-14)

At the fifth year of the injection, as shown in Fig 4-15a, the stress state of the evaluation site of the caprock has not moved across the stress polygon boundary, so this evaluation site is still stable, and no faults would be activated. This conclusion can be confirmed by Fig. 4-11, and the figure shows that the stability coefficient is 2.6585 at five years. The coefficient overrides 3.12 and reaches 3.1535 after the ninth injection year. Fig. 4-15b indicates that the strike-slip fault is activated before the end of the injection at the evaluation point of the aquifer. During the monitoring period, the stress state inclines to fall back into the polygon periphery, and the stability coefficient decreases to 3.1365 in Fig. 4-11.

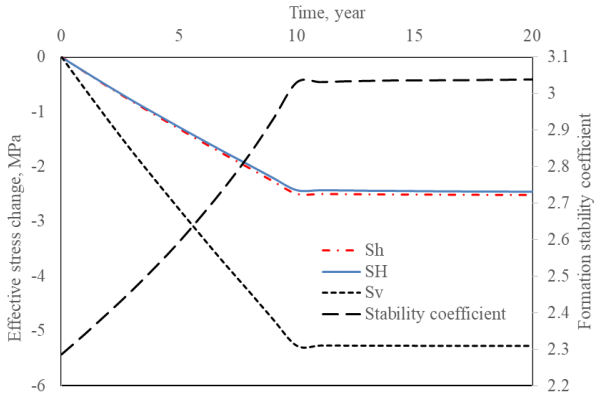

Figure 4-14 Effective stress and formation stability coefficient of the aquifer for strike-slip faulting environment

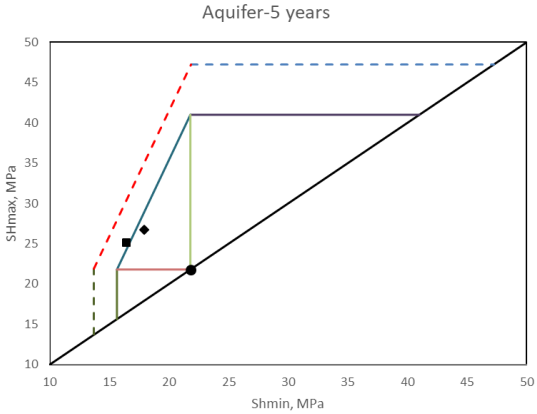

Figure 4-15a Stress polygon of aquifer after 5-year injection

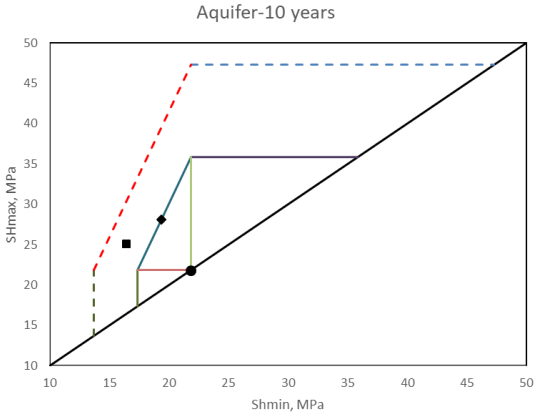

Figure 4-15b Stress polygon of aquifer after 10-year injection

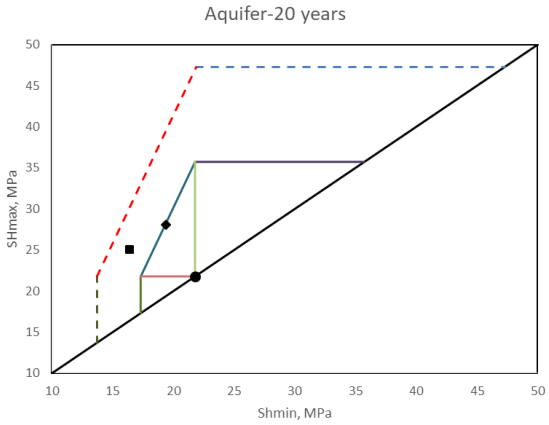

Figure 4-15c Stress polygon of aquifer after the injection and monitoring period

Bedrock

Fig. 4-16 shows that the horizontal effective stress reduces during the injection and monitoring period, and the vertical stress increases before reducing at the sixth year of the injection period. The formation stability coefficient continuously increases during the whole simulation, which indicates increasing formation instability. However, the bedrock remains intact at the end of the simulation as the formation stability coefficient is less than 3.12.

As shown in Fig. 4-17, the bedrock evaluation site remains stable during the injection and monitoring period. Strike-slip faulting is unlikely to be activated at this evaluation site through the simulation. We can confirm this conclusion by Fig. 4-11. The stress state moves toward the stress polygon periphery, and Fig. 4-11 also shows an increasing stability coefficient during the monitoring period.

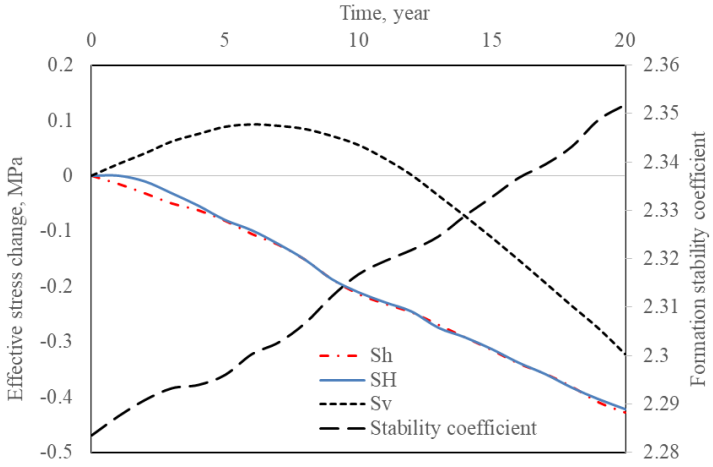

Figure 4-16 Effective stress and formation stability coefficient of bedrock for strike-slip faulting environment

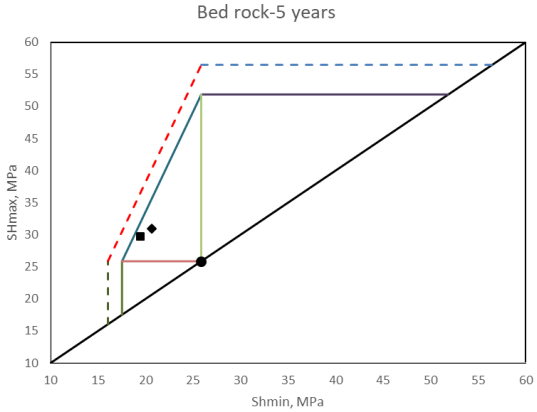

Figure 4-17a Stress polygon of bedrock after 5-year injection

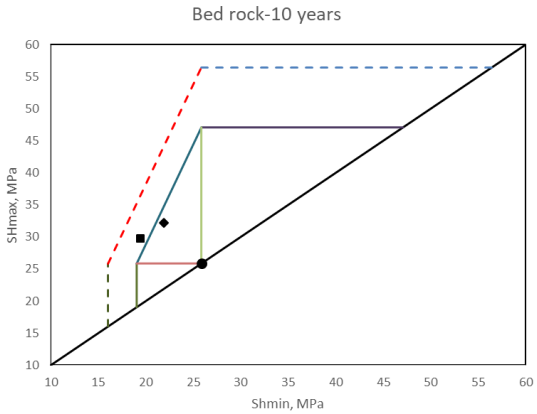

Figure 4-17b Stress polygon of bedrock after 10-year injection

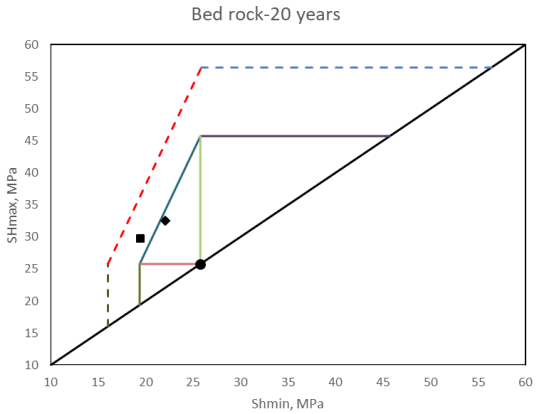

Figure 4-17c Stress polygon of bedrock after the injection and monitoring

Reverse Faulting

For the reverse faulting environment, $S_{Hmax} \geq S_{hmin} \geq S_v$ is applied on in situ stress, and stress limits are shown in the following figure (Fig. 4-18). In the reverse faulting environment in which pore pressure is hydrostatic, Eq. (4-1c) defines the highest value of the maximum principal stress with depth. When pore pressure is hydrostatic, the upper bound value of the largest principal stress S_{Hmax}~$2.18S_v$, as illustrated by the red dashed line in Fig. 4-18. The magnitude of the maximum principal stress cannot be high than this value because reverse faults would slip. The initial principal stress is S_{hmin}~$1.460S_v$ and S_{Hmax}~$1.991S_v$. After the injection and monitoring period for 20 years, the stress state changes in the caprock, aquifer, and bedrock section. In the following parts, three sections will be analyzed accordingly.

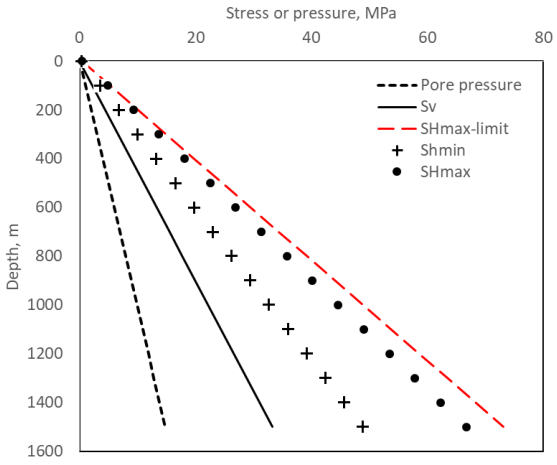

Figure 4-18 In situ stress and pore pressure for reverse faulting environment

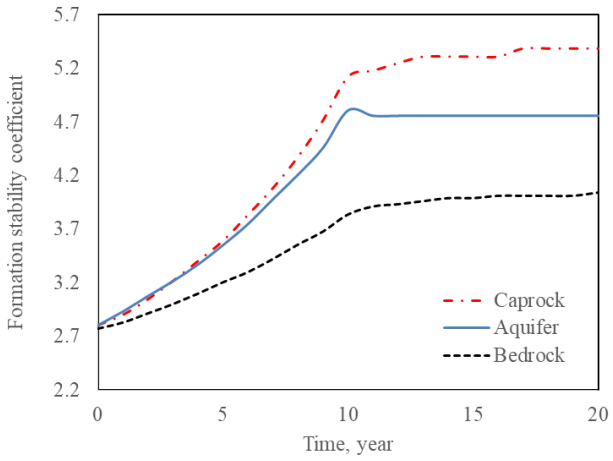

Figure 4-19 Formation stability coefficient at the evaluation sites for reverse faulting environment

Caprock

In Fig. 4-20, the effective stresses reduce through the 20-year simulation, and the reduction rate of the horizontal effective stresses becomes smaller when the monitoring period starts, while the vertical effective stress decreases at a higher rate when the monitoring period starts. By comparison, the vertical effective stress has a more considerable reduction. The formation stability coefficient continuously rises during the injection and monitoring period, and its increasing rate becomes higher after the injection. For the whole caprock, it is stable and intact since the average formation stability coefficient is less than 3.12.

At the fifth year of the injection, as shown in Fig 4-21a, the reverse fault has been activated at the evaluation site of the caprock before this checkpoint, and the formation stability coefficient is 3.5960. Fig. 4-19 indicates that the seismic event happened during the second year. The stress state approaches the stress polygon profile in Fig. 4-21b and c. The formation stability coefficient reaches 5.1258 at ten years and increases to 5.3895 at 20 years.

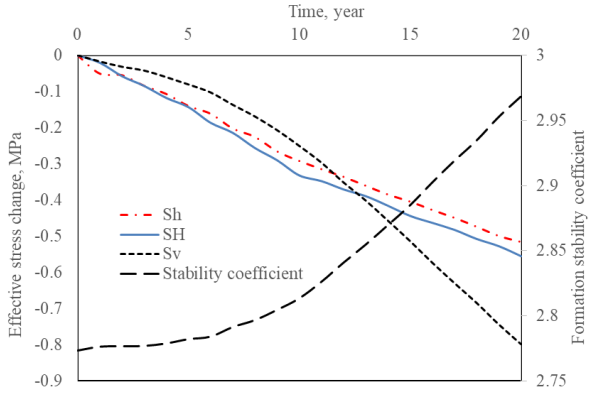

Figure 4-20 Effective stress and formation stability coefficient of caprock for reverse faulting environment

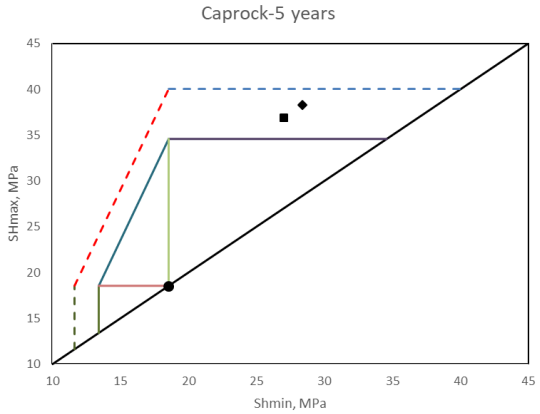

Figure 4-21a Stress polygon of caprock after 5-year injection

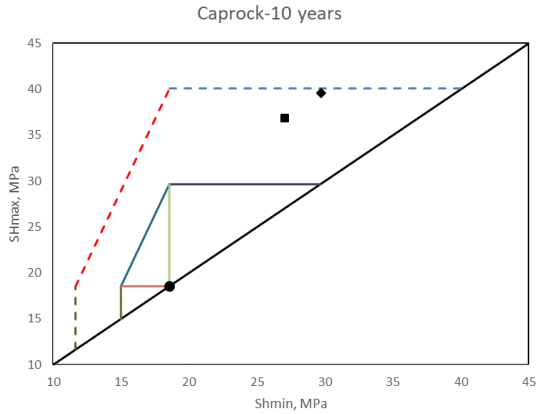

Figure 4-21b Stress polygon of caprock after 10-year injection

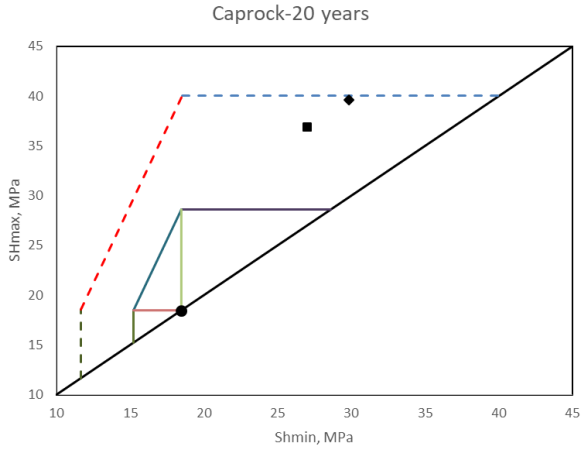

Figure 4-21c Stress polygon of caprock after the injection and monitoring period

Aquifer

During the injection period, the horizontal and vertical effective stress keeps reducing. By comparison, the vertical effective stress has a larger reduction than the horizontal effective stress. After the 10-year injection, the effective stress slightly bounces back and then becomes nearly constant, which indicates formation stability increasing at the beginning of the monitoring period, and the stability is kept in the following years. This result can also be concluded by the formation stability coefficient. Fig. 4-22 illustrates that the formation stability coefficient of the aquifer continues to rise during the injection period and drops slightly at the beginning of the monitoring period before being constant. Before the third year of the injection period, the formation stability coefficient becomes larger than its limit, which indicates that reverse fault is activated through the aquifer. (Fig 4-22) At the fifth year of the injection, as shown in Fig 4-23a, the reverse fault has been activated at the evaluation site of the aquifer before this checkpoint, and the formation stability coefficient is 3.5535 in Fig. 19. The seismic event occurred during the second year of the

injection period. Fig. 4-23b and c suggest that the reverse fault continues to develop in the following years at the evaluation site. The formation stability coefficient reaches 4.8096 at the end of the injection period. However, during the monitoring period, the stability coefficient decreases to 4.7589, and, therefore, the aquifer formation is inclined to stabilize.

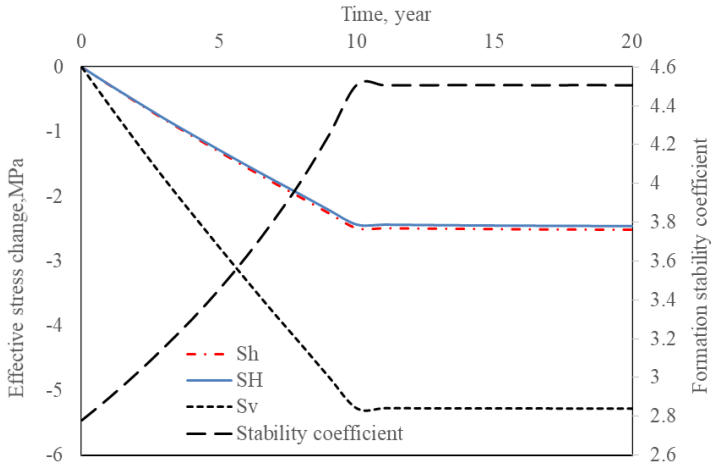

Figure 4-22 Effective stress and formation stability coefficient of the aquifer for reverse faulting environment

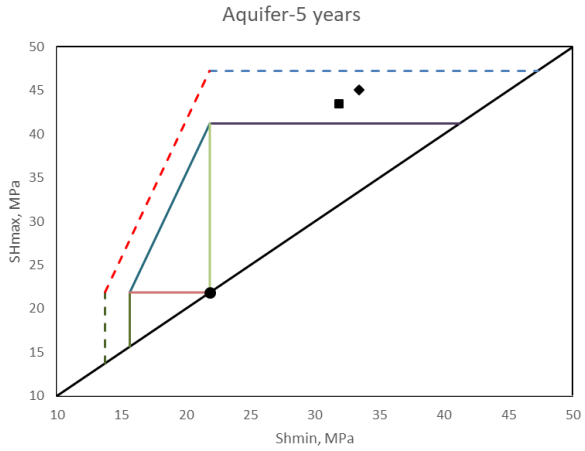

Figure 4-23a Stress polygon of aquifer after 5-year injection

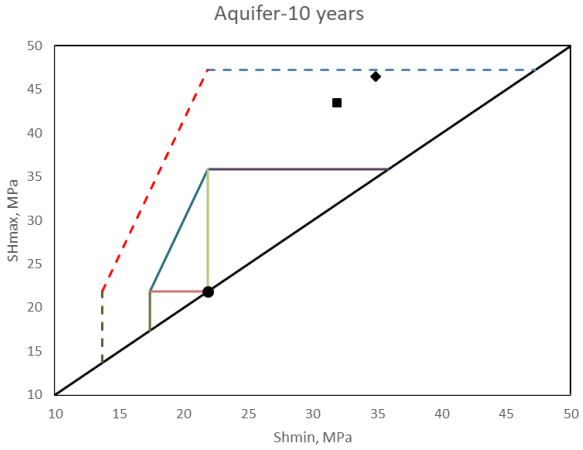

Figure 4-23b Stress polygon of aquifer after 10-year injection

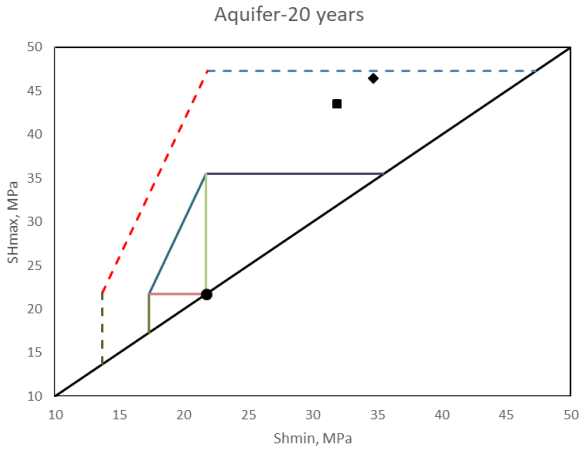

Figure 4-23c Stress polygon of aquifer after the injection and monitoring period

Bedrock

Fig. 4-24 shows that the horizontal effective stress reduces during the injection and monitoring period, and the vertical stress increases before reducing at the sixth year of the injection period. The formation stability coefficient decreases before starting to increase at the eighth year of the injection period, which indicates the bedrock is getting stable first

and then tends to get unstable. However, the bedrock remains intact at the end of the simulation as the formation stability coefficient is less than 3.12.

At the fifth year of the injection, as shown in Fig 4-25a, the reverse fault has been activated at the evaluation site of the aquifer before this checkpoint. The formation stability coefficient reaches 3.0993 at the fourth injection year, and the seismic event happens. The stability coefficient reaches 3.8383 at the end of the injection period. Fig. 4-25b and c suggest that the reverse fault continues to develop in the following years at the evaluation site. The stability coefficient continues to increase during the monitoring period and reaches 4.0429 at 20 years.

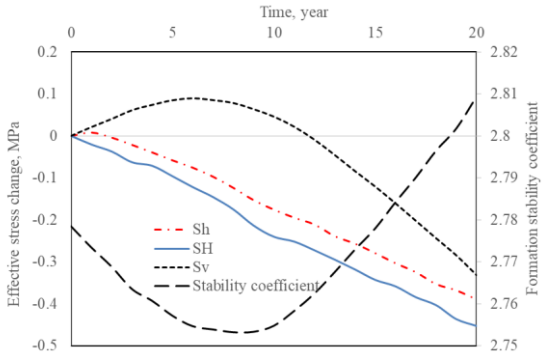

Figure 4-24 Effective stress and formation stability coefficient of bedrock for reverse faulting environment

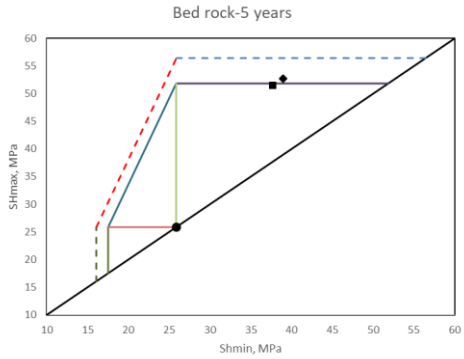

Figure 4-25a Stress polygon of bedrock after 5-year injection

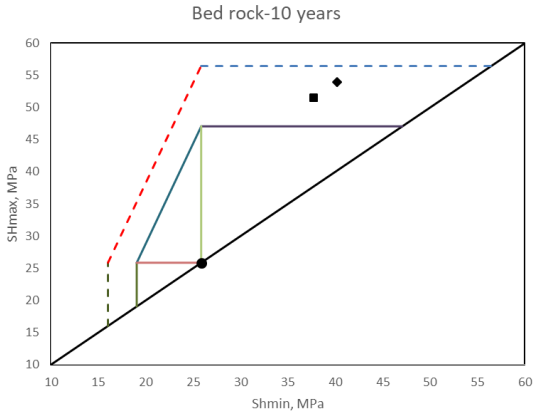

Figure 4-25b Stress polygon of bedrock after 10-year injection

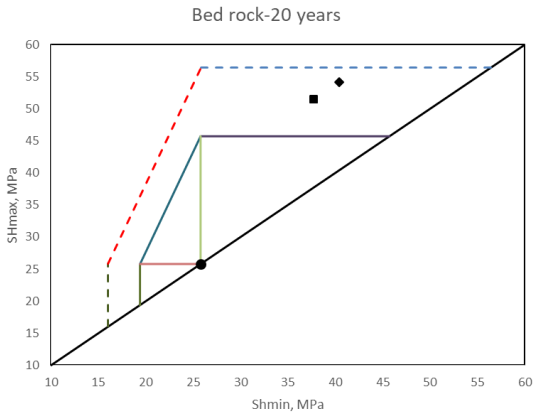

Figure 4-25c Stress polygon of bedrock after the injection and monitoring

Soft Aquifer

In this part, all parameters applied in simulations are the same as parameters in Chapter 3. Aquifer rock is softer than the surrounding formation, so Young's module of the aquifer is half of that of the surrounding area. Three types of faulting environments will be evaluated accordingly.

Normal Faulting

For the normal faulting environment, $S_v \geq S_{Hmax} \geq S_{hmin}$ is applied on in situ stress, and stress limits are shown in the following figure (Fig. 4-26). In the normal faulting environment in which pore pressure is hydrostatic, Eq. (4-1a) defines the lowest value of the minimum principal stress with depth. It is straightforward to show that in an area of critically stressed normal faults when pore pressure is hydrostatic, the lower bound value of the least principal stress S_{hmin}~$0.621S_v$, as illustrated by the heavy dashed line in Fig. 4-26. The magnitude of the least principal stress cannot be lower than this value because well-oriented normal faults would slip. The initial principal stress is S_{hmin}~$0.686S_v$ and S_{Hmax}~$0.885S_v$. After the injection and monitoring period for 20 years, the stress state changes in the caprock, aquifer, and bedrock section. In the following parts, three sections will be analyzed accordingly.

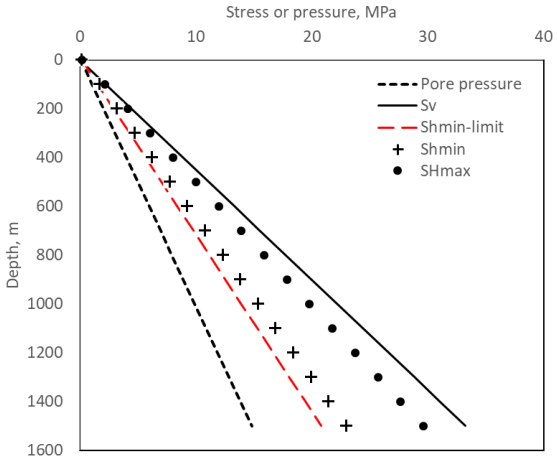

Figure 4-26 In situ stress and pore pressure for normal faulting environment

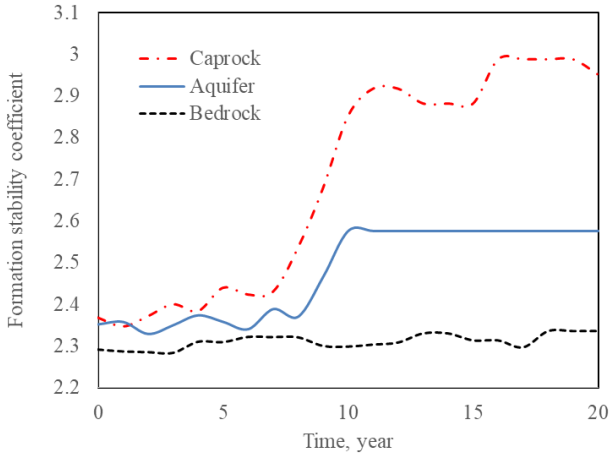

Figure 4-27 Formation stability coefficient at the evaluation sites for normal faulting environment

Caprock

During the injection and monitoring period, the horizontal and vertical effective stresses keep reducing. The vertical effective stress reduces at a slower rate during the 10-year injection; however, it reduces faster towards the end of injection period. For the horizontal effective stress, the injection period has a larger reduction rate than the monitoring rate. The caprock became more and more unstable during the injection as the formation stability coefficient keep increasing, and it started to stabilize during the monitoring period according to the slightly dropping formation stability coefficient. As shown in Fig. 4-28, the maximum formation stability coefficient did not reach the limit of the stability coefficient, 3.12. Therefore, caprock is kept as an intact structure in the given normal faulting environment. (Fig. 4-28)

As shown in Fig. 4-29a and b, this evaluation site reminds stable but keeps approaching the polygon periphery during the injection period. After the injection, it became closer to faulting because the evaluation site is close to the aquifer, and the high pressure in the

aquifer keeps spreading to the caprock, which would lead to instability (see Fig. 4-29c). Also, we can find that the stress state in Fig. 4-29c is closer to the periphery of the polygon compared to that in Fig. 4-29b. At ten years, the formation stability coefficient reaches 2.8513. During the monitoring period, the stability coefficient has a maximum value of 2.9876 in Fig. 4-27.

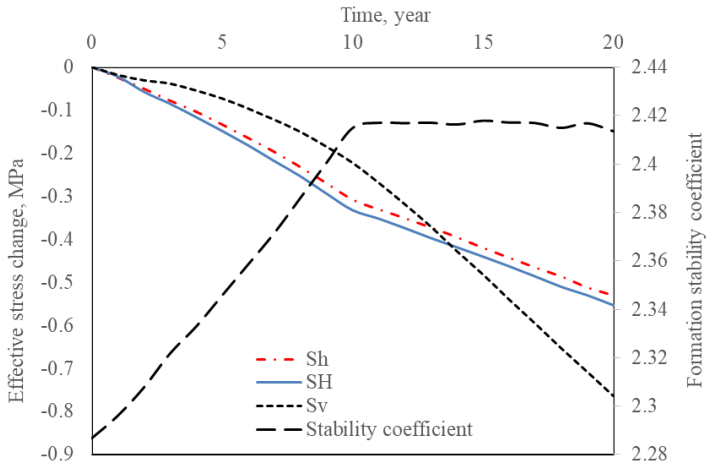

Figure 4-28 Effective stress and formation stability coefficient of caprock for normal faulting environment

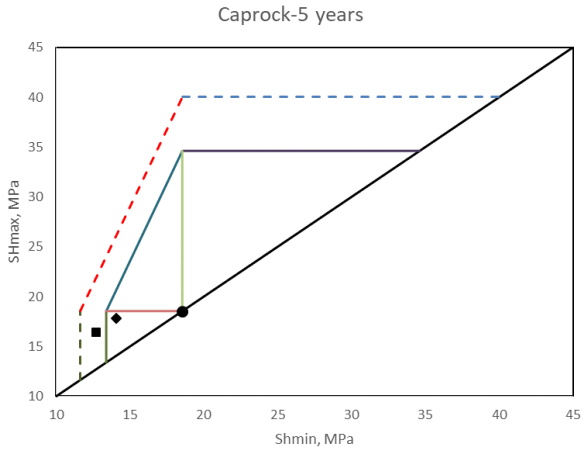

Figure 4-29a Stress polygon of caprock after 5-year injection

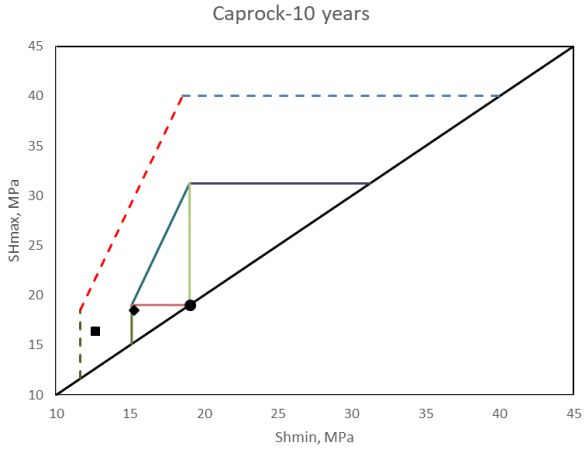

Figure 4-29b Stress polygon of caprock after 10-year injection

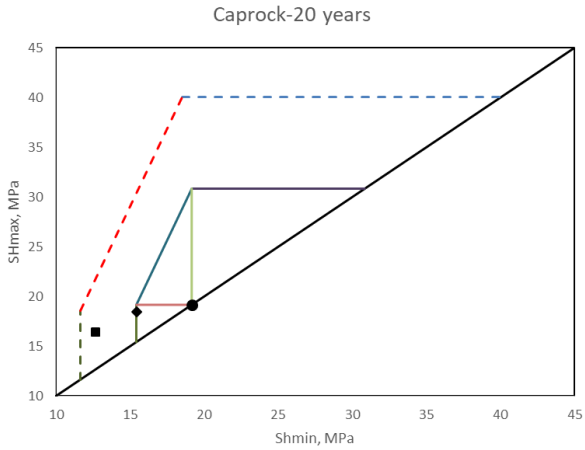

Figure 4-29c Stress polygon of caprock after the injection and monitoring period

Aquifer

During the injection period, the horizontal and vertical effective stresses keep reducing. By comparison, the vertical effective stress has a larger reduction than the horizontal effective stress. After the 10-year injection, the effective stress slightly bounces back and then becomes nearly constant, which indicates formation stability increasing at the beginning of the monitoring period, and the formation stability is kept in the following

years. This can also be concluded by the formation stability coefficient. Fig. 4-30 illustrates that the formation stability coefficient of the aquifer continues to rise during the injection period and drops slightly at the beginning of the monitoring period before being constant. At the end of the simulation, faulting does not happen, and the aquifer is still intact during monitoring period. (Fig 4-30)

Fig. 4-31 shows the stress polygons of the evaluation site of the aquifer. As shown in Fig. 4-31a and b, this evaluation site remains stable but keeps approaching the polygon edge during the injection period. After the injection, it became more stable because the high pressure in the aquifer keeps spreads to the surrounding formation, which would lead to stability in the aquifer (see Fig. 4-31c). At the end of the injection, the formation stability coefficient reaches 2.5760, and this value remains during the monitoring period.

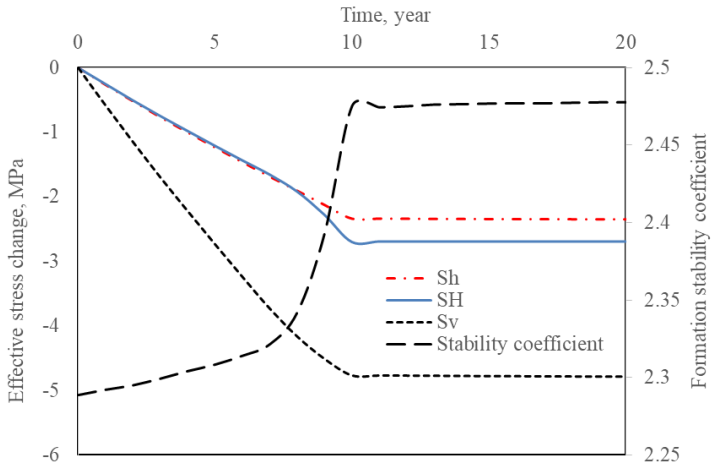

Figure 4-30 Effective stress and formation stability coefficient of the aquifer for normal faulting environment

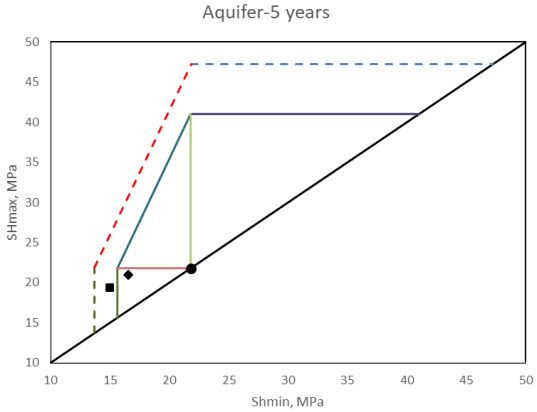

Figure 4-31a Stress polygon of aquifer after 5-year injection

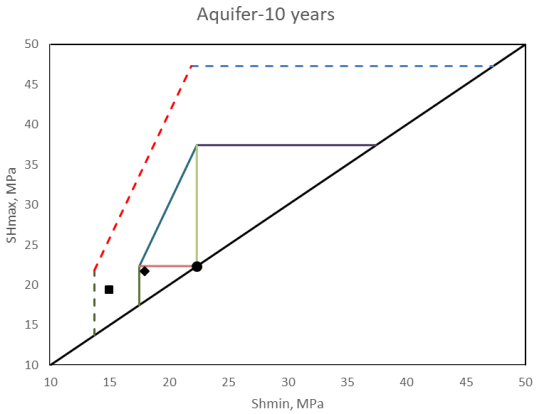

Figure 4-31b Stress polygon of aquifer after 10-year injection

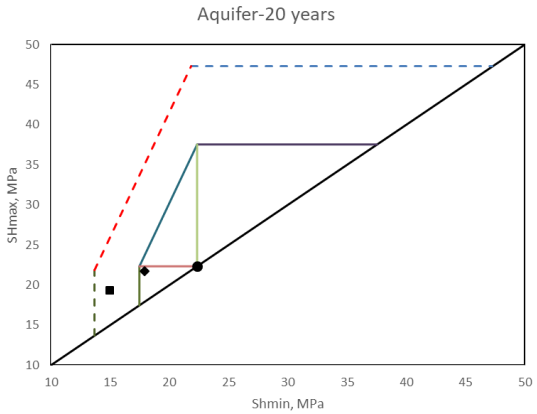

Figure 4-31c Stress polygon of aquifer after the injection and monitoring period

Bedrock

Fig. 4-32 shows that the horizontal effective stress reduces during the injection and monitoring period, and the vertical stress increases before reducing at the seventh year of the injection period. The formation stability coefficient continuously increases during the whole simulation, which indicates increasing formation instability. However, the bedrock remains stable at the end of the simulation.

As shown in Fig. 4-27, the formation stability continues to increase after the injection period, and the bedrock evaluation site remains stable during the injection and monitoring period. As shown in Fig. 4-33, the stress state does not change much, and it is inclined to switch to the strike-slip faulting environment.

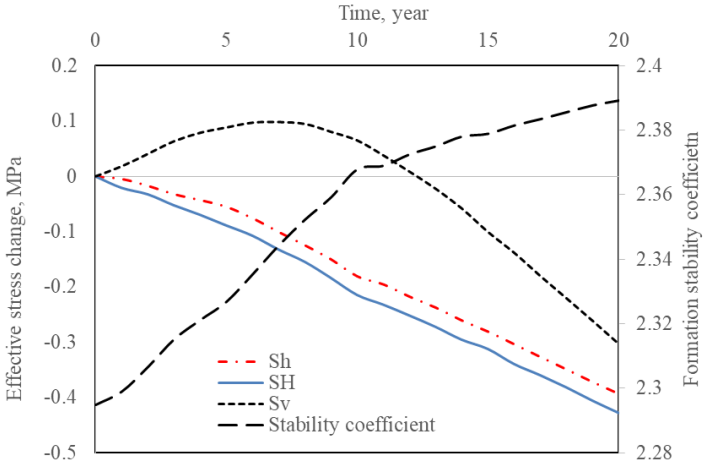

Figure 4-32 Effective stress and formation stability coefficient of bedrock for normal faulting environment

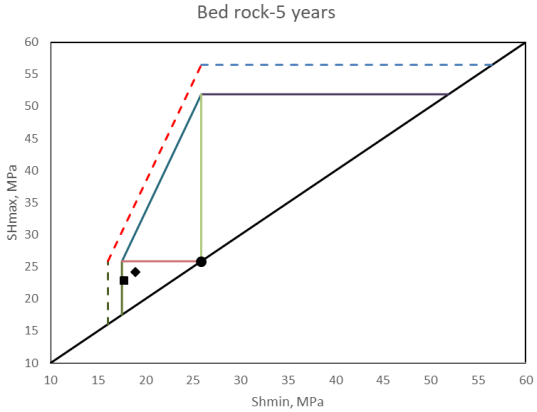

Figure 4-33a Stress polygon of bedrock after 5-year injection

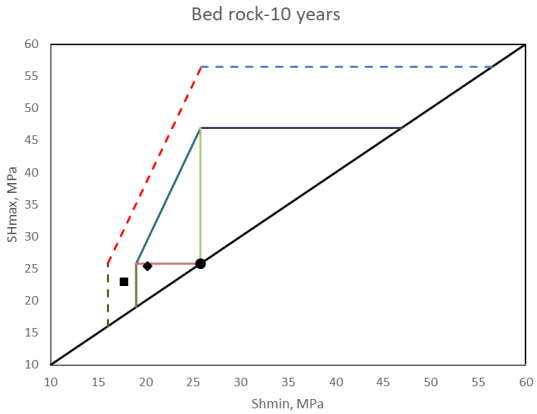

Figure 4-33b Stress polygon of bedrock after 10-year injection

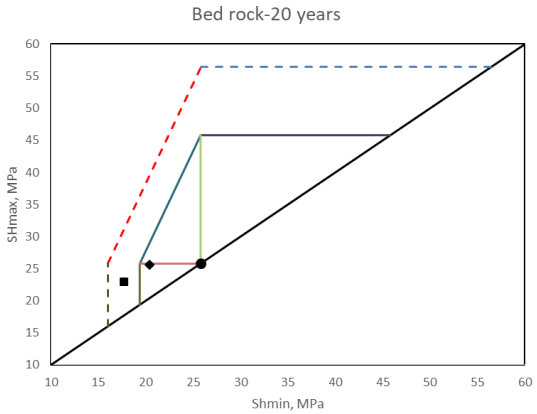

Figure 4-33c Stress polygon of bedrock after the injection and monitoring

Strike-Slip Faulting

For the strike-slip faulting environment, $S_{Hmax} \geq S_v \geq S_{hmin}$ is applied on in situ stress and stress limits are shown in the following figure (Fig. 4-34). In the strike-slip faulting environment in which pore pressure is hydrostatic, Eq. (4-1b) defines the highest value of the maximum principal stress and the lowest value of the minimum principal stress with depth. The maximum value of S_{Hmax} depends on the magnitude of the minimum horizontal stress, S_{hmin}. If the value of the minimum principal stress is known, Eq. (4-1b) can be used to put an upper bound on S_{Hmax}. When pore pressure is hydrostatic, the upper bound value of the largest principal stress S_{Hmax}~$1.41S_v$ and the lower bound value of the least principal stress S_{hmin}~$0.669S_v$, as illustrated by the red dashed line in Fig. 4-34. The initial principal stress is S_{hmin}~$0.752S_v$ and S_{Hmax}~$1.15S_v$. After the injection and monitoring period for 20 years, the stress state changes in the caprock, aquifer, and bedrock section. In the following parts, three sections will be analyzed accordingly.

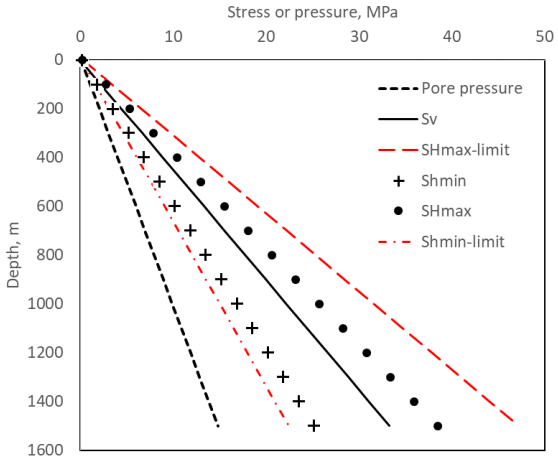

Figure 4-34 In situ stress and pore pressure for strike-slip faulting environment

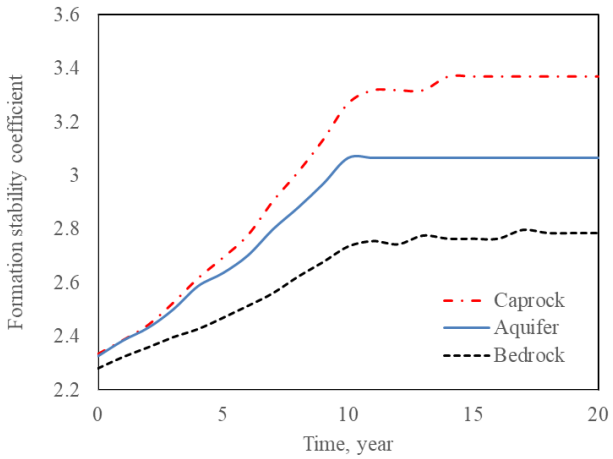

Figure 4-35 Formation stability coefficient at the evaluation sites for strike-slip faulting environment

Caprock

In Fig. 4-36, the effective stresses reduce through the 20-year simulation, and the reduction rate of the horizontal effective stresses becomes smaller when the monitoring period starts, while the vertical effective stress decreases at a higher rate when the monitoring period starts. By comparison, the vertical effective stress has a larger reduction. The formation stability coefficient continuously rises during the injection and monitoring period, and its increasing rate almost keeps constant. For the whole caprock, it is stable and intact since the average formation stability coefficient is less than 3.12.

At the fifth year of the injection, as shown in Fig 3-37a, the evaluation site at the caprock is stable, and no faults would be activated at the evaluation site. Fig. 3-37b shows that the strike-slip fault is activated before the end of the injection at the evaluation point of the caprock though the caprock structure as a whole is intact. The formation stability reaches 3.12 during the eighth year. And it has a value of 3.2685 at ten years, and the value

continues to increase to 3.3689 during the monitoring period. Also, we can see that the stress state gets further away from the stress polygon profile.

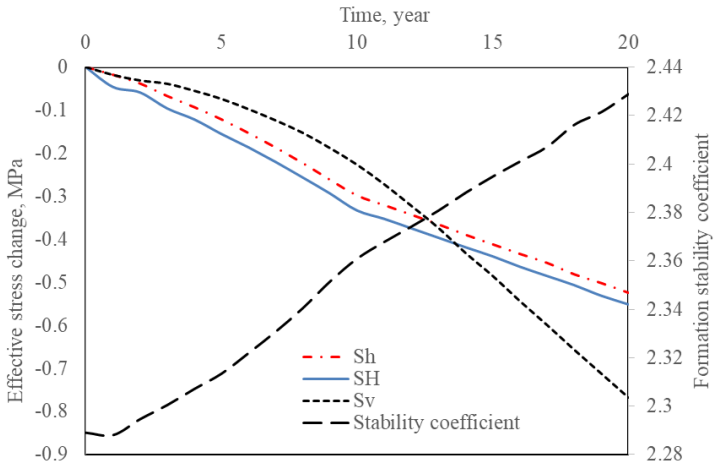

Figure 4-36 Effective stress and formation stability coefficient of caprock for strike-slip faulting environment

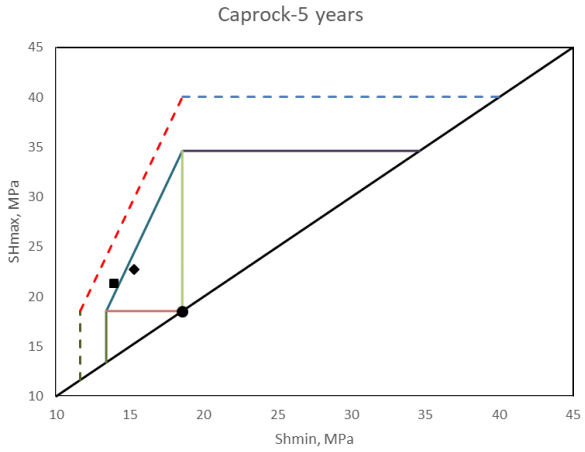

Figure 4-37a Stress polygon of caprock after 5-year injection

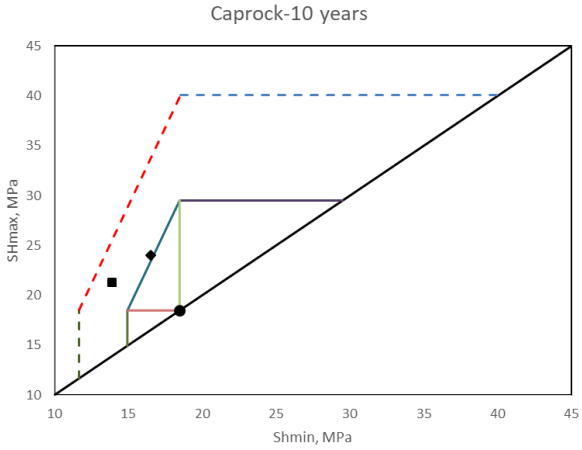

Figure 4-37b Stress polygon of caprock after 10-year injection

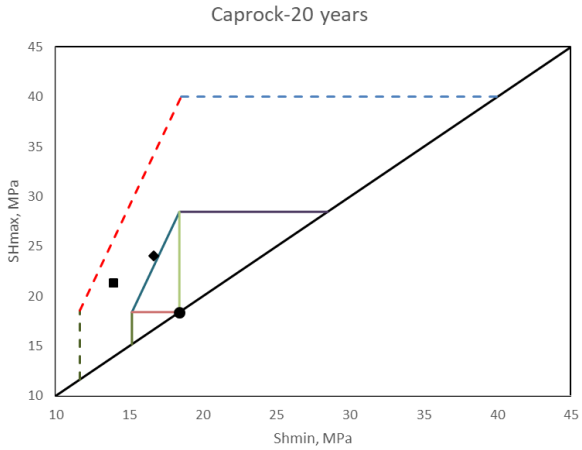

Figure 4-37c Stress polygon of caprock after the injection and monitoring period

Aquifer

During the injection period, the horizontal and vertical effective stresses keep reducing. By comparison, the vertical effective stress has a larger reduction than the horizontal effective stress. After the 10-year injection, the effective stress slightly bounces back and then becomes nearly constant, which indicates formation stability increasing at the beginning of the monitoring period, and the formation stability is kept in the following

years. This can also be concluded by the formation stability coefficient. Fig. 4-38 illustrates that the formation stability coefficient of the aquifer continues to rise during the injection period and drops slightly at the beginning of the monitoring period before being constant. The strike-slip fault is unlikely to be activated through the aquifer. (Fig 4-38)

At the fifth year of the injection, as shown in Fig. 3-39a, the stress state is still within the stress polygon, and no faults would be activated at the evaluation site. The stress state in Fig. 3-39b gets closer to the polygon profile, and the strike-slip fault has not been activated in the aquifer formation at the end of the injection period. At ten years, the formation stability coefficient reaches 3.0665, and this value keeps constant during the monitoring period.

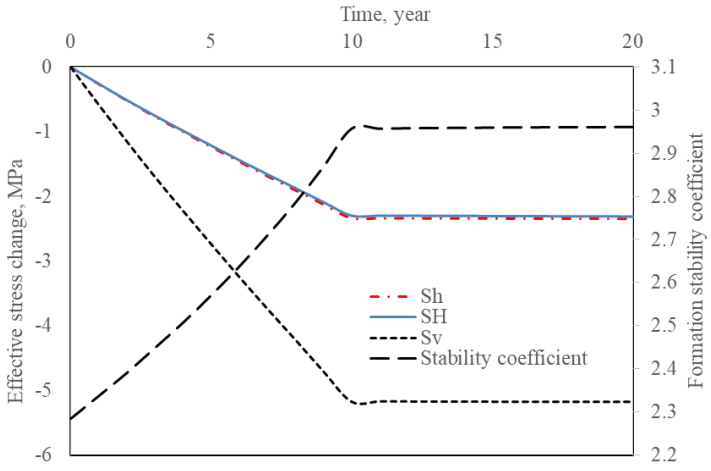

Figure 4-38 Effective stress and formation stability coefficient of the aquifer for strike-slip faulting environment

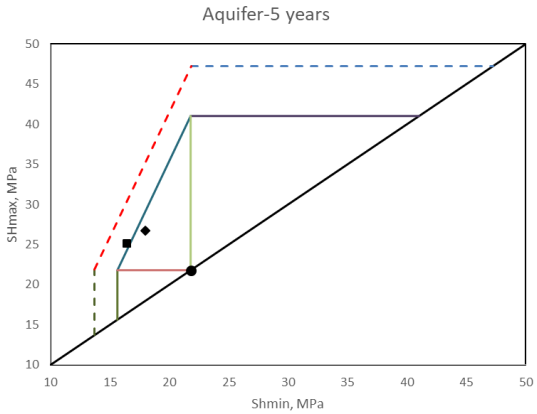

Figure 4-39a Stress polygon of aquifer after 5-year injection

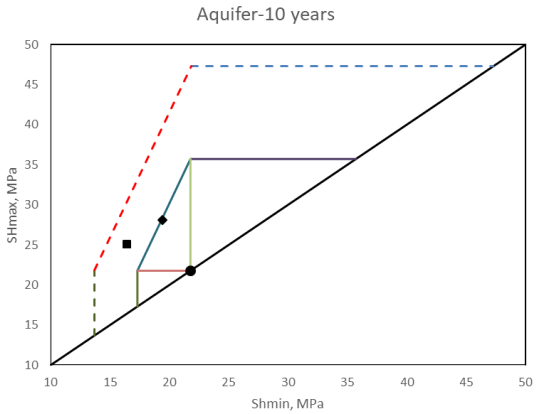

Figure 4-39b Stress polygon of aquifer after 10-year injection

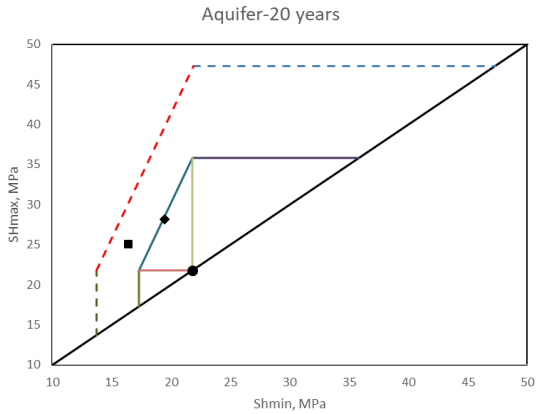

Figure 4-39c Stress polygon of aquifer after the injection and monitoring period

Bedrock

Fig. 4-40 shows that the horizontal effective stress reduces during the injection and monitoring period, and the vertical stress increases before reducing at the seventh year of the injection period. The formation stability coefficient continuously increases during the whole simulation, indicating increasing formation instability. However, the bedrock remains intact at the end of the simulation as the formation stability coefficient is less than 3.12.

As shown in Fig. 4-41, the stress state stays within the stress polygon, and the bedrock evaluation site remains stable during the injection and monitoring period. Strike-slip faulting is unlikely to be activated at this evaluation site through the simulation. The stress state moves toward the stress polygon profile during the injection period, and Fig. 4-35 also shows an increasing stability coefficient during the monitoring period. However, the stability coefficient does not reach 3.12 at 20 years.

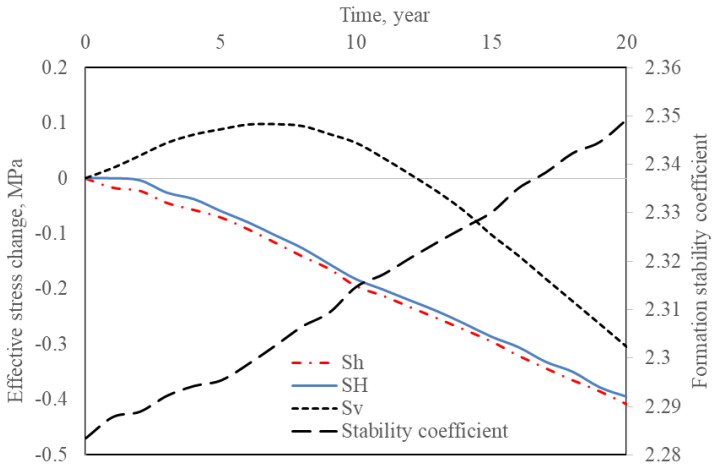

Figure 4-40 Effective stress and formation stability coefficient of bedrock for strike-slip faulting environment

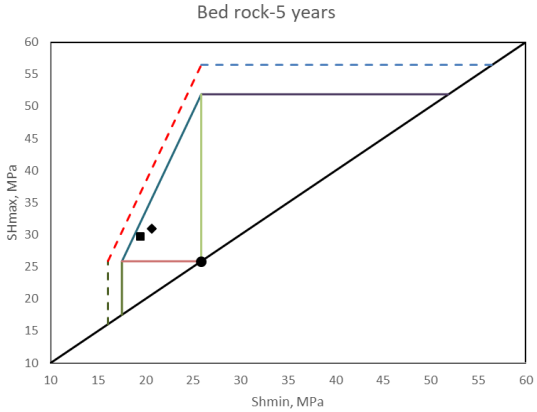

Figure 4-41a Stress polygon of bedrock after 5-year injection

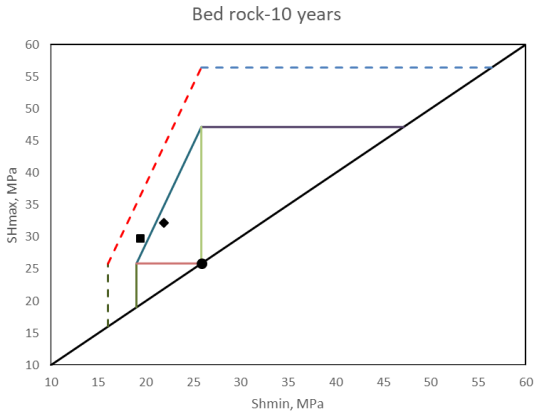

Figure 4-41b Stress polygon of bedrock after 10-year injection

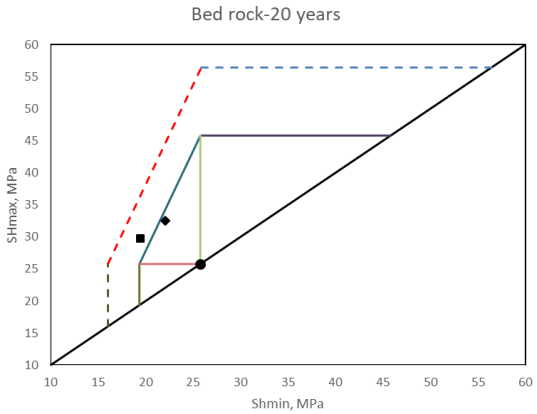

Figure 4-41c Stress polygon of bedrock after the injection and monitoring

Reverser Faulting

For the reverse faulting environment, $S_{Hmax} \geq S_{hmin} \geq S_v$ is applied on in situ stress, and stress limits are shown in the following figure (Fig. 4-42). In the reverse faulting environment in which pore pressure is hydrostatic, Eq. (4-1c) defines the highest value of the maximum principal stress with depth. When pore pressure is hydrostatic, the upper bound value of the largest principal stress S_{Hmax}~$2.18S_v$, as illustrated by the red dashed line in Fig. 4-36. The magnitude of the maximum principal stress cannot be high than this value because reverse faults would slip. The initial principal stress is S_{hmin}~$1.460S_v$ and S_{Hmax}~$1.991S_v$. After the injection and monitoring period for 20 years, the stress state changes in the caprock, aquifer, and bedrock section. In the following parts, three sections will be analyzed accordingly.

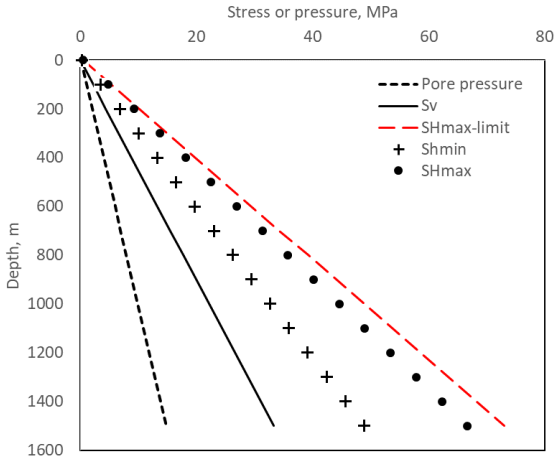

Figure 4-42 In situ stress and pore pressure for reverse faulting environment

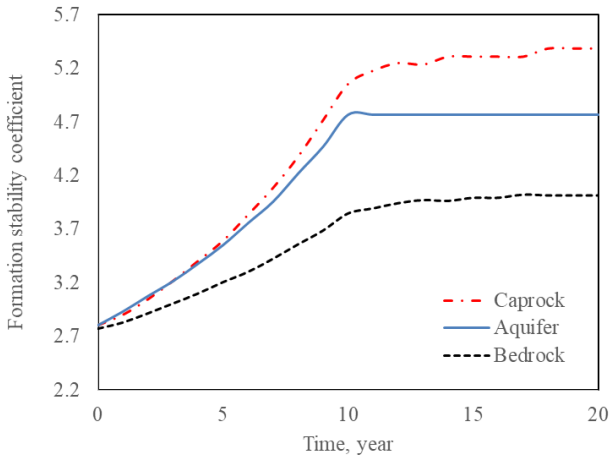

Figure 4-43 Formation stability coefficient at the evaluation sites for reverse faulting environment

Caprock

In Fig. 4-44, the effective stresses reduce through the 20-year simulation, and the reduction rate of the horizontal effective stresses becomes smaller when the monitoring period starts, while the vertical effective stress decreases at a higher rate when the monitoring period starts. By comparison, the vertical effective stress has a more significant reduction. The formation stability coefficient continuously rises during the injection and monitoring period, and its increasing rate becomes higher after the injection. For the whole caprock, it is stable and intact since the average formation stability coefficient is less than 3.12.

At the fifth year of the injection, as shown in Fig 4-45a, the reverse fault has been activated at the evaluation site of the caprock before this checkpoint, and the formation stability coefficient is 3.5960. Fig. 4-43 indicates that the seismic event is induced during the second year. The stress state approaches the stress polygon edige in Fig. 4-45b and c. The formation stability coefficient reaches 5.0576 at ten years and increases to 5.3895 at 20 years.

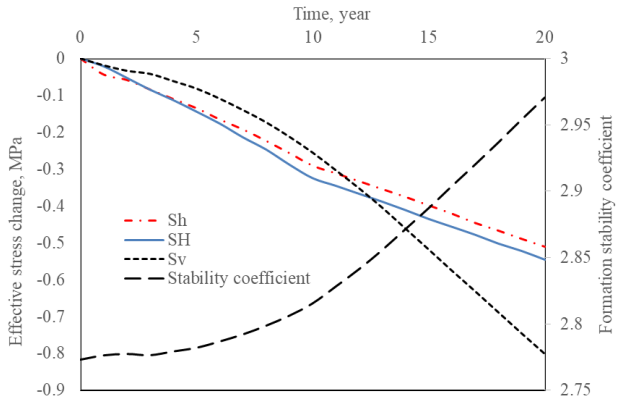

Figure 4-44 Effective stress and formation stability coefficient of caprock for reverse faulting environment

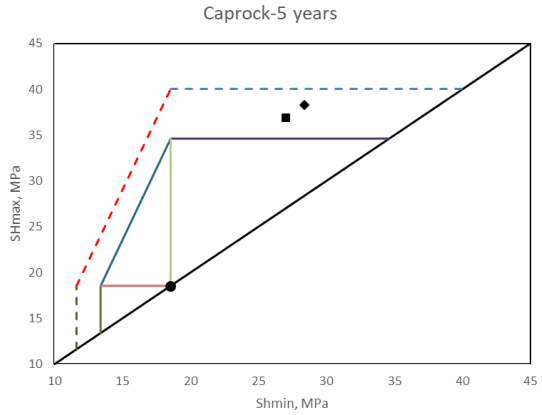

Figure 4-45a Stress polygon of caprock after 5-year injection

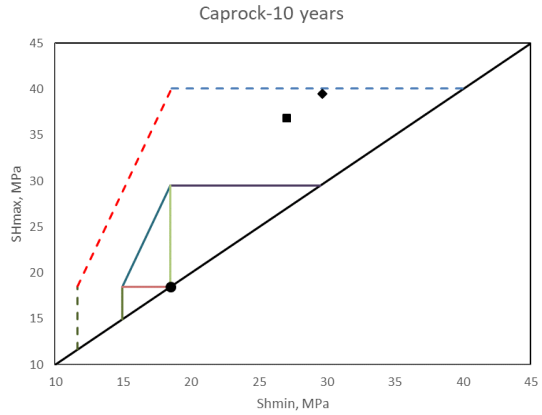

Figure 4-45b Stress polygon of caprock after 10-year injection

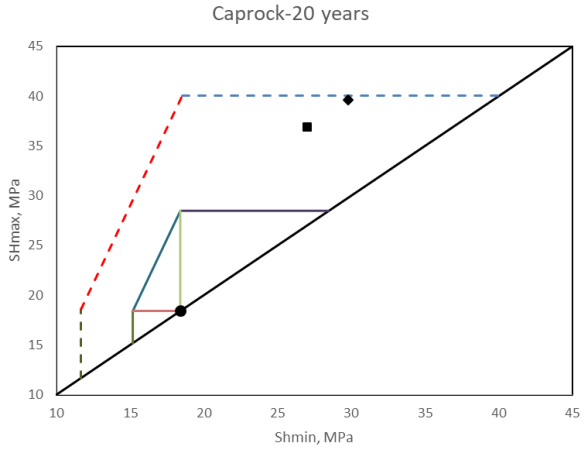

Figure 4-45c Stress polygon of caprock after the injection and monitoring period

Aquifer

During the injection period, the horizontal and vertical effective stresses keep reducing. By comparison, the vertical effective stress has a larger reduction than the horizontal effective stress. After the 10-year injection, the effective stress slightly bounces back and then becomes nearly constant, which indicates formation stability increasing at the beginning of the monitoring period, and the stability is kept in the following years. This can also be concluded by the formation stability coefficient. Fig. 4-46 illustrates that the formation stability coefficient of the aquifer continues to rise during the injection period and drops slightly at the beginning of the monitoring period before being constant. Before the third year of the injection period, the formation stability coefficient becomes larger than its limit, which indicates that reverse fault is activated through the aquifer. (Fig 4-46) At the fifth year of the injection, as shown in Fig 4-47a, the reverse fault has been activated at the evaluation site of the aquifer before this checkpoint, and the formation stability coefficient is 3.5535 in Fig. 43. The seismic event is induced during the second year of

the injection period. Fig. 4-47b and c suggest that the reverse fault continues to develop in the following years at the evaluation site. The formation stability coefficient reaches 4.7695 at the end of the injection period, and this value keeps constant during the monitoring period.

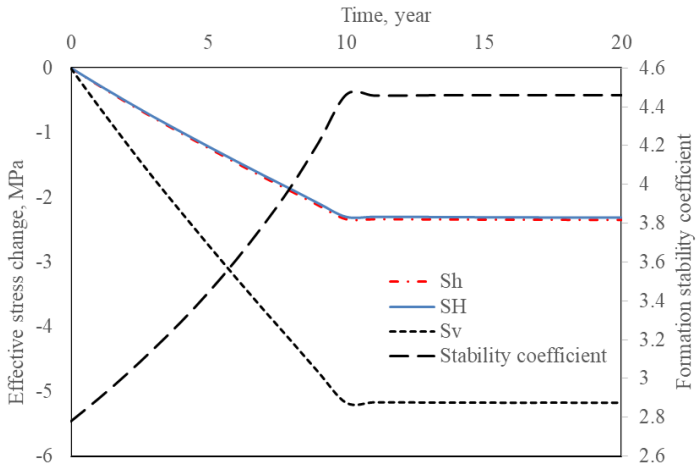

Figure 4-46 Effective stress and formation stability coefficient of the aquifer for reverse faulting environment

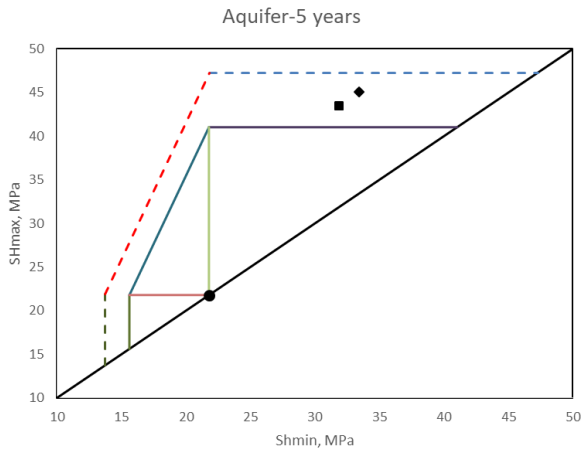

Figure 4-47a Stress polygon of aquifer after 5-year injection

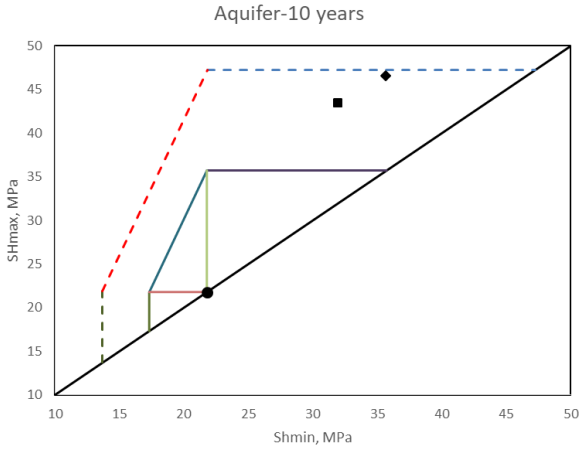

Figure 4-47b Stress polygon of aquifer after 10-year injection

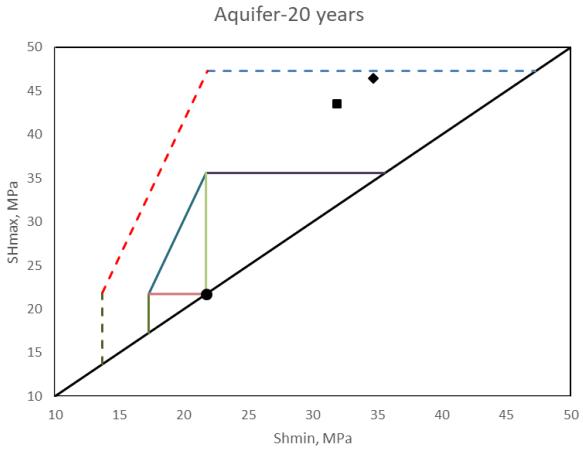

Figure 4-47c Stress polygon of aquifer after the injection and monitoring period

Bedrock

Fig. 4-48 shows that the horizontal effective stress reduces during the injection and monitoring period, and the vertical stress increases before reducing at the sixth year of the injection period. The formation stability coefficient decreases before starting to grow at the eighth year of the injection period, which indicates the bedrock is getting stable first

and then tends to get unstable. However, the bedrock remains intact at the end of the simulation as the formation stability coefficient is less than 3.12.

At the fifth year of the injection, as shown in Fig 4-49a, the reverse fault has been activated at the evaluation site of the aquifer before this checkpoint. The formation stability coefficient reaches 3.0993 at the fourth injection year, and the seismic event happens. The stability coefficient reaches 3.8453 at the end of the injection period. Fig. 4-49b and c suggest that the reverse fault continues to develop in the following years at the evaluation site. The stability coefficient continues to increase during the monitoring period and reaches 4.0133 at 20 years.

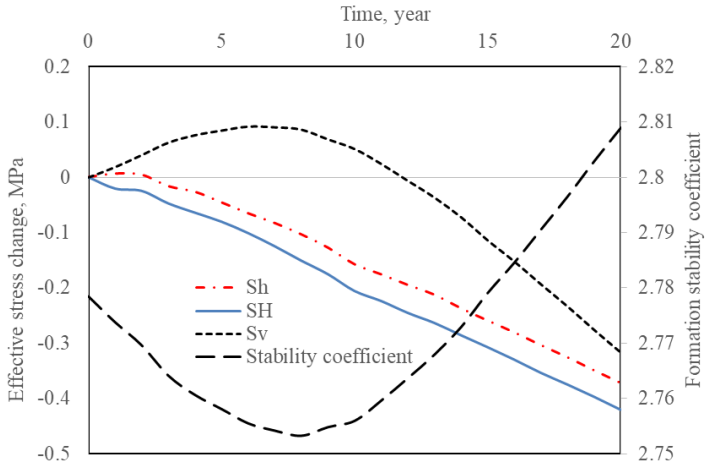

Figure 4-48 Effective stress and formation stability coefficient of bedrock for reverse faulting environment

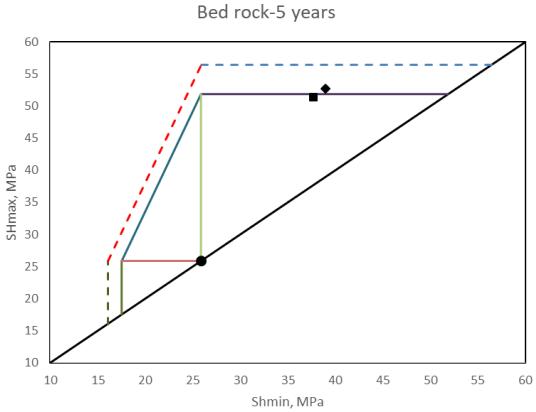

Figure 4-49a Stress polygon of bedrock after 5-year injection

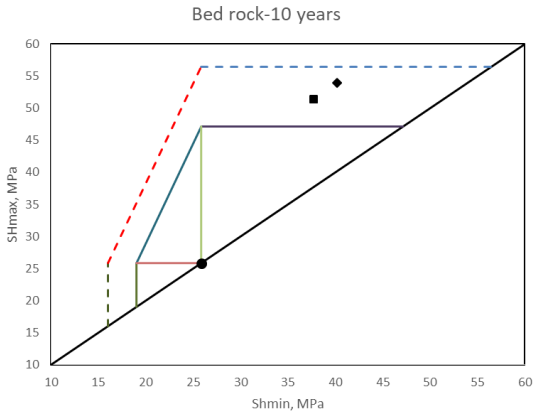

Figure 4-49b Stress polygon of bedrock after 10-year injection

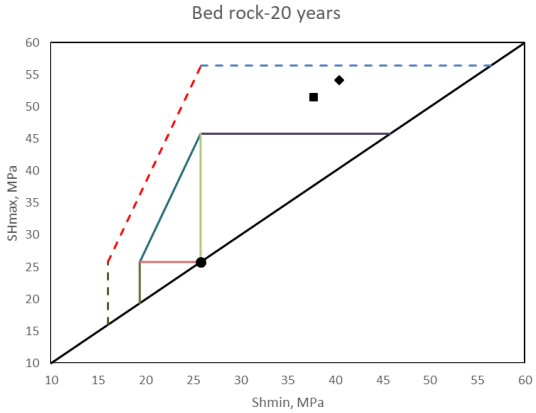

Figure 4-49c Stress polygon of bedrock after the injection and monitoring

Discussion

According to the result shown in the previous sections, caprock, aquifer, and bedrock have different mechanical behavior under normal faulting, reverse faulting, and strike-slip faulting environment. For the different formation arrangements, homogeneous formation, and soft aquifer, we can find differences in the behavior of formation. In the following parts, we will discuss the mechanical behavior of different formation sections under different faulting environments.

Effective Stress

The effective stresses in caprock continuously decrease during the injection and monitoring period due to the pore pressure increase. The horizontal effective stresses have a larger reduction rate during the injection period than that during the monitoring period. While the vertical effective stress acts differently, it has a higher reduction rate during the monitoring period. Among effective stresses, the vertical effective stress has the largest reduction, and the minimum horizontal effective stress has the smallest reduction.

In the aquifer, the effective stresses act in similar behavior, reducing during the injection period, slightly increasing as the monitoring period starts, and being constant. The vertical effective stress reduces much more than horizontal effective stresses.

The horizontal effective stresses have a different changing pattern from the vertical effective stress. The vertical effective stress increases at the beginning of the injection for several years and then decreases in the following injection years and monitoring period.

While the horizontal effective stresses continuously reduce through the whole simulation. By comparison, the horizontal effective stresses have a larger reduction.

Formation Stability Coefficient

Since the model assumes isotropic linear poro-elasticity, the effective stress changes are the same between the three faulting environments. However, the change in the formation stability coefficients is signinificantly different between the three regimes. In Fig 4-50, 4-51, and 4-52, the formation stability coefficient of homogeneous formation is on the left-hand side, and the coefficient of soft aquifer formation is on the right-hand side. From the following figures, we can find that the stability coefficient of the aquifer is larger than that of other formation sections and, therefore, fault activation most likely to happen in the aquifer section. This is because the aquifer section undergoes significant pressure increase. With soft aquifer formation, the aquifer section is more stable by comparison with the homogeneous formation.

As for the evaluation sites, the formation stability coefficient at different parts of the formation with soft aquifer is not larger than that of the homogeneous formation, indicating that the formation with a soft aquifer would be more stable than the homogeneous formation.

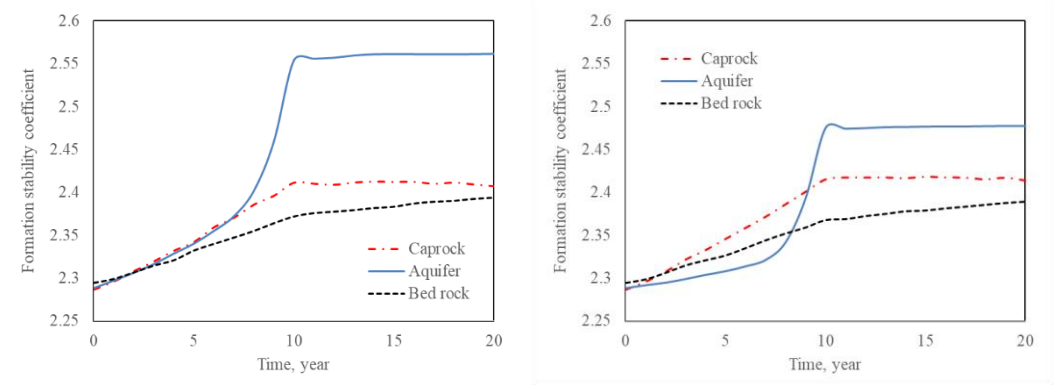

Figure 4-50 Formation stability coefficient of evalustion areas under normal faulting environment

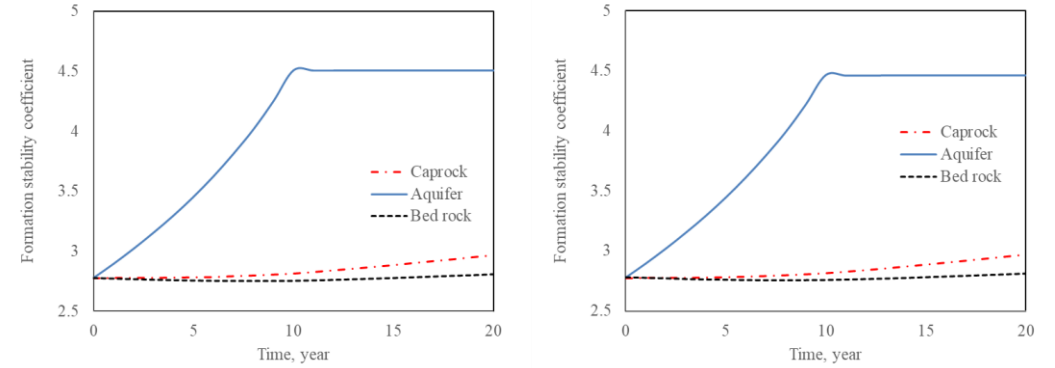

Figure 4-51 Formation stability coefficient of evalustion areas under reverse faulting environment

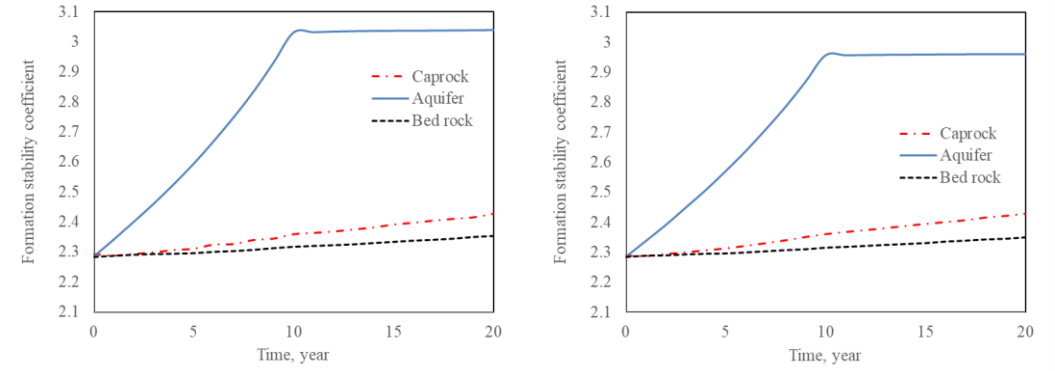

Figure 4-52 Formation stability coefficient of evalustion areas under strike-slip faulting environment

CHAPTER V

CONCLUSIONS

We proposed a new coupling workflow for the thermo-hydro-mechanical problem during CO2 injection in the water formation. We coupled fluid flow with geomechanical effects by coupling ECLIPSE and an in-house geomechanics simulator GEO3D. GEO3D was validated using the analytical solution for the ground surface deformation induced by pressure and temperature. The errors in ground surface subsidence and reservoir compactions are around 0.023% and 0.17%, respectively. We also validated the coupling model with the 1D Terzhagi's compaction problem using the fixed total stress method. Both the pressure distribution and formation compaction were compared with analytical solution and the error was small. The validated coupling model was applied to simulate the CO2 injection in a water formation. The pressure, temperature and stress changes are calculated during injection and obseravation period after injection. During a 20-year simulation, the average pressure of caprock and bedrock from the coupled simulation has a several-bar difference from the traditional reservoir simulation. The wellbore-vicinity thermal effect also stressed the importance of the coupling simulation. By applying the proposed coupling model, we provided a tool to evaluate the formation stability during CO2 injection. The formation stability coefficient and stress polygon were utilized to evaluate the stability of the water formation in three sections (caprock, aquifer, and bedrock) under three types of faulting environment (normal, strike-slip, and reverse faulting). Two types of formations were assumed: homogeneous formation and formation

with a soft aquifer. Results demonstrated that the faulting regime and Young's module could affect the performance of the storage site. The aquifer is much more unstable and is more likely to induce seismic events, comparing to the upper part of the caprock and the lower part of the bedrock. The lower part of the caprock and the upper part of the bedrock is also unstable since they are close to the aquifer, though the caprock and bedrock structure is intact and effective to seal the aquifer. Based on the stability analysis of evaluation sites and areas, the formation with soft aquifer is more stable than the homogeneous formation assuming the surrounding formation has the same Young's modules in two types of formation.

- After the injection and monitoring period, a larger increasing happens in permeability of the formation with a soft aquifer, indicating stronger geomechanical effects induced in pore volume and rock matrix.
- Due to the geomechanical effects, the average pressure calculated by coupled simulations is smaller than that of traditional simulations. This difference could be explained by the change in pore volume. In the formation with a soft aquifer, there is stronger influence in average pressure induced by geomechanical effects. The effects are also stronger in caprock and bedrock.
- The temperature calibration is much more significant in the aquifer section than that in the caprock and bedrock. At the end of the simulation, the temperature calibration in the aquifer and bedrock of the formation with a soft aquifer is higher than that of the homogeneous formation, in contrast to the temperature calibration in the caprock. The temperaute is averagely distributed throughout the model, and

apparent gradient can be found within 200m from the injection well. This is because homogeneous thermal properties are applied through the whole model.

- The ground surface deformation is more significant when the formation has a soft aquifer.
- According to the formation stability coefficient collected form the evaluation sites and areas, the formation with a soft aquifer is more stable, and the evaluation sites close to the well is more likely to have seismic events in contrast to the whole structure of evaluation areas.
- After injection, formation pressure increases, the profile of stress polygon shrinks, the stress state of evluation site changes. The stress polygon could be applied to evaluate the formation stability.
- Finally, based on our coupling model, the stress polygon and formation stability coefficient could be applied to evaluate the formation stability.
- In the future, we will optimize the grid system, refining grids near the borehole, to investigate the geomechanical effects around the well, and conduct more parametric studies using parameters obtained from various fields.

REFERENCES

Angeli M, Faleide JI, Gabrielsen RH. Evaluating seal quality for potential storage sites in the Norwegian North Sea. Energy Proc 2013;37:4853–62. http://dx.doi.org/10.1016/j.egypro.2013.06.395.

Bachu, S. 2003: Screening and ranking sedimentary basins for sequestration of CO2 in geological media in response to climate change. Environmental Geology, 44, pp 277−289.

Corey, A.T., 1954. The Interrelation between Gas and Oil Relative Permeabilities. Producers Monthly (November), pp. 38-42.

Gale J, Christensen NP, Cutler A, Torp TA. Demonstrating the potential for geological storage of CO2: the sleipner and GESTCO projects. Environ Geosci 2001;8:160–5. http://dx.doi.org/10.1046/j.1526-0984.2001.008003160.x.

Ghosh R, Sen MK, Vedanti N. Quantitative interpretation of CO2 plume from Sleipner (North Sea), using post-stack inversion and rock physics modeling. Int J Greenh Gas Control 2015;32:147–58. http://dx.doi.org/10.1016/j.ijggc.2014.11.002.

IEA. Global Status of CCS 2020; 2020. https://www.globalccsinstitute.com/wp-content/uploads/2021/03/Global-Status-of-CCS-Report-English.pdf

IPCC. Special report on carbon dioxide capture and storage, Cambridge; 2005. http://dx.doi.org/10.1021/cr2003272.

Kohl, A. L. and R.B. Nielsen, 1997: Gas Purification. Gulf Publishing Company, Houston, TX, USA.

MIT. Carbon capture and sequestration technologies. Massachusetts Inst Technol; 2015.<https://sequestration.mit.edu/tools/projects/index.html >[accessed March 23, 2021].

NIST, 2003: National Institute of Standards and Technology Standard Reference Database Number 69, March 2003, P.J. Linstrom andW.G. Mallard (eds.).

Span, R and W. Wagner, 1996: A new equation of state for carbon dioxide covering the fluid region from the triple-point temperature to 1100K at pressures up to 800 MPa. Journal of Phys. Chem. Data, 25(6), pp. 1509 −1596.

APPENDIX A

STRAIN NUCLEI METHOD

We now consider a small sphere with radius R and a uniform pressure in an infinite domain.

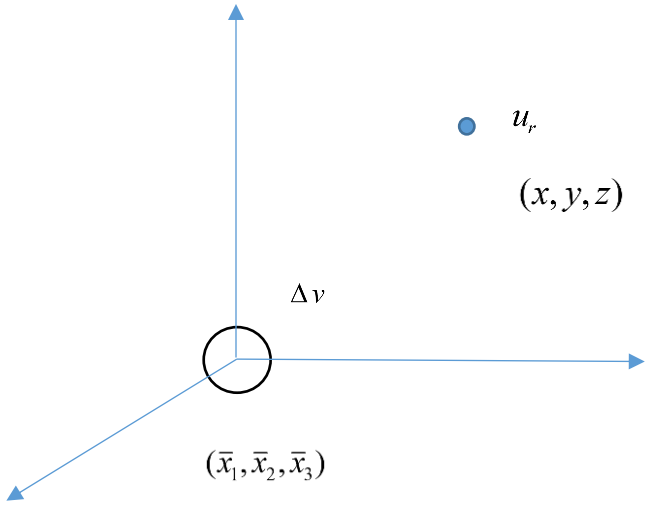

Fig. A-1 Strain neucli method

Transforming the equation of equilibrium without body force gives,

$$\frac{\partial \sigma_r}{\partial r} + \frac{1}{r}\left(2\sigma_r - \sigma_\varphi - \sigma_\theta\right) = 0 \tag{1}$$

for point symmetric problems.

The strain deformation relation is given by

$$\varepsilon_r = \frac{\partial u_r}{\partial r}, \varepsilon_\theta = \frac{u_r}{r}, \varepsilon_\varphi = \frac{u_r}{r} \tag{2}$$

The stress strain relation is given by

$$\sigma_{ij} = \frac{E}{1+\nu}\left(\varepsilon_{ij} + \frac{\nu}{1-2\nu}\varepsilon_{mm}\delta_{ij}\right) - (1-c_m)p\delta_{ij} \tag{3}$$

or

$$\sigma_r = \frac{E}{1+\nu}\left[\varepsilon_r + \frac{\nu}{1-2\nu}(\varepsilon_r + \varepsilon_\theta + \varepsilon_\varphi)\right] - (1-c_m)p \tag{4}$$

$$\sigma_\theta = \frac{E}{1+\nu}\left[\varepsilon_\theta + \frac{\nu}{1-2\nu}(\varepsilon_r + \varepsilon_\theta + \varepsilon_\varphi)\right] - (1-c_m)p \tag{5}$$

$$\sigma_\varphi = \frac{E}{1+\nu}\left[\varepsilon_\varphi + \frac{\nu}{1-2\nu}(\varepsilon_r + \varepsilon_\theta + \varepsilon_\varphi)\right] - (1-c_m)p \tag{6}$$

Where: $c_m = \frac{1-2\nu_m}{E_m} / \frac{1-2\nu}{E}$

Eliminating the stress and strains, the equations become

$$\frac{d^2u}{dr^2} + 2\frac{d}{dr}\left(\frac{u}{r}\right) - \frac{(1+\nu)(1-2\nu)}{E(1-\nu)}(1-c_o)\frac{dp}{dr} = 0 \tag{7}$$

When the pore pressure has no gradient, the differential equation becomes

$$\frac{d^2u}{dr^2} + 2\frac{d}{dr}\left(\frac{u}{r}\right) = 0 \tag{8}$$

The general solution is given by

$$u_r = C_1 r + \frac{C_2}{r^2} \tag{9}$$

Since the displacement becomes 0 at far field, the solution becomes

$$u_r = u_o \frac{R^2}{r^2} \tag{10}$$

where the displacement is u_o at $r = R$. Note that the radial displacement direction is inward on the sphere surface.

The volume change of the sphere is given by

$$\Delta v = -4\pi R^2 u_o \tag{11}$$

$$\text{Or } u_r = \frac{-\Delta v}{4\pi}\frac{1}{r^2} \tag{12}$$

This equation indicates that volume change Δv at the origin creates a displacement $u_r = \frac{-\Delta v}{4\pi}\frac{1}{r^2}$ at a distance r from the origin. Since R is assumed to be infinitely small, the shape does not affect the displacement if the reduction of volume is induced by a sphere, a cylinder or other shapes. For example, for uniaxial compaction problems, the volume change is given by:

$$\Delta v = C_m \Delta p V \tag{13}$$

Where: C_m is the compaction coefficient, $C_m = \frac{\beta(1-2\nu_r)(1+\nu_r)}{E_r(1-\nu_r)}$, $\beta = 1 - \frac{1-2\nu_m}{E_m} \Big/ \frac{1-2\nu}{E}$

Hence,

$$u_r = -\frac{C_m \Delta p}{4\pi}\frac{1}{r^2} V \tag{14}$$

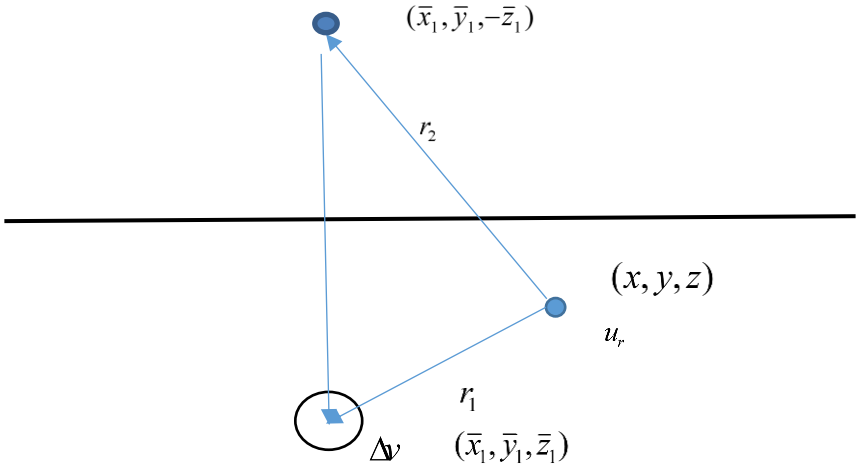

Fig. A-2 Strain nucleus for a half plane

Now consider strain nucleus for a half plane. At the surface, the axial stress must be zero and the following displacement satisfies the condition. Note that with the following displacement, the shear and vertical stresses on the earth surface become zero. Since $r_1 << r_2$ around the nucleus, the volume change around the nucleus is also equivalent to Eq. (12).

$$u_x^* = \frac{C_M \Delta p}{4\pi}(x - x_1)\left[\frac{1}{r_1^3} + \frac{3-4\nu}{r_2^3} - \frac{6z(z+z_1)}{r_2^5}\right] \tag{15}$$

$$u_y^* = \frac{C_M \Delta p}{4\pi}(y - y_1)\left[\frac{1}{r_1^3} + \frac{3-4\nu}{r_2^3} - \frac{6z(z+z_1)}{r_2^5}\right] \tag{16}$$

$$u_z^* = \frac{C_M \Delta p}{4\pi}\left[\frac{z-z_1}{r_1^3} + \frac{4\nu(z+z_1)-(z+3z_1)}{r_2^3} - \frac{6z(z+z_1)^2}{r_2^5}\right] \tag{17}$$

Where: $C_M = \frac{\beta(1-2\nu_r)(1+\nu_r)}{E_r(1-\nu_r)}$, $\beta = 1 - \frac{1-2\nu_m}{E_m} \Big/ \frac{1-2\nu}{E}$

$$r_1 = \sqrt{(x-x_1)^2 + (y-y_1)^2 + (z-z_1)^2}$$

$$r_2 = \sqrt{(x-x_1)^2 + (y-y_1)^2 + (z+z_1)^2}$$

Then, the displacement at (x, y, z) for a structure is calculated with:

$$u_i(x, y, z) = \int_V u_i^* dV(x_1, y_1, z_1) \tag{18}$$

For cylindrical coordinates, if $R > H$, the center of the nuclei z_1 is placed at the center plane of the reservoir and Eq. (18) is approximated as

$$u_i(r, z) = h\int_0^R \int_0^{2\pi} u_i^*(r, z, \xi, \theta)\xi d\xi d\theta \tag{19}$$

Note that Eq.19 is not a good approximation for $R > H$.

After complex transformations, the solution is given by:

For $z > 0$ (positive for surface to reservoir direction)

$$u_r = \frac{C_M R h \Delta p}{2} \int_0^\infty J_1(\alpha R) J_1(\alpha r) \left[e^{-\alpha(z-c)} - (4\nu - 3 + 2\alpha z) e^{-\alpha(z+c)} \right] d\alpha \tag{20}$$

$$u_z = \frac{C_M R h \Delta p}{2} \int_0^\infty J_1(\alpha R) J_0(\alpha r) \left[e^{-\alpha(z-c)} + (4\nu - 3 + 2\alpha z) e^{-\alpha(z+c)} \right] d\alpha \tag{21}$$

Along the center of the reservoir, Eq.20 gives by setting $r = 0$,

$$u_z(0,z) = 0.5 C_M h \Delta p \left[(3-4\nu) + \frac{D-z}{|D-z|} - \frac{(D-z)/R}{\sqrt{1+\left((D-z)/R\right)^2}} - \frac{(3-4\nu)(D+z)/R}{\sqrt{1+\left((D+z)/R\right)^2}} + \frac{2z/R}{\left(1+(D+z)^2/R^2\right)^{1.5}} \right] \tag{22}$$

Hence, the subsidence at the center of the subsidence bowl is given by

$$u_z(0,0) = 2 C_M h \Delta p (1-\nu) \left[1 - \frac{1}{\sqrt{1+(R/D)^2}} \right] \tag{23}$$

The stresses are given by

$$\sigma_r = 2G \frac{\partial u_r}{\partial r} + \lambda \left(\frac{\partial u_r}{\partial r} + \frac{u_r}{r} + \frac{\partial u_z}{\partial z} \right) \tag{24}$$

$$\sigma_\theta = 2G \frac{u_r}{r} + \lambda \left(\frac{\partial u_r}{\partial r} + \frac{u_r}{r} + \frac{\partial u_z}{\partial z} \right) \tag{25}$$

$$\sigma_z = 2G \frac{\partial u_z}{\partial z} + \lambda \left(\frac{\partial u_r}{\partial r} + \frac{u_r}{r} + \frac{\partial u_z}{\partial z} \right) \tag{26}$$

$$\tau_{rz} = G \left(\frac{\partial u_z}{\partial r} + \frac{\partial u_r}{\partial z} \right) \tag{27}$$

The solutions are given by Hankel integrals:

$$\sigma_r = GC_M Rh\Delta p\left[\left(I_{(1,0;1)}{}^{(z-c)} + 3I_{(1,0;1)}{}^{(z+c)} - 2zI_{(1,0;2)}{}^{(z+c)}\right) - \frac{1}{r}\left(I_{(1,1;0)}{}^{(z-c)} + (3-4\nu)I_{(1,0;1)}{}^{(z+c)} - 2zI_{(1,1;1)}{}^{(z+c)}\right)\right]$$

(28)

$$\sigma_\theta = GC_M Rh\Delta p\left[4\nu I_{(1,0;1)}{}^{(z+c)} + \frac{1}{r}\left(I_{(1,1;0)}{}^{(z-c)} + (3-4\nu)I_{(1,1;0)}{}^{(z+c)} - 2zI_{(1,1;1)}{}^{(z+c)}\right)\right] \quad (29)$$

$$\sigma_z = GC_M Rh\Delta p\left(-I_{(1,0,1)}{}^{(z-c)} + I_{(1,0,1)}{}^{(z+c)} + 2zI_{(1,0,2)}{}^{(z+c)}\right) \quad (30)$$

$$\tau_{rz} = GC_M Rh\Delta p\left(-I_{(1,1;1)}{}^{(z-c)} - I_{(1,1;1)}{}^{(z+c)} + zI_{(1,1;2)}{}^{(z+c)}\right) \quad (31)$$

Where: $I^\lambda(l,m,n) = \int_0^\infty e^{-\lambda\alpha}\alpha^n J_l(\alpha R)J_m(\alpha r)d\alpha$

At $r = 0$:

$$\sigma_r = \sigma_\theta = 0.5GC_M Rh\Delta p\left(I_{(1,0;1)}{}^{(z-c)} + (3+4\nu)I_{(1,0;1)}{}^{(z+c)} - 2zI_{(1,0;2)}{}^{(z+c)}\right) \quad (32)$$

$$\sigma_z = GC_M Rh\Delta p\left(-I_{(1,0;1)}{}^{(z-c)} + I_{(1,0;1)}{}^{(z+c)} + 2zI_{(1,0;2)}{}^{(z+c)}\right) \quad (33)$$

$$\tau_{rz} = 0 \quad (34)$$

For $r = 0$, only the following integration must be evaluated.

$$I^\lambda(\ell = 1, m = 0, n = 1 or 2) = \int_0^\infty e^{-\lambda\alpha}\alpha^n J_1(\alpha R)d\alpha \quad (35)$$

$$\sigma_r = \sigma_\theta = 0.5GC_M Rh\Delta p\left(\int_0^\infty e^{-(z-c)\alpha}\alpha J_1(\alpha R)d\alpha + (3+4\nu)\int_0^\infty e^{-(z+c)\alpha}\alpha J_1(\alpha R)d\alpha - 2z\int_0^\infty e^{-(z+c)\alpha}\alpha^2 J_1(\alpha R)d\alpha\right)$$

$$= \frac{0.5GC_M h}{R}\Delta p\left(\frac{1}{[1+\left(\frac{z-c}{R}\right)^2]^{\frac{3}{2}}} + \frac{(3+4\nu)}{[1+\left(\frac{z+c}{R}\right)^2]^{\frac{3}{2}}} - \frac{6z(z+c)}{R^2[1+\left(\frac{z+c}{R}\right)^2]^{\frac{5}{2}}}\right)$$

(36)

$$\sigma_z = GC_M h\Delta pR\left(-\int_0^\infty e^{-(z-c)\alpha}\alpha J_1(\alpha R)d\alpha + \int_0^\infty e^{-(z+c)\alpha}\alpha J_1(\alpha R)d\alpha + 2z\int_0^\infty e^{-(z+c)\alpha}\alpha^2 J_1(\alpha R)d\alpha \right)$$

$$= \frac{GC_M h}{R}\Delta p\left(-\frac{1}{[1+\left(\frac{z-c}{R}\right)^2]^{\frac{3}{2}}} + \frac{1}{[1+\left(\frac{z+c}{R}\right)^2]^{\frac{3}{2}}} + \frac{6z(z+c)}{R^2[1+\left(\frac{z+c}{R}\right)^2]^{\frac{5}{2}}} \right)$$

(37)

$$\tau_{rz} = 0 \tag{38}$$

The strains and stresses are given as follows as shown in Appendix.

$$\varepsilon_r = \varepsilon_\theta = (-C_M h\Delta p / D)(-0.25)\frac{D}{R}\left(\frac{(R/D)^3}{[(R/D)^2+\left(\frac{D-z}{D}\right)^2]^{\frac{3}{2}}} + \frac{(3-4\nu)(R/D)^3}{[(R/D)^2+\left(\frac{z+D}{D}\right)^2]^{\frac{3}{2}}} - \frac{6z(z+D)(R/D)^3}{D^2[(R/D)^2+\left(\frac{z+D}{D}\right)^2]^{\frac{5}{2}}} \right)$$

(39)

$$\varepsilon_z = (-C_M h\Delta p / D)(-0.5)\frac{D}{R}\left(-\frac{(R/D)^3}{[(R/D)^2+\left(\frac{D-z}{D}\right)^2]^{\frac{3}{2}}} + \frac{(1-4\nu)(R/D)^3}{[(R/D)^2+\left(\frac{z+D}{R}\right)^2]^{\frac{3}{2}}} + \frac{6z(z+D)(R/D)^3}{D^2[(R/D)^2+\left(\frac{z+D}{D}\right)^2]^{\frac{5}{2}}} \right)$$

(40)

$$\sigma_r = \sigma_\theta = -G(C_M h\Delta p / D)(-0.5)\frac{D}{R}\left(\frac{(R/D)^3}{[(R/D)^2+\left(\frac{D-z}{D}\right)^2]^{\frac{3}{2}}} + \frac{(3+4\nu)(R/D)^3}{[(R/D)^2+\left(\frac{z+D}{D}\right)^2]^{\frac{3}{2}}} - \frac{6z(z+D)(R/D)^3}{D^2[(R/D)^2+\left(\frac{z+D}{D}\right)^2]^{\frac{5}{2}}} \right)$$

(41)

$$\sigma_z = -G(C_M h\Delta p / D)(\frac{-D}{R})\left(-\frac{(R/D)^3}{[(R/D)^2+\left(\frac{D-z}{D}\right)^2]^{\frac{3}{2}}} + \frac{(R/D)^3}{[(R/D)^2+\left(\frac{z+D}{D}\right)^2]^{\frac{3}{2}}} + \frac{6z(z+D)(R/D)^3}{D^2[(R/D)^2+\left(\frac{z+D}{D}\right)^2]^{\frac{5}{2}}} \right)$$

(42)

APPENDIX B

In this part, we are going to obtain the equilibrium equations for flow and mechanical problem in 1D uniaxial compaction problem.

The stress strain relation is given by:

$$\sigma_{ij} = \frac{E}{1+\nu}\varepsilon_{ij} + \frac{E\nu}{(1-2\nu)(1+\nu)}\varepsilon_{kk}\delta_{ij} - \alpha p\delta_{ij} \tag{1}$$

For uniaxial compaction, $i = j = k = 3$ so we have:

$$\sigma_{33} = \frac{E}{1+\nu}\varepsilon_{33} + \frac{E\nu}{(1-2\nu)(1+\nu)}\varepsilon_{33} - \alpha p \tag{2}$$

And Eq. (67) can be written as:

$$\sigma_{33} = \frac{E(1-\nu)}{(1-2\nu)(1+\nu)}\varepsilon_{33} - \alpha p \tag{3}$$

$$\sigma_z = \bar{K}_{dr}\frac{\partial u}{\partial z} - \alpha p \tag{4}$$

Where: the drained uniaxial compaction coefficient $\bar{K}_{dr} = \frac{E(1-\nu)}{(1-2\nu)(1+\nu)}$, while the standard drained uniaxial compaction coefficient should be given by:

$$\bar{K}_{dr} = \frac{\alpha E(1-\nu)}{(1-2\nu)(1+\nu)}.$$

For the equilibrium equation of mechanics problem, we start from the following equation:

$$\sigma^{e}_{ij,j} - \alpha p_{,j}\delta_{ij} + F_i = 0 \tag{5}$$

Plugging $\sigma^{e}_{ij} = \frac{E}{1+\nu}\varepsilon_{ij} + \frac{E\nu}{(1-2\nu)(1+\nu)}\varepsilon_{kk}\delta_{ij}$ and $\varepsilon_{ij} = \frac{1}{2}(u_{i,j} + u_{j,i})$ and eliminating the strain and stress:

$$\frac{E}{2(1+\nu)}\frac{\partial^2 u_i}{\partial x_j \partial x_j}+\frac{E}{2(1+\nu)(1-2\nu)}\frac{\partial^2 u_i}{\partial x_i \partial x_j}-\alpha\frac{\partial p}{\partial x_j}\delta_{ij}+F_i=0 \tag{6}$$

The Terzhagi's uniaxial compaction problem assumes no displacement in the horizontal direction and no body force. Therefore, the equation is reduced to:

$$\overline{K}_{dr}\frac{\partial}{\partial z}\left(\frac{\partial u}{\partial z}\right)-\alpha\frac{\partial p}{\partial z}=0 \tag{7}$$

Now, let consider the continuity equation for flow problem:

$$\frac{\partial}{\partial x}(\rho\frac{K_x\delta}{\mu}\frac{\partial p}{\partial x})+\frac{\partial}{\partial y}(\rho\frac{K_y\delta}{\mu}\frac{\partial p}{\partial y})+\frac{\partial}{\partial z}(\rho\frac{K_z\delta}{\mu}\frac{\partial p}{\partial z})=\partial(\rho V_{pore})/\partial t \tag{8}$$

For small compressibility given by $\rho=\rho_o e^{c_f(p-p_o)}$, we have

Using $\frac{\partial\rho}{\partial x_i}=c\frac{\partial p}{\partial x_i}$, and $\frac{\partial\rho}{\partial t}=c\frac{\partial p}{\partial t}$, we have:

$$\rho\frac{K_x\delta}{\mu}\frac{\partial}{\partial x}(\frac{\partial p}{\partial x})+\rho\frac{K_y\delta}{\mu}\frac{\partial}{\partial y}(\frac{\partial p}{\partial y})+\rho\frac{K_z\delta}{\mu}\frac{\partial}{\partial z}(\frac{\partial p}{\partial z})+\frac{\partial}{\partial x}(\rho\frac{K_x\delta}{\mu})+\frac{\partial}{\partial y}(\rho\frac{K_y\delta}{\mu})+\frac{\partial}{\partial z}(\rho\frac{K_z\delta}{\mu})=(\rho V_{pore}c)\partial p/\partial t+(\rho)\partial V_{pore}/\partial t$$

(9)

The pore volume change is given by :

$$\delta V_{pore}=\alpha\delta\varepsilon_{kk}+(\alpha-\phi)c_m\delta p \tag{10}$$

Where: $c_m=\frac{3(1-2\nu_m)}{E_m}$

Note that the equation of the pore volume change δV_{pore} may be different depending on how it is approximated, although the difference of the value is negligibly small if each term is substituted by measured rock properties.

Since the following term is small comparing with the first three terms, we may assume

$$\frac{\partial}{\partial x}(\rho\frac{K_x\delta}{\mu})+\frac{\partial}{\partial y}(\rho\frac{K_y\delta}{\mu})+\frac{\partial}{\partial z}(\rho\frac{K_z\delta}{\mu})\approx 0 \tag{11}$$

Then,

$$\frac{k_x}{\mu}\frac{\partial^2 p}{\partial x^2}+\frac{k_y}{\mu}\frac{\partial^2 p}{\partial y^2}+\frac{k_z}{\mu}\frac{\partial^2 p}{\partial z^2}=(\phi c_f)\partial p/\partial t+\partial[\alpha\varepsilon_{kk}+(\alpha-\phi)c_m p]/\partial t \tag{12}$$